1225-0767(ISSN Print)
2287-6715(ISSN Online)
한국연구재단 우수등재학술지

Journal of Ocean Engineering and Technology

Vol. 37, No. 1 (Serial Number 170)

February 2023

한국해양공학회지

KSOE

www.joet.org

KSOE The Korean Society of Ocean Engineers

Journal of Ocean Engineering and Technology
한국해양공학회지
Vol. 37 No. 1
(Serial Number 170)
February 28, 2023
www.JOET.org

Published on February 28, 2023
Published by The Korean Society of Ocean Engineers (KSOE)
Room 1302, 13, Jungang-daero 180beon-gil, Dong-gu, Busan, 48821, Korea
TEL: +82-51-759-0656 FAX: +82-51-759-0657 E-mail: ksoehj@ksoe.or.kr URL: http://www.ksoe.or.kr
Printed by Hanrimwon Co., Ltd., Seoul, Korea E-mail: hanrim@hanrimwon.co.kr
ISSN(print) 1225-0767 **ISSN(online)** 2287-6715

This journal was supported by the Korean Federation of Science and Technology Societies (KOFST) grant funded by the Korean government.

Journal of Ocean Engineering and Technology
한국해양공학회지

CONTENTS

Volume 37, Number 1 February, 2023

<Original Research Articles>

GENERAL INFORMATION

"Journal of Ocean Engineering and Technology" is the official journal published by "The Korean Society of Ocean Engineers (KSOE)". The ISO abbreviation is "J. Ocean Eng. Technol." and acronym is "**JOET**". It was launched in 1987. It is published bimonthly in February, April, June, August, October, and December each year. Supplement numbers are published at times.

Journal of Ocean Engineering and Technology (JOET) is a medium for the publication of original research and development work in the field of ocean engineering. JOET covers the entire range of issues and technologies related to the following topics:

Ships and offshore platforms: Design of marine structures; Resistance and propulsion; Seekeeping and maneuvering; Experimental and computational fluid dynamics; Ocean wave mechanics; Fatigue strength; Plasticity; Optimization and reliability; Arctic technology and extreme mechanics; Noise, vibration, and acoustics; Concrete engineering; Thermodynamics and heat transfer; Hydraulics and pneumatics;
Coastal engineering: Coastal structures; Port and harbor structures; Soil mechanics; Drilling and exploration; Hydraulics of estuary; Seismic engineering; Coastal disaster prevention engineering;
Ocean renewable energy platforms: Offshore wind turbines; Wave energy platforms; Tidal current energy platforms; Floating photovoltaic energy platforms;
Marine robots: Robot sensor system; Autonomous navigation; Robot equipments; Spatial information and communications; Underwater network; Design of underwater vehicles;
Multidisciplinary areas: Design for safety; IT-based design; IT-based production engineering; Welding mechanics; Control engineering; GPS and GIS; Inspection and sensor; Port and logistics; Leisure boat and deep see water; Offshore process systems engineering; Marine metallic materials; Marine organic materials; Marine Composite materials; Materials properties; Corrosion and Anti-corrosion; Tribology;

It contains original research articles, case reports, brief communications and reviews on technial issues. Conference papers, research papers, diploma papers and academic articles can be submitted.

All of the manuscripts are peer-reviewed. **JOET** has a system where two or more peer reviewers must review each submitted paper and it is operated very strictly.

JOET is being indexed in some prominent database such as Korean Citatation Index (KCI), Google Scholar, Science Central, Korea Science and Directory of Open Access Journals (DOAJ).

For correspondences concerning business matters, author needs to contact KSOE Secretariat by email or phone (e-mail: ksoehj@ksoe.or.kr or Tel: +82 51 759 0656). Correspondences for publication matters can be asked via email to the Editor-in-Chief (email: heroeswise2@gmail.com).

KSOE

Journal of Ocean Engineering and Technology 37(1), 1-7 February, 2023
https://doi.org/10.26748/KSOE.2022.032

pISSN 1225-0767
eISSN 2287-6715

Original Research Article

Motion Response Characteristics of Small Fishing Vessels of Different Sizes among Regular Waves

DongHyup Youn[1], LeeChan Choi[2] and JungHwi Kim[3]

[1]*Senior Researcher, Design Engineering Support Center, Research Institute of Medium & Small Shipbuilding, Busan, Korea*
[2]*Researcher, Design Engineering Support Center, Research Institute of Medium & Small Shipbuilding, Busan, Korea*
[3]*Senior Engineer, Design Engineering Support Center, Research Institute of Medium & Small Shipbuilding, Busan, Korea*

KEYWORDS: Small fishing vessel, Basin test, Roll motion, Pitch motion, Wavesteepness, Regular wave

ABSTRACT: *The motion of small fishing vessels is significantly affected by small waves, leading to accidents, such as capsizing or sinking. This paper presents the results of two types of basin tests. The first test analyzed the characteristics of roll and pitch motions among regular waves with the same wave steepness using the drifting state of three (3G/T, 7G/T, 10G/T) small fishing vessels. The second test analyzed the motion characteristics of the 7G/T fishing vessel under different wave steepness. The first test showed that heave and roll motions are significant in the beam sea, while pitch motion is significant in the bow and stern seas. The second test shows that wave steepness has a linear relationship with roll and pitch motions in the bow and stern seas.*

1. Introduction

The number of vessels involved in marine accidents is increasing every year, with fishing vessel accidents accounting for 80% of all vessel accidents. Small fishing vessels refer to fishing vessels with a gross tonnage of fewer than 10 tons, and accidents involving small fishing vessels account for 71% of all fishing vessel accidents (Korea Maritime Safety Tribunal, 2021; Ministry of Oceans and Fisheries, 2020). Small fishing vessels are significantly affected even by small waves, leading to accidents, such as capsizing or sinking.

Meanwhile, domestic small fishing vessels are mainly built in small or medium-sized shipyards. Accordingly, they are built based on an existing mother vessel, relying on experience rather than using systematic procedures. Under this circumstance, it is difficult to conduct studies on hull forms to increase the efficiency of resistance performance and motion performance for small fishing vessels. Recently, more studies have been conducted on fishing vessels. However, most of these studies were focused on the operability, convenience, and speed of fishing vessels (Yu et al., 2010; Park et al., 2016a; Seok et al., 2018). In the case of small fishing vessels, the position of the transverse metacentric height changes frequently based on the fishing operation environment, affecting vessel stability, which is closely related to the roll motion of the vessel. Methods for analyzing the stability include numerical analysis, computational fluid dynamics analysis, experiments, and real ship tests. Im and Lee (2021) utilized computational fluid dynamics to analyze the motion response characteristics of small fishing vessels in regular waves based on the size of the fishing vessel and verified that the maximum value of the motion response moves to the long-wavelength region as the vessel speed increases in bow sea conditions, regardless of the size of the vessel. An experimental study on the motion response characteristics of small fishing vessels wavesteepness inclines in beam sea conditions verified that if only the resistance characteristics are considered for the chine line shape in the design of the hull of the vessel, the motion performance of the vessel can be degraded when it is damaged. In addition, it was confirmed that the position of the chine line shape significantly impacts vessel motion (Park et al., 2011). An analysis of seakeeping performance using multi-purpose fishing training vessels analyzed the performance of tasks under each sea condition and presented guidelines on adjusting the wave encounter angle an avoidance or changing the course of the vessel based on the sea condition (Ryu et al., 2019). The roll motion characteristics of a small fishing vessel were analyzed based on the change in the wave encounter angle and speed of the small fishing vessel. Although the roll motion response rapidly increased in a beam sea or stern sea, a real ship test verified that the motion period does not change much because of the

Received 14 September 2022, revised 29 November 2022, accepted 23 December 2022
Corresponding author DongHyup Youn: +82-51-974-5569, dhyoun@rims.re.kr

wave direction (Kang et al., 2007). The hull response characteristics of a stern-type trawler were measured according to wavesteepnes and wave direction via a real ship test when the trawler was drifting, sailing, and trawling. When the trawler was drifting, the maximum and significant values of the angle of roll motion increased as the wave height increased. However, both the maximum and significant values of the angle of pitch motion decreased (Park et al., 2016b).

In this study, we conduct a tank test experiment by simulating the drifting state of three small fishing vessels. First, we analyze the roll and pitch motion characteristics of these vessels in regular waves with uniform wave steepness. Then, we compare the characteristics of each fishing vessel with each other to present foundational data for the development of fishing vessels in terms of seakeeping performance. In addition, we analyze the roll and pitch motion characteristics of a 7-ton fishing vessel in a bow sea and a stern sea based on wave steepness to verify whether these characteristics increase linearly.

2. Experiment Methodology

2.1 Description of Setup and Model

Considering small fishing vessels account for 71% of recent fishing vessel accidents, we selected three sizes of fishing vessels under 10 tons, including a 3-ton (2.99), 7-ton (7.93), and 10-ton (9.77) class vessels, to analyze the response characteristics of small fishing vessels in regular waves (Im and Lee, 2021). Table 1 and Fig. 1 show the specifications and front view diagrams of the selected fishing vessels, respectively. Table 2 and Fig. 2 show the specifications and pictures of the model vessels used in the experiment, respectively. In addition, the scale ratios of the model vessels are 8.65 for the 3-ton class vessel, 9.46 for the 7-ton class vessel, and 11 for the 10-ton class vessel.

Table 1 Specifications of small fishing vessels

Item	3 G/T[1)] class	7 G/T class	10 G/T class
Length between perpendicular (m)	9.46	11.50	14.88
Breadth (m)	2.87	3.68	4.10
Draft (m)	0.54	0.83	0.80
Gross tonnage (G/T) (t)	2.99	7.31	9.77
Block coefficient (-)	0.34	0.58	0.46
Metacentric height (m)	0.84	0.88	1.28
Transverse radius of gyration (m)	1.15	1.47	1.64
Longitudinal radius of gyration (m)	2.37	2.88	3.72
Length to breadth ratio (-)	3.30	3.13	3.38
Breadth to draft ratio (-)	5.28	4.43	5.13

[1)] Gross tonnage

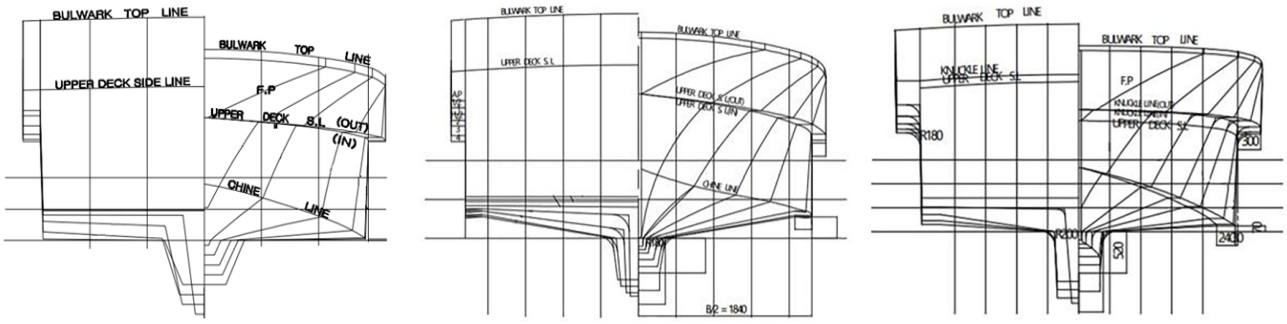

(a) (b) (c)

Fig. 1 Body plan: (a) 3 G/T class, (b) 7 G/T class, (c) 10 G/T class

Table 2 Specifications of the experimental models

Item	3 G/T[1)] class	7 G/T class	10 G/T class
Scale ratio (-)	8.65	9.46	11
Length between perpendicular (m)	1.5	1.5	1.5
Breadth (m)	0.33	0.39	0.37
Draft (m)	0.06	0.09	0.07
Metacentric height (m)	0.10	0.09	0.12
Transverse radius of gyration (m)	0.13	0.16	0.15
Longitudinal radius of gyration (m)	0.27	0.30	0.34

[1)] Gross tonnage

Fig. 2 Picture of experiment models (From the left, 3 G/T class, 7 G/T class, 10 G/T class)

2.2 Experimental Setup

The model experiment was conducted in the ocean engineering basin with a dimension of 28 × 22 × 2 m at the Research Institute of Medium and Small Shipbuilding (RIMS). The wave maker consisted of a system with a total length of 22.0 m, including 40 segments, a height of 1.0 m, and a width of 0.4 m. Moreover, wave absorber was installed on the opposite side of the wave maker to absorb incoming waves and prevent wave reflections at the boundary of the wave basin and to achieve interaction between the floating object and the wave by adjusting the infinite range of the fluid. The fishing vessel was located in the center of the basin, as shown in Fig. 3. To facilitate this study, the origin was located at the position of the wave maker at a constant water level. In addition, the coordinate system was designated by setting the horizontal direction of the wave maker as the x-coordinates and the positive numbers of the wave propagation direction as the y-coordinates. The four-point mooring was used with springs with a natural period greater than twice the maximum period of the model vessel to prevent the model vessel from being pushed away by waves. As a result, the springs did not affect the movement of the model vessel. In addition, the springs were fixed at the vertical center of gravity of the bow and stern to prevent the effect of the mooring point.

The following wave encounter angles (x) were used in the experiment—head sea, bow sea, beam sea, stern sea, and following sea conditions—as shown in Fig. 4. The wave encounter angle is 180º for the head sea condition and 0º for the stern sea condition.

The height of the waves was measured using a wire resistance-type wave probe. The wave height signal was converted into a voltage and sent to the data acquisition board in the computer. All data from the wave probe was measured at a sampling rate of 20 Hz. The motion characteristics of the fishing vessel were measured using alternating current (AC) electromagnetic-type motion measurement equipment, with data transmitted to a PC via radio frequency (RF) wireless communication. The motion measurement equipment can measure six degrees of freedom, but only heave, roll, and pitch motions were measured in this study. Fig. 5 shows the positions of the motion tracking equipment and gyro sensors installed on the model vessel.

Table 3 shows the regular wave conditions used in the experiment to analyze the response characteristics. The wave steepness was maintained, while the wave period, was varied from 0.6 s to 2.0 s at a uniform interval of 0.2 s to determine the wave number and wave height, H. The experiment was conducted at wave range of 1.76–5.88 s for the 3-ton class fishing vessel, 1.84–6.15 s for the 7-ton class fishing vessel, and 1.98–6.63 s for the 10-ton class fishing vessel. In Table 4, the wave period was maintained, while the wave steepness was varied from 0.05–0.11 at uniform intervals of 0.02 to analyze the response characteristics based on the wave steepness. This experiment was conducted with a wave period of 3.69 s using only the 7-ton fishing vessel.

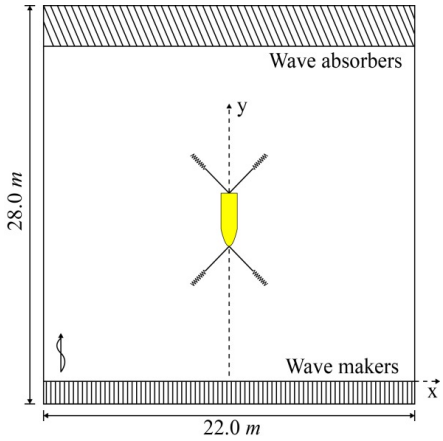

Fig. 3 Experiment layout at different views in the basin

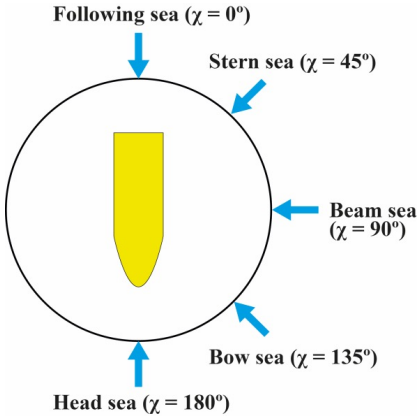

Fig. 4 Wave encounter angle

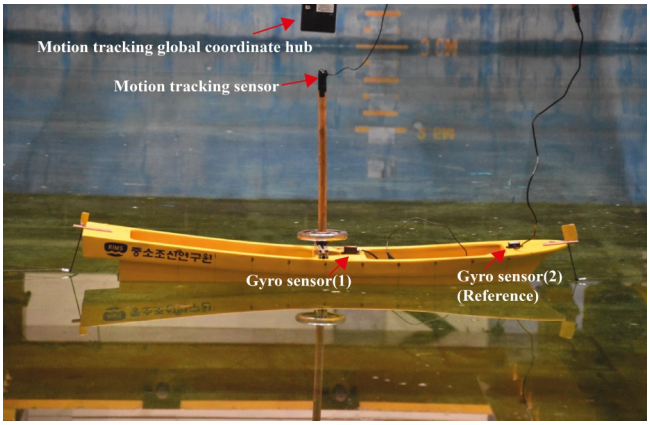

Fig. 5 View of the model-located sensor

Table 3 Experiment wave condition (same wave steepness)

No.	Wavesteepness (-)	Height (m)	Period (s)	Wave number (1/m)
1	0.05	0.042	0.6	2.365
2	0.05	0.056	0.8	1.773
3	0.05	0.070	1.0	1.419
4	0.05	0.084	1.2	1.182
5	0.05	0.098	1.4	1.013
6	0.05	0.112	1.6	0.887
7	0.05	0.126	1.8	0.788
8	0.05	0.141	2.0	0.709

Table 4 Experiment wave condition (same period)

No.	Wavesteepness (-)	Height (m)	Period (s)	Wave number (1/m)
9	0.05	0.084	1.2	1.182
10	0.07	0.118	1.2	1.182
11	0.09	0.152	1.2	1.182
12	0.11	0.186	1.2	1.182

2.3 Validation Studies

For regular wave validation, eight regular waves with the same wave steepness and different wave periods and four regular waves with the

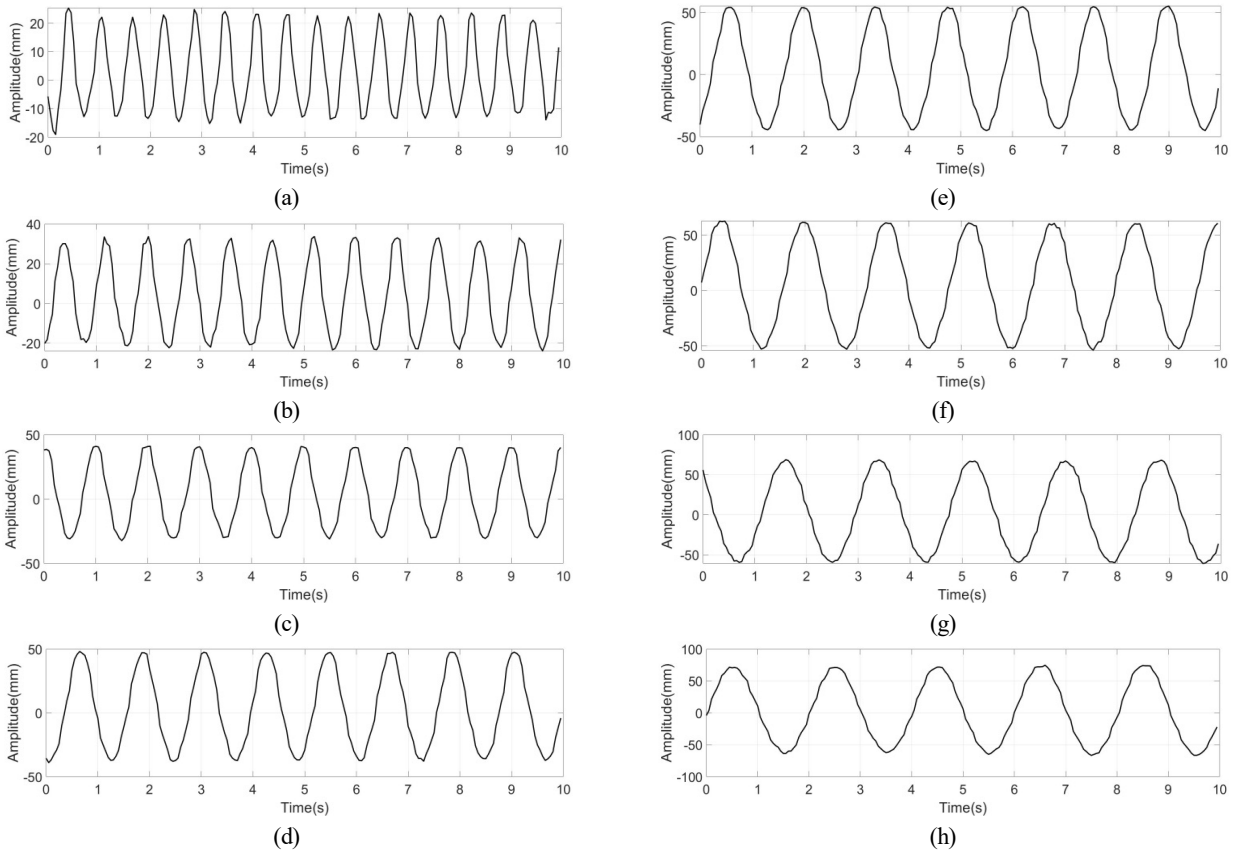

Fig. 6 Validation of incident wave (same wave steepness): (a) No. 1, (b) No. 2, (c) No. 3, (d) No. 4, (e) No. 5, (f) No. 6, (g) No. 7, (h) No. 8

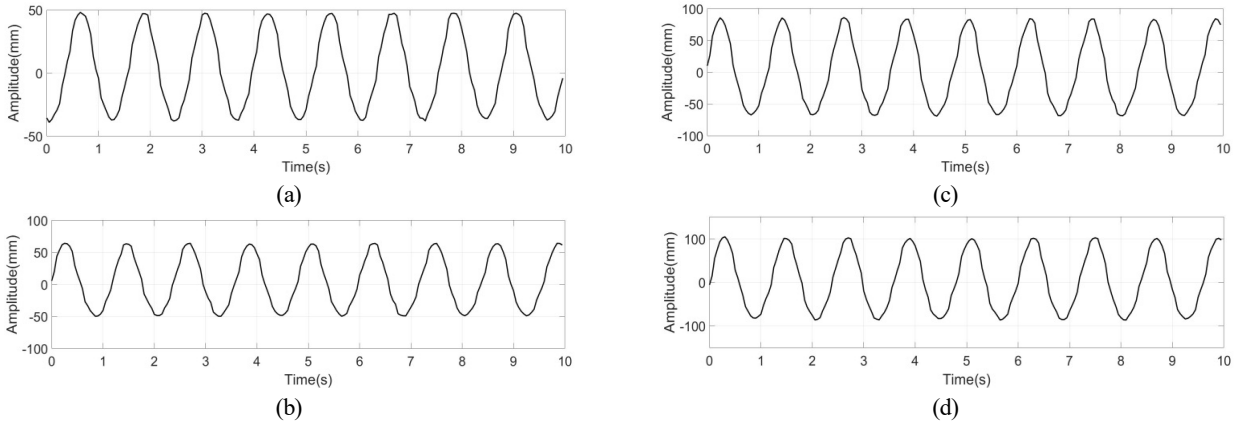

Fig. 7 Validation of incident wave (same period): (a) No. 9, (b) No. 10, (c) No. 11, (d) No. 12

same period and different wave steepness were generated in the wave tank with a depth of 2 m. The physical wave maker signal was converted into a voltage and sent to the data acquisition board, ensuring excellent repeatability of the experiment. The measurement time was set to less than or equal to 40 s to avoid the effect of reflected waves on the experimental results. At least 30 wave periods were generated for each wave, with 9−11 wave periods in a normal state selected. Figs. 6 and 7 show the wave heights for the validation of the incident waves.

3. Results and Discussion

3.1 Analysis of Motion in Regular Waves with the Same Wave Steepness

Figs. 8−10 show the experimental results of the heave, roll, and pitch motions in regular waves when the wave steepness remains the same. The graphs on the left, middle, and right show the experimental results for the 3-ton, 7-ton, and 10-ton class fishing vessels, respectively.

Fig. 8 shows the heave motion characteristics under different wave direction conditions. The size of the heave motion characteristics was similar to that of the incident waves as the wavelength increased. However, in the case of the beam sea (x = 90°), the heave motion characteristics were the largest at λ/D = 2.36 for all three fishing vessels (3, 7, and 10-ton class vessels). In addition, in the case of the 10-ton class fishing vessel, the motion characteristics were the largest at λ/D = 4.72 in the bow sea condition. Therefore, it is recommended that 10-ton class fishing vessels avoid bow seas when drifting.

Fig. 9 shows the roll motion characteristics under different wave direction conditions. Similar to the heave motion, the roll motion was also amplified in a specific region. High roll motion occurred at λ/D = 2.36 under the beam sea condition (x = 90°) for all three fishing vessels (3-ton, 7-ton, and 10-ton class vessels). In the case of the 10-ton class fishing vessel, significant motion characteristics were exhibited at λ/D = 4.13, which is a longer wavelength. Based on this result, it is determined that λ/D = 4.13 is the natural period of the roll

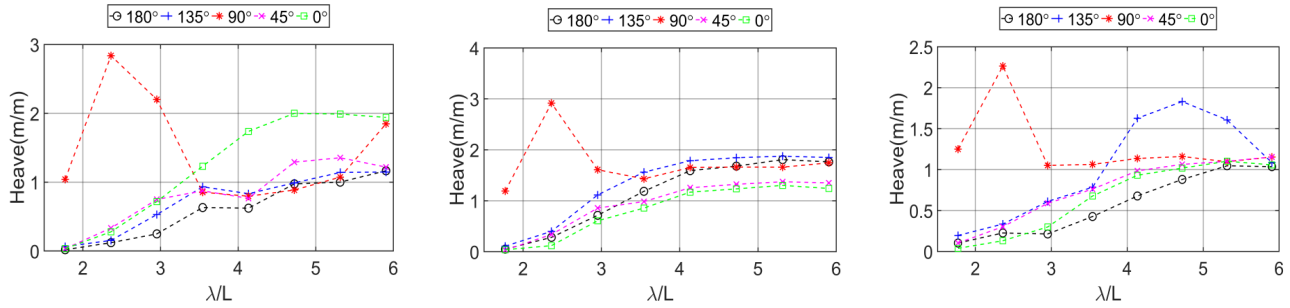

Fig. 8 Heave motions: (a) 3 G/T class, (b) 7 G/T class, (c) 10 G/T class

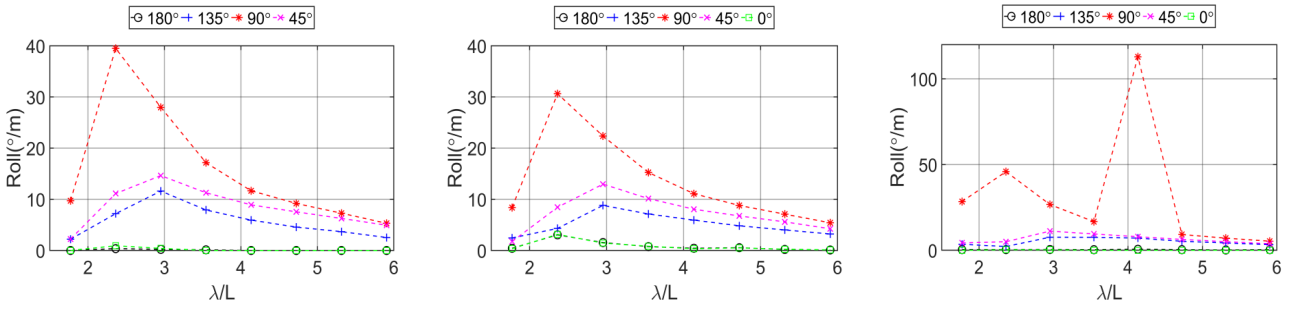

Fig. 9 Roll motions: (a) 3 G/T class, (b) 7 G/T class, (c) 10 G/T class

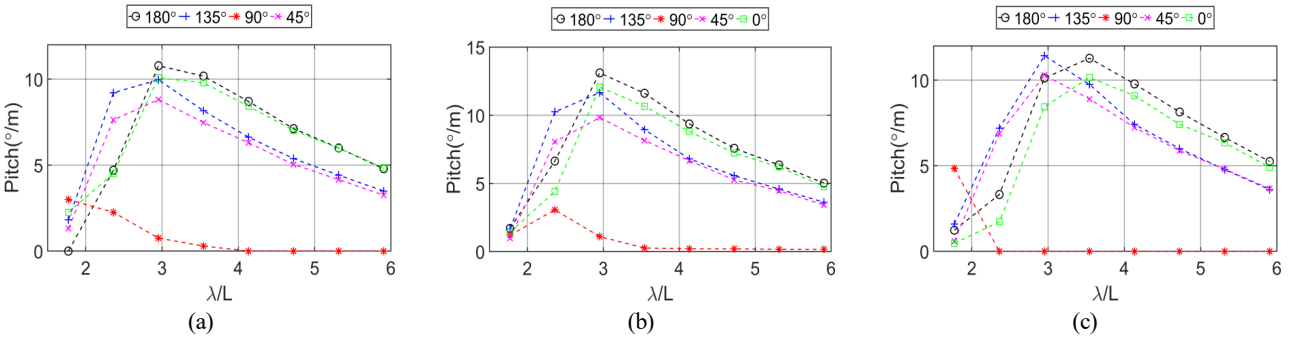

Fig. 10 Pitch motions: (a) 3 G/T class, (b) 7 G/T class, (c) 10 G/T class

motion for the 10-ton fishing vessel. Moreover, 10-ton fishing vessels must avoid the natural period of the roll motion when drifting as it could be dangerous when a 10-ton fishing vessel encounters the natural period of the roll motion. In addition, it is necessary to change the direction of the fishing vessel since the fishing vessel exhibited relatively high roll motion characteristics at $\lambda/D = 2.95$ in a head sea ($x = 135°$) and stern sea ($x = 45°$).

Fig. 10 shows the pitch motion characteristics under different wave direction conditions. The 3-ton class and 7-ton class fishing vessels exhibited high pitch motion characteristics at $\lambda/D = 2.95$ in a head sea ($x = 180°$) and following sea ($x = 0°$), while the 10-ton class fishing vessel exhibited high pitch motion characteristics at $\lambda/D = 3.54$ because of differences in the length of the fishing vessels; however, it does not represent a large difference in terms of wavelength. Therefore, caution must be exercised for real vessels in the wave period between 3.31–3.98 s, equivalent to $\lambda/D = 2.95$–3.54.

3.2 Analysis of Motion in Regular Waves with Different Wave Steepness

Figs. 11 and 12 show the motion characteristics of the 7-ton class fishing vessel in a bow sea ($x = 135°$) and stern sea ($x = 45°$) when the wave steepness is varied in regular waves.

The size of the roll and pitch motions increased as the wave steepness increased in both a bow sea ($x = 135°$) and stern sea ($x = 45°$). In addition, both the roll and pitch motions increased linearly as the wave steepness increased at uniform intervals. The period was set the same as the period of the incident wave, i.e., 1.2 s; consequently, the period of the motions was also the same. Based on this phenomenon, if the wave height is substituted in the motion phenomena of Figs. 8–10, we can obtain the motion characteristics of the wave height.

Fig. 13 shows the characteristics of the bow sea ($x = 135°$) and stern sea ($x = 45°$) according to the wave steepness as the roll and $x$pitch

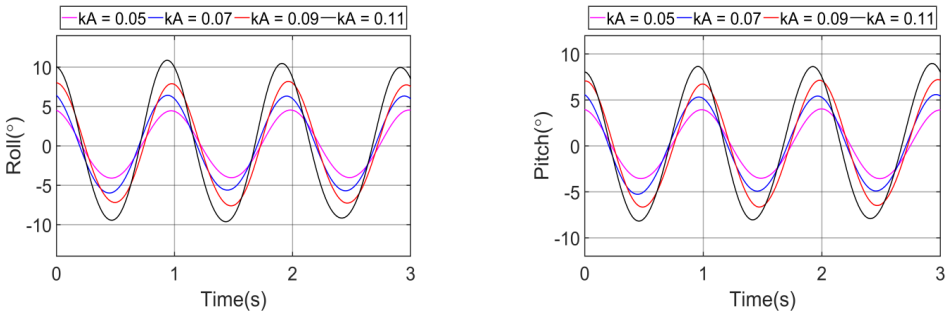

Fig. 11 Motion of bow sea ($x = 135°$): (a) Roll motion, (b) Pitch motion

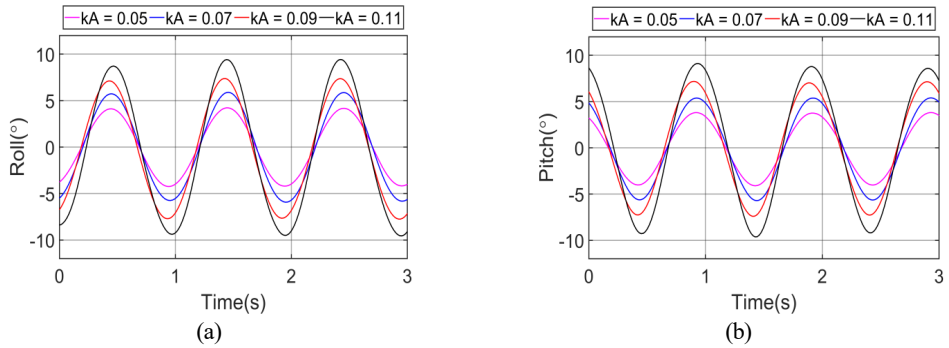

Fig. 12 Motion of stern sea ($x = 45°$): (a) Roll motion, (b) Pitch motion

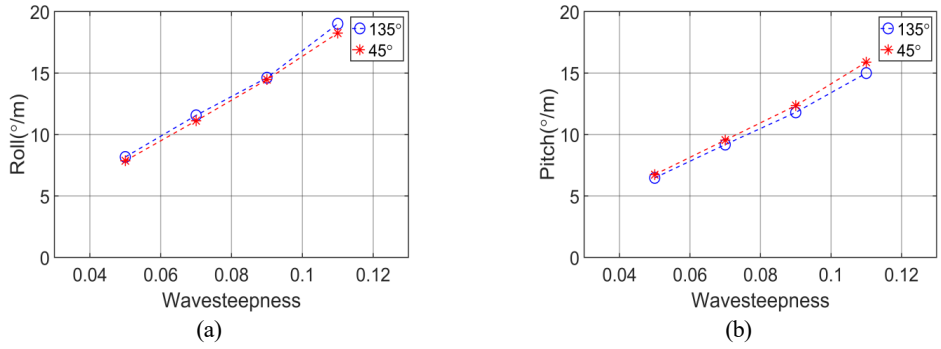

Fig. 13 Motion according to wavesteepness: (a) Roll motion, (b) Pitch motion

motions. The characteristics of both the bow sea (x = 135°) and the stern sea (x = 45°) increased linearly as the wave steepness increased. However, in the case of the roll motion, the characteristics of the bow sea were larger, while the characteristics of the stern sea were larger for the pitch motion. These phenomena can be caused by the effect of the chine of the fishing vessel reducing the roll motions in the stern sea (x = 45°).

4. Conclusions

In this study, we conducted wave tank tests on three small fishing vessels by simulating drifting conditions. The characteristics of the roll and pitch motions were analyzed in regular waves with the same wave steepness. We analyzed the seakeeping performances by comparing the characteristics of each vessel. We verified whether the roll and pitch motion characteristics increased linearly and drew the following conclusions by analyzing the roll and pitch motion characteristics of a 7-ton class fishing vessel according to the wave steepness in a bow sea and stern sea.

(1) The largest heave motions occur when λ/D = 2.36 in a beam sea when 3-ton, 7-ton, and 10-ton class fishing vessels were drifting. Therefore, such a fishing vessel should change its direction towards the bow sea or stern sea direction. Large roll motions also occur when λ/D = 2.36 in a beam sea. In the case of the 10-ton class fishing vessel, huge roll motion characteristics are exhibited at λ/D = 4.72. Therefore, 10-ton class fishing vessels should avoid a beam sea when drifting. The largest pitch motions occur in a head sea and a following sea. As the wavelength is longer than the size of the vessel, similar characteristics are exhibited. Fishing vessels should turn in a direction other than a beam sea, which generates large roll motions because roll motions are larger than pitch motions in all fishing vessels.

(2) We checked the roll and pitch motion characteristics by varying the wave steepness while keeping the wave period the same in a bow sea and stern sea. Considering the characteristics increased linearly, we can substitute the wave height to obtain the motion characteristics of the wave height.

In the future, we plan to experimentally analyze the change in the motion characteristics based on the change in the center of gravity through regular and irregular waves to use the study findings as foundation data for improving the stability of fishing vessels.

Conflict of Interest

No potential conflict of interest relevant to this article was reported.

Funging

This research was supported by a grant (20015029) of Regional Customized Disaster-Safety R&D Program, funded by Ministry of Interior and Safety (MOIS, Korea).

References

Im, N. K., & Lee, S. M. (2021). A study on motion response of small fishing vessels according to various tonnage in regular waves. *Journal of the Korean Society of Marine Environment and Safety, 27*(6), 832−838. https://doi.org/10.7837/kosomes.2021.27.6.832

Kang, I. K., KIM, H.S ., KIM, M. S, Lee, Y. W, Kim, J. C., Jo, H. J., & Lee, C. K. (2007). Characteristics on the rolling response of a small fishing boat according to the waves and the ship's speed. *Journal of the Korean Society of Fisheries and Ocean Technology, 43*(1), 62−70. https://doi.org/10.3796/KSFT.2007.43.1.062

Korea Maritime Safety Tribunal. (2021). *Statics of marine accidents.* http://www.kmst.go.kr/eng/page.do?menuIdx=227

Ministry of Oceans and Fisheries (2020). *Standard of structure and facility of small fishing vessel under G/T 10 tone*. https://www.mof.go.kr/statPortal/cate/partStat.do?codeCateId0140000

Park, B. S., Kang, I. K., Ham, S. J., Park, C. W., Kim, S. H., & Cho, H. K. (2016a). The main factor and counterplan for marine casualties of fishing vessel according to the type of fishing gear in Korea. *Journal of the Korean Society of Fisheries and Ocean Technology, 52*(3), 232−240. https://doi.org/10.3796/KSFT.2016.52.3.232

Park, C. W., Kim, J. W., Kim, H. S., & Kang, I. K. (2016b). Characteristics on the response of the stern trawler according to the state of its operation. *Journal of the Korean Society of Fisheries and Ocean Technology, 52*(4), 339−346. https://doi.org/10.3796/KSFT.2016.52.4.339

Park, R. S., Kim, S. G., & Lee, J. B. (2011). Study on Motion Response Characteristics for Large Inclined State of Small Fishing Vessel in Beam Sea Condition. *Journal of Ocean Engineering and Technology, 25*(6), 17−22. https://doi.org/10.5574/KSOE.2011.25.6.017

Ryu, K. J., Park, T. S., Kim, C. W., & Park, T. G. (2019). A study on the development of multi-purpose fisheries training ship and result of seakeeping model test. *Journal of the Korean Society of Fisheries and Ocean Technology, 55*(1), 74−81. https://doi.org/10.3796/KSFOT.2019.55.1.074

Seok, J., Park, J. C., Park, D. W., & Yang, Y. J. (2018). A study of roll performance for 2.99 ton class fishing boat with appendages using computational fluid dynamics. *Journal of Advanced Marine Engineering and Technology, 42*(4), 293−297. https://doi.org/10.5916/jkosme.2018.42.4.293

Yu, J. W., Lee, Y. G., Jee, H. W., Park, A. S., Choi, Y. C., Ha, Y. J., & Jeong, K. L. (2010). A Study on the Improvement of Resistance Performance for G/T 4.99ton Class Korean Coastal Fishing Boats. *Journal of the Society of Naval Architects of Korea, 47*(6), 757−762. https://doi.org/10.3744/SNAK.2010.47.6.757

Author ORCIDs

Author name	ORCID
Youn, DongHyup	0000-0001-9399-4945
Choi, LeeChan	0000-0003-1143-8414
Kim, JungHwi	0000-0001-9478-5483

KSOE

Journal of Ocean Engineering and Technology 37(1), 8-19 February, 2023
https://doi.org/10.26748/KSOE.2022.033

pISSN 1225-0767
eISSN 2287-6715

Original Research Article

Numerical Analysis for Motion Response of Modular Floating Island in Waves

Hyo-Jin Park[1], Jeong-Seok Kim[2] and Bo Woo Nam[3]

[1]*Graduate student, Department of Naval Architecture and Ocean Engineering, Seoul National University, Seoul, Korea*
[2]*Junior Researcher, Eco-friendly Ocean Development Research Division, Korea Research Institute of Ships & Ocean Engineering, Deajeon, Korea*
[3]*Assistant Professor, Department of Naval Architecture and Ocean Engineering, Seoul National University, Seoul, Korea*

KEYWORDS: Modular floating island, Pontoon type module, Motion response in wave, Higher-order boundary element method

ABSTRACT: *In recent years, modular-type floating islands have been considered as a promising option for future ocean space utilization. A modular floating island consists of a number of standardized pontoon-type modules and connectors between them. In this study, the motion responses of a modular floating island in waves was investigated based on frequency-domain numerical analysis. The numerical method is based on the potential flow theory and adopts a higher-order boundary element method with Green's function. First, motion RAOs were directly compared with the model test data by reference to validate the present numerical method. Then, numerical investigations were conducted to analyze the motion characteristics of the floating island by considering various modules shapes and arrangements. It was found that motion responses were reduced in a single central module compared to when divided central modules were used. Finally, the effect of modular arrangement on the motion responses in irregular waves was discussed. It was confirmed that multiple-layer outer modules are more effective in calming the central module than using single-layer outer modules, except under very long period conditions.*

1. Introduction

The demand for ocean space utilization is rising because of the recent rise in sea level and population density in coastal regions. As a strategy to exploit the ocean space, expanding land space through land reclamation has been widely adopted. However, in terms of environmental protection and economic feasibility, floating islands have been actively studied (Yeh et al., 2015; Lu et al., 2015). In Japan, floating islands have been used for airports and fuel storage facilities because floating island technology can minimize environmental damage compared to the coastal reclamation development (Wang and Tay, 2011). In South Korea, floating island structures have been employed as maritime recreational amenities in combination with waterfront infrastructure projects. Furthermore, floating islands are used as salmon farming facilities in Canada, Chile, Norway and the United States. Recently in Europe, research projects on multi-purpose very large offshore structures for dwelling, fishing, energy generation and storage functions have been launched and related research is being conducted.

Very large floating structures (VLFS) for floating islands have been generally classified into semi-submersible and pontoon types. A semi-submersible VLFS has an topside platform above the water surface, which is suitable for use in the open ocean. On the other hand, a pontoon type VLFS has a floating platform on the water surface, which is appropriate for mild seas (Wang and Tay, 2011). Furthermore, a pontoon type VLFS has the advantages of simple structure, good stability, low manufacturing and maintenance costs, and easy repair (Lamas-Pardo et al., 2015). So far, many studies on the integrated pontoon-type VLFS have been conducted focusing on structural safety evaluation considering the hydroelastic response (Kashiwagi, 1998; Kim et al., 2014). This is because the structural deformation of the pontoon-type VLFS is rather substantial owing to the small draft compared to the length.

Some studies have been conducted regarding the modular floating island, which links multiple modules through connectors. Watanabe et al. (2004) pointed out that most floating islands, including the integrated type, need to be manufactured by combining a number of standardized modules in order to overcome difficulties in

Received 26 September 2022, revised 28 November 2022, accepted 1 December 2022
Corresponding author Bo Woo Nam: +82-2-880-7324, bwnam@snu.ac.kr

manufacturing, transportation, and installation. This implies that an integrated floating island can be changed into the modular floating island by introducing the appropriate connectors. Wu et al. (1993) and Riggs et al. (2000) performed numerical analysis on the hydroelastic response of a semi-submersible VLFS composed of five modules. Fu et al. (2007) reported the numerical results that the hydroelastic response of the integrated floating island can be changed as the pontoon type module was connected via flexible connectors. Gao et al. (2011) showed the hydroelastic response and load of a pontoon- type VLFS are reduced by applying a hinge connector that allows some floater movement under short wave conditions. This suggests that the modular method using flexible connectors, which allows some relative movement between modules, has an advantage over the integral method using rigid connectors to restrain the VLFS in terms of hydroelastic response and load.

Recently, active research is now being performed to utilize pontoon-type VLFS in the form of a modular floating island. Zhang et al. (2015) conducted a numerical study on a marine airport in which two to five pontoon modules were connected via flexible connectors. In Europe, a modular floating island composed of 87 pontoon modules was proposed through the "Space@Sea Project". The motion response of a modular floating island was described by Waals et al. (2018) who performed a series of model test. Otto et al. (2019a) conducted a potential flow-based numerical analysis in the frequency domain. Otto et al. (2019b) evaluated the motion response of the module and the load acting on the connector with different dimensions of the floating island, and demonstrated that module size has a significant effect on the motion response of a modular floating island. However, their study did not closely examine the effects of module arrangement on the motion response and load of the floating island.

Numerical models for a modular floating island can be divided into a rigid module & flexible connector model and a flexible module & flexible connector model depending on whether the flexibility of the module is considered. Wu et al. (1993) evaluated the hydroelastic response of a modular floating island composed of five semi-submersible modules by applying a flexible module and flexible connector model. Zhang et al. (2015) analyzed motion response by applying a rigid module and flexible connector model to a marine airport composed of multiple pontoon type modules. In order to apply the rigid module and flexible connector model, the hydrodynamic coefficients were derived using a linear wave theory and an eigen-function expansion method. Riggs et al. (2000) calculated a similar motion response and connector force using a rigid module and flexible connector model as well as a flexible module and flexible connector model for a modular floating island composed of 300 m long modules. This demonstrated that the motion response of a modular floating island can be evaluated based on a rigid module and flexible connector model, which is a relatively simple model. Otto et al. (2019a) analyzed motion response by applying the modular floating island proposed by the Space@Sea project as a rigid module and flexible connector model. Waals et al. (2018) verified the validity of the analysis technology through comparison with the model test results.

In this study, the wave-induced motion response of a floating island composed of a number of pontoon-type modules was analyzed based on a potential flow-based numerical analysis method in the frequency domain. In Section 2, a numerical method was presented to evaluate the motion response of a modular floating island. The modular floating island was modeled with a number of rigid modules and flexible connectors by applying potential flow-based hydrodynamic coefficients. In Section 3, the validity of the present numerical method was examined by comparing it with the existing model test results of a modular floating island (Waals et al., 2018). In Section 4, the configuration of the modular floating island is divided into 'central modules', 'tail module', and 'outer modules'. Then the effects of the arrangement and size of each module on the motion characteristics of floating islands in waves were discussed.

2. Numerical Analysis Method

2.1 Higher-order Boundary Element Method

This study applied a potential flow model to analyze the motion response of floating bodies in waves. In the potential flow theory where inviscid, incompressible fluid and irrotational flow are assumed, the boundary value problem for linear velocity potential is formulated as Eqs. (1) to (5).

$$\nabla^2\phi = 0 \quad \in \Omega \tag{1}$$

$$\frac{\partial\phi}{\partial t} + g\zeta = 0,\ \frac{\partial\zeta}{\partial t} - \frac{\partial\phi}{\partial z} = 0 \quad on\ z = 0 \tag{2}$$

$$\frac{\partial\phi}{\partial n} = v_n \quad on\ S_B \tag{3}$$

$$\frac{\partial\phi}{\partial n} = 0 \quad on\ S_W \tag{4}$$

$$\lim_{kr\to\infty} \sqrt{kr}\left(\frac{\partial\phi_j}{\partial r} - k\phi_j\right) = 0 \tag{5}$$

Here, Ω denotes the entire fluid domain. S_B and S_W represent the boundaries of the floating body surface and the sea bottom, respectively. ϕ is the linear velocity potential for the flow. g denotes the gravitational acceleration, and ζ denotes the wave height. n and v_n are the normal vector and normal velocity defined on the floating body surface or the sea bottom, respectively. z denotes the coordinate in the vertical direction with respect to the free surface. k and r are the wave number and the diameter of the boundary, respectively. Eq. (1) is the Laplace equation, which is the governing equation for the fluid domain based on the potential flow theory. Eq. (2) indicates the dynamical and kinematic boundary conditions on the free surface, respectively. Eqs. (3) and (4) are the non-penetration boundary conditions for the floating body surface and sea bottom, respectively. Eq. (5) corresponds to the

radiation condition at the far field.

To solve the linear boundary value problem described above, the higher-order boundary element method was applied in this study. To this end, the floating body surface was discretized with 9-node biquadratic elements. Numerical solutions with the higher-order boundary element method have been found to have higher accuracy and convergency than the constant panel method (Choi and Hong, 2002). It has also been extensively applied to the problem of multiple floating bodies with complex shapes (Nam and Hong, 2021). The following equation represents the integral equation for the boundary value problem using the wave Green function:

$$\phi(\vec{r_0})[1+\nu\iint_{S_B} G(\vec{r},\vec{r_0})dS]+\iint_{S_B}[\phi(\vec{r})-\phi(\vec{r_0})]G(\vec{r},\vec{r_0})dS = \iint_{S_B}\phi_n(\vec{r})G(\vec{r},\vec{r_0})dS \quad (6)$$

where $\vec{r_0}$ denotes the coordinates of the source point distributed on the panel.

Complex flows occur in the narrow gap space between the modules of a modular floating island. Strong vortex is generated at the edge of the module, and the viscous drag becomes significant. To consider the damping effect of this flow, the modified body boundary condition in E. (7) was applied to reflect the viscous damping effect, which is similar to the method applied to the sloshing flow problem by Zalar et al. (2007).

$$\frac{\partial\phi}{\partial n}=i\epsilon k_0\phi+v_n \quad on\, S_B \quad (7)$$

where $k_0(=\omega^2/g)$ is the wave number at infinite depth and ω is the wave frequency. ϵ is a parameter that controls the degree of numerical damping. In this study, 0.02 was applied for ϵ.

2.2 Evaluation of Stiffness Matrix

With regard to mooring and connector problems between multiple floating bodies, a linear stiffness matrix can be derived considering the pretension and spring stiffness components (Nam and Hong, 2021). The first stiffness component is proportional to the pretension and the change in the angle of the mooring line, while the second stiffness component is proportional to the change in the length of the mooring line. In this study, complex connectors between modules of the floating island were simplified with equivalent springs, and the motion of the floating island was analyzed in consideration of the linear stiffness matrix by the equivalent springs. To derive the global stiffness matrix of the floating island, the local stiffness matrix is first derived according to the connectors' positions between unit modules, and then it is converted into a global stiffness matrix by applying a conversion matrix. Subsequently, the same process is repeated for all connectors to finally obtain the total global stiffness matrix of the modular floating island.

First, a stiffness component for the connector between the modules J_1 and J_2 can be represented as a local stiffness matrix ($[K^e]_{3\times6}$) as follows:

$$\begin{Bmatrix}F_{n+1}\\F_{n+2}\\F_{n+3}\end{Bmatrix}=[K^e]_{3\times6}\begin{Bmatrix}s_{n+1}\\s_{n+2}\\s_{n+3}\\s_{n+4}\\s_{n+5}\\s_{n+6}\end{Bmatrix},\quad [K^e]_{3\times6}=\begin{bmatrix}-k_x & 0 & 0 & k_x & 0 & 0\\ 0 & -k_y & 0 & 0 & k_y & 0\\ 0 & 0 & -k_z & 0 & 0 & k_z\end{bmatrix} \quad (8)$$

where F_{n+1}, F_{n+2}, and F_{n+3} are the restoring forces acting on the module J_1, while F_{m+1}, F_{m+2}, and F_{m+3} are the restoring forces acting on the module J_2. $n=6\times(J_1-1)$ and $m=6\times(J_2-1)$ are integers for the degree of freedom of the two modules, respectively. s_n is the local motion of nth degree of freedom at the connector position, and (k_x,k_y,k_z) are the components of the spring stiffness. Then, the local stiffness matrix can be converted into a global stiffness matrix using a transformation matrix ($[T^e]_{6\times12}$) as follows:

$$\begin{Bmatrix}s_{n+1}\\s_{n+2}\\s_{n+3}\\s_{n+4}\\s_{n+5}\\s_{n+6}\end{Bmatrix}=[T^e]_{6\times12}\begin{Bmatrix}\xi_{n+1}\\\xi_{n+2}\\\xi_{n+3}\\\xi_{n+4}\\\xi_{n+5}\\\xi_{n+6}\\\xi_{m+1}\\\xi_{m+2}\\\xi_{m+3}\\\xi_{m+4}\\\xi_{m+5}\\\xi_{m+6}\end{Bmatrix},\ [T^e]_{6\times12}=\begin{bmatrix}1&0&0&0&z_1&-y_1&0&0&0&0&0&0\\0&1&0&-z_1&0&x_1&0&0&0&0&0&0\\0&0&1&y_1&-x_1&0&0&0&0&0&0&0\\0&0&0&0&0&0&1&0&0&0&z_2&-y_2\\0&0&0&0&0&0&0&1&0&-z_2&0&x_2\\0&0&0&0&0&0&0&0&1&y_2&-x_2&0\end{bmatrix} \quad (9)$$

where (x_1,y_1,z_1) and (x_2,y_2,z_2) correspond to the positions where the connectors of modules J_1 and J_2 are attached. Considering the rotation matrix ($[R^e]_{3\times3}$) for the moment of rotational motion, the stiffness matrix ($[K]$) by the connector can be calculated as follows:

$$\begin{Bmatrix}F_{n+1}\\F_{n+2}\\F_{n+3}\\F_{n+4}\\F_{n+5}\\F_{n+6}\\F_{m+1}\\F_{m+2}\\F_{m+3}\\F_{m+4}\\F_{m+5}\\F_{m+6}\end{Bmatrix}=\begin{bmatrix}[K^e]_{3\times6}[T^e]_{6\times12}\\ [R^e]_{3\times3}[K^e]_{3\times6}[T^e]_{6\times12}\\ -[K^e]_{3\times6}[T^e]_{6\times12}\\ -[R^e]_{3\times3}[K^e]_{3\times6}[T^e]_{6\times12}\end{bmatrix}\begin{Bmatrix}\xi_{n+1}\\\xi_{n+2}\\\xi_{n+3}\\\xi_{n+4}\\\xi_{n+5}\\\xi_{n+6}\\\xi_{m+1}\\\xi_{m+2}\\\xi_{m+3}\\\xi_{m+4}\\\xi_{m+5}\\\xi_{m+6}\end{Bmatrix}=[K]\begin{Bmatrix}\xi_{n+1}\\\xi_{n+2}\\\xi_{n+3}\\\xi_{n+4}\\\xi_{n+5}\\\xi_{n+6}\\\xi_{m+1}\\\xi_{m+2}\\\xi_{m+3}\\\xi_{m+4}\\\xi_{m+5}\\\xi_{m+6}\end{Bmatrix}$$

$$\text{where, } [R^e]_{3\times3}=\begin{bmatrix}0&-z_1&y_1\\z_1&0&-x_1\\-y_1&x_1&0\end{bmatrix} \quad (10)$$

3. Validation of Numerical Method

3.1 Module Specifications

To validate the numerical method of this study, the present calculation results are directly compared with the model test data on modular floating islands by Waals et al. (2018). A model test was conducted for a floating island made of modules in the shape of an equilateral triangular prism of two sizes (Fig. 1) at MARIN (Maritime Research Institute Netherlands) by Waals et al. (2018). In this study, this modular floating island concept is referred to as the 'MARIN model'. The principle dimensions of the triangle modules by Waals et al.(2018) are shown in Table 1. Here, the dimensions are based on the real-scale values which are obtained by converting the model test dimensions by considering the model test scale ratio (1:250). As shown in Table 1, the dimensions of a small triangle module with a length of 237 m are listed in the first column, and the dimensions of a large triangle module with a length of 487 m are listed in the second column. Here, the distance between the triangle modules was assumed as 7.5 m, which is the length in which the four little triangle modules has the same size as the giant triangle module. This is approximately 2% more than the 7.35 m by Waals et al. (2018). The same radius of gyration as Waals et al. (2018) was used for present numerical analysis, which corresponds to about 68% of the radius of gyration in the case of a uniform mass distribution. In this study, a hexagon module was newly introduced to check the effect of the central module arrangements. In this case, the length parameters of the hexagon modules were determined to match the combined form of six big triangle modules. By extending the radius of gyration of the triangle modules, the radius of gyration of hexagon modules was calculated, which also corresponds to 68% of the radius of gyration of hexagon modules with a homogeneous mass distribution. The center of gravity in the vertical direction of the triangle and hexagon modules was assumed as the same as the still water level. The shape and panel distribution of the modules are depicted in Fig. 2. Because the floating island should be represented by a number of modules, it is necessary to determine the number of panels per module considering not only the accuracy of the solution but also the efficiency of the calculation. The grid convergence for triangle modules was analyzed in this work, and the number of panels (elements) was determined to have an inaccuracy of less than 0.5% based on motion response. Triangle modules were discretized with 45 higher-order elements in total, and the hexagonal module was represented by 198 elements. In the vertical direction, a single higher order element was applied to both triangle modules and hexagon modules.

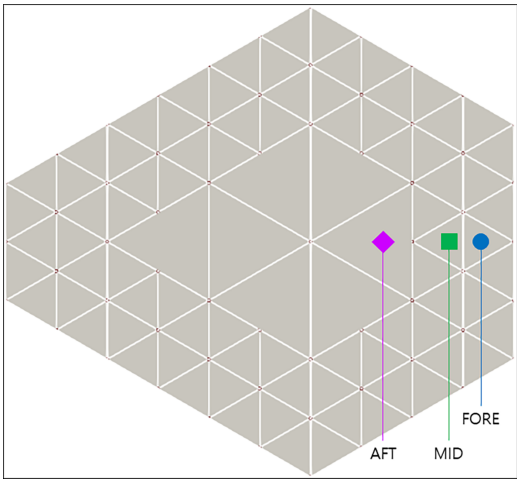

Fig. 1 Module arrangements of MARIN model (Waals et al, 2018)

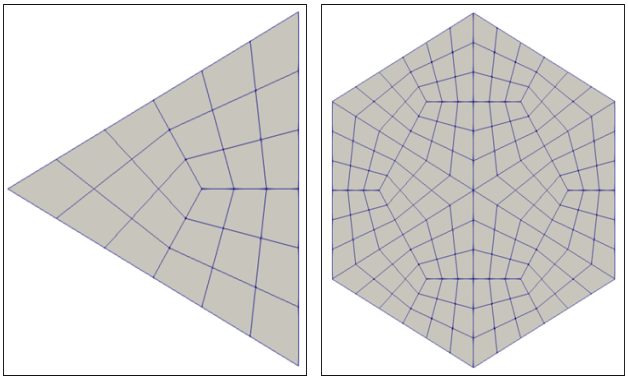

(a) (b)

Fig. 2 Panel distributions of triangle and hexagon module: (a) Triangle module; (b) Hexagon module.

Table 1 Principal dimensions of the floating structure modules

Item	Small triangle	Large triangle	Hexagon
Displacement (m^3)	2.171×10^5	9.166×10^5	5.697×10^6
Length (m)	237	487	495.66
Longitudinal length (m)	$L_{x,small}$ = 205.25	$L_{x,large}$ = 421.75	$L_{x,hexagon}$ = 858.51
Draft (m)	8.925	8.925	8.925
Kxx[1] (m)	27.3	67.54	153.71
Kyy[2] (m)	32.6	67.54	153.71
Kzz[3] (m)	40.9	94.85	217.38

[1] Radius of gyration about x axis
[2] Radius of gyration about y axis
[3] Radius of gyration about z axis

3.2 Connectors Between Modules

Waals et al. (2018) used fenders and springs to represent connectors between unit modules of the floating artificial island in their model test. The fender provides elastic force only when compressed, generating a supporting force that keeps the spacing between modules from narrowing. The spring, on the other hand, provides a force proportional to displacement equally during compression and relaxation, which generates a restoring force to maintain the separation distance between modules. During the model test, it was confirmed that the fender remained in contact with the module due to the initial tension of the springs. In this case, the fender was inserted to receive force perpendicular to the module's side, and a number of springs were installed at an angle of 45 degrees on the facing surface of the adjacent module. Thus, an equivalent spring corresponding to the fender and the springs was introduced to link the modules in this numerical analysis, and the stiffness of the spring used in the analysis was 187,250 kN/m. In addition, although the spring and fender are utilized for the horizontal connection, vertical frictional force may arise owing to the compressed fender. As a result, even for vertical motion, the restoring force must be considered. Otto et al. (2019b) conducted a numerical study by modeling the vertical shear force induced by the connector with a force proportionate to vertical deformation. In this study, a vertical spring with a stiffness of 87,500 kN/m, which corresponds to about 47% of the stiffness on the horizontal plane, was used in the numerical analysis.

3.3 Validation

To validate the present numerical method, the calculated heave and pitch motion RAOs (response amplitude operator) of the unit floating modules were directly compared with the measured experimental data of the model test. The representative positions for the motion responses of three floating modules were labeled as 'AFT', 'MID', and 'FORE', and each position is remarked in Fig. 1. Fig. 3 shows the comparison results of the heave and pitch motion RAOs of three floating modules. The numerical analysis results are denoted by lines, whereas the model test results are represented by symbols. The numerical results are based on the frequency-domain analysis, where the motion RAO values are calculated individually for each frequency. In the case of the model test, the motion RAOs of the modules were estimated by using the motion response spectra and wave spectrum measured from the irregular wave test. The numerical and experimental data show a slight difference in motion RAOs around a wave frequency of 0.5 rad/s, but overall motion responses show a similar tendency. The heave motion RAO of the FORE and MID modules is approximately 1.5 around the wave frequency of 0.3 rad/s ($\lambda/L_{x,small} = 3.34$), whereas the AFT module showed a smaller heave RAO than the other modules at all frequencies. The small motion response of the AFT module can be interpreted as an insignificant wave excitation effect due to its relatively large size and location away from the outside. In higher frequencies than 0.3 rad/s, both numerical and experimental results showed a decreasing tendency of the heave and pitch RAOs as the wave frequency increased. Looking at the module's pitch RAO, the closer the module is to the incident wave direction, the larger the peak response occurs at a higher wave frequency. From the results of Fig. 3, it can be confirmed that, even though the FORE module and MID module are the same size, the magnitude of the response and the peak period differ based on the location and connection method.

4. Results and Discussions

According to the planar arrangement of the modules, the modular floating island can be divided into three parts, as illustrated in Fig. 4. The "central modules" are the large triangle modules that make up the central section. The term "tail module" was used to describe the large triangle module that is located behind the central modules, while the word "outer modules" was used to describe the outermost modules that surround the tail module and the central modules. In this study,

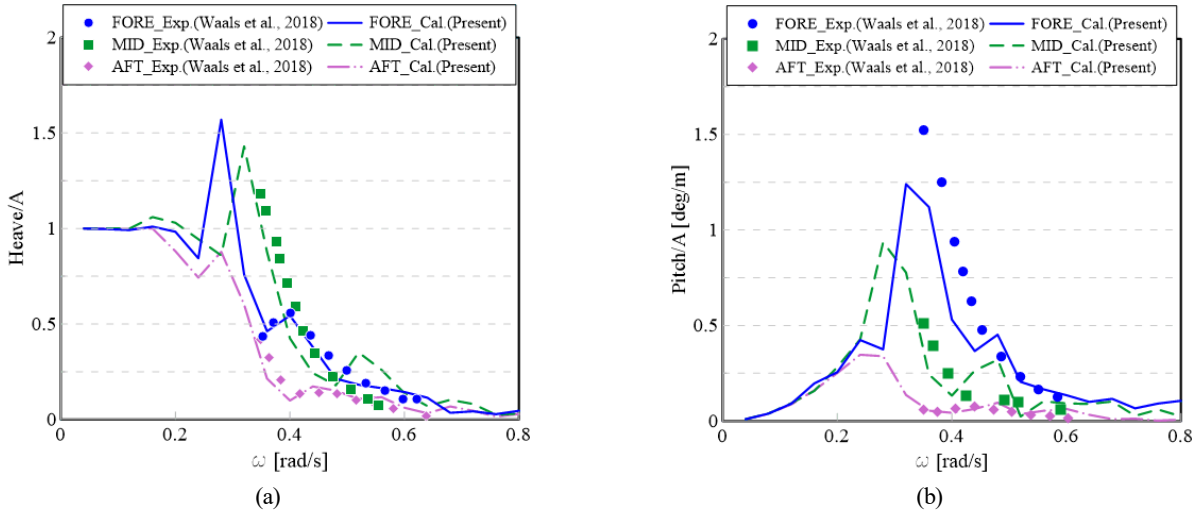

(a) (b)

Fig. 3 Comparison of motion RAOs of the modules (FORE, MID and AFT) between the experimental model and present numerical model: (a) Heave motion; (b) Pitch motion.

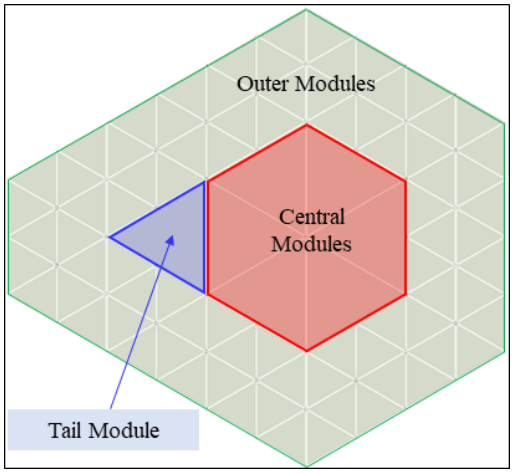

Fig. 4 Definition of module sections of floating island model

the effect of module size and arrangement on the motion performance of the floating island was examined. All numerical analyses made use of the assumption of deep water and head wave, which corresponds to the case where the incident wave propagates from the right to the left in Fig. 4.

4.1 Effect of Tail Module

The motion responses were compared between the original MARIN model and the newly proposed "Floater A" model in order to examine the effects of the tail module, as shown in Fig. 5. In the case of the Floater A model, the arrangement of the outer modules becomes symmetrical by removing the tail module. Focusing on the motion response of the modules on the weather side, a comparison was conducted between the 'HEAD' module at the outermost edge (square/rhombus symbol in Fig. 5) and the 'MID' module at the inside (circle/triangle symbol in Fig. 5). Fig. 6 compares the heave and pitch RAOs of the two outer modules between the MARIN model (solid line) and Floater A (dotted line). At $\omega = 0.2\,rad/s$, there is a slight difference in heave RAO due to the tail module, but overall, it can be seen that the effect of tail module on the motion RAOs of the outer modules is not significant. This indicates that the interaction effect is not strong owing to the large separation distance between the tail module and the front outer modules, and the effect of tail module on the overall motion response characteristics of the floating island is quite small. When comparing the motion response characteristics of the two outer modules at frequencies higher than 0.36 rad/s, the HEAD

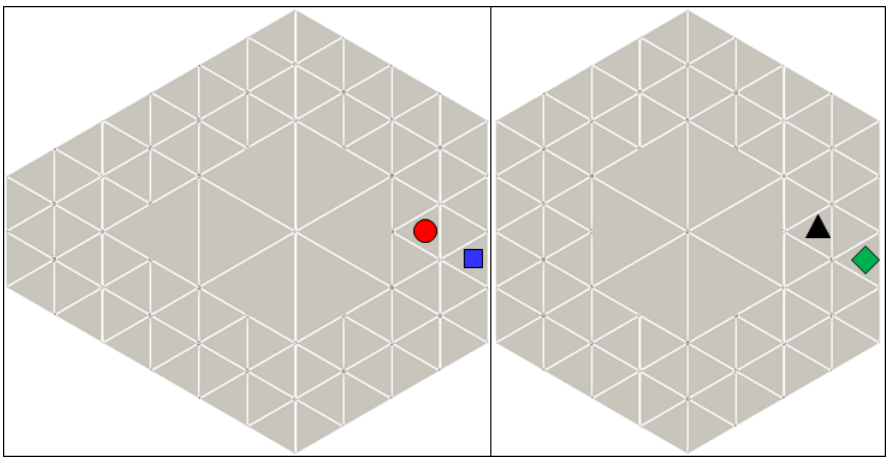

Fig. 5 Module arrangement of floating island models with and without tail module (left: MARIN model, right: Floater A)

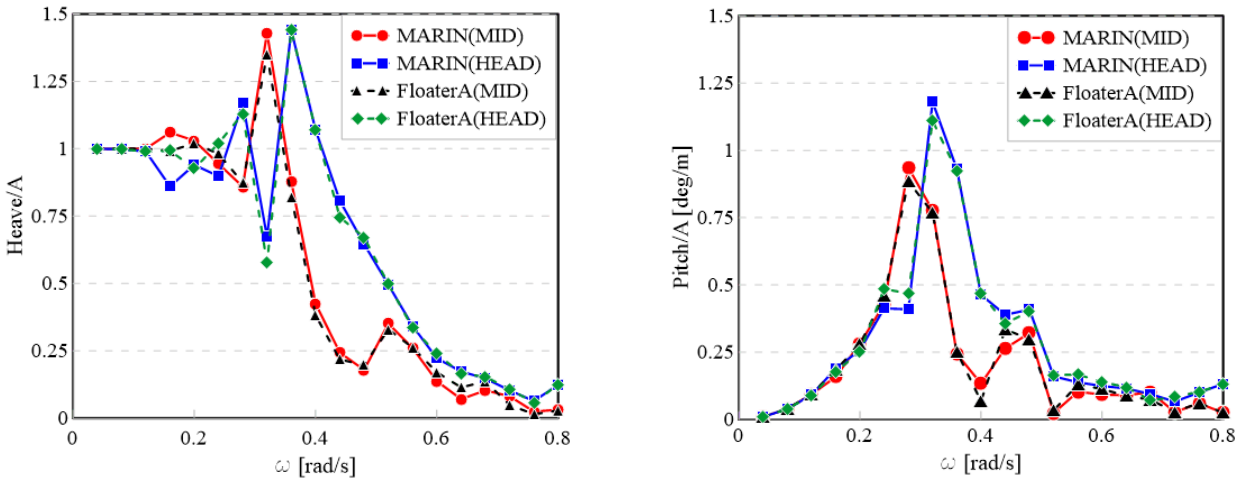

Fig. 6 Comparison of motion RAOs between floating island models with and without tail module: (a) Heave motion; (b) Pitch motion.

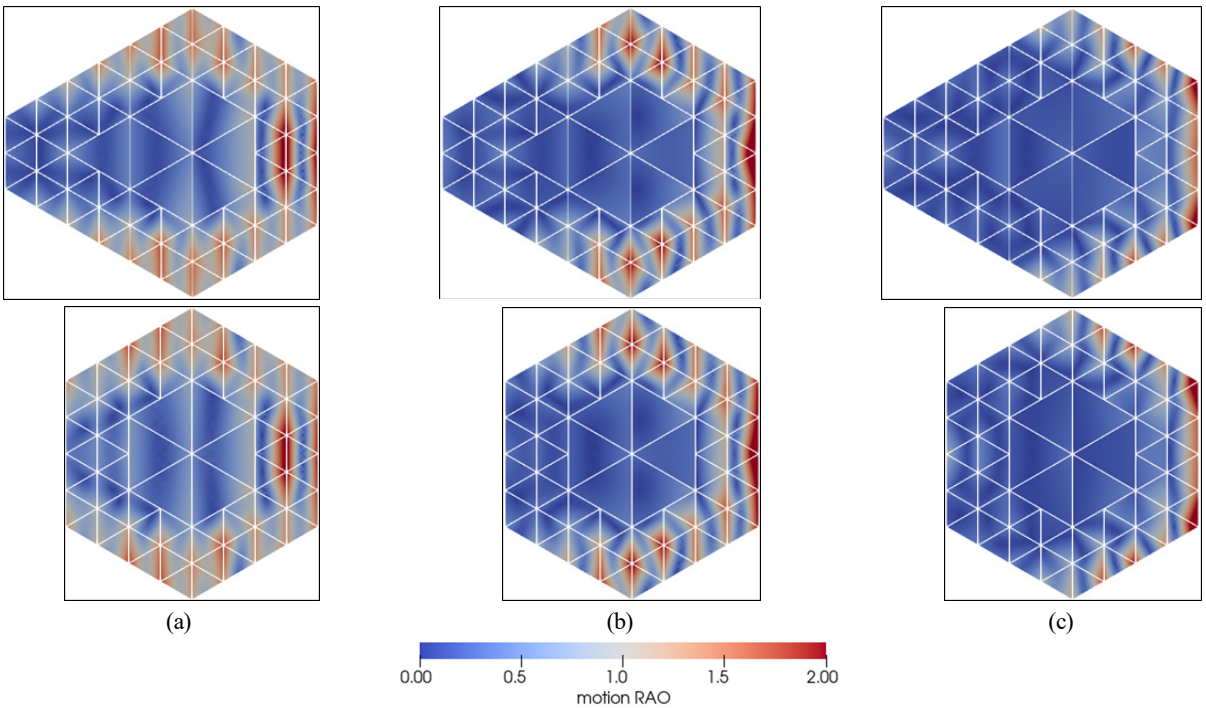

Fig. 7 Comparison of contour plots of vertical motion responses between floating island models with and without tail module: (a) ω = 0.32 rad/s; (b) ω = 0.36 rad/s; (c) ω = 0.4 rad/s

module consistently showed larger heave and pitch motions than the MID module. This means that when a high-frequency short wave is incident, only the outermost modules on the weather side are mainly excited, and the motions of the modules positioned farther within are reduced. In this case, most of the incident waves are reflected, creating high waves in front of the outer modules.

In the frequency range of 0.28 to 0.4 rad/s, the HEAD and MID modules exhibit large heave and pitch motion responses. The contour plots in Fig. 7 compares overall vertical motion response distribution of the two floating islands at three frequency conditions (ω= 0.32, 0.36, and 0.40 rad/s). First, both floating island models show that the vertical motion of the central modules is relatively less than that of the adjacent outer modules. This is because the outer modules move by absorbing the wave energy, and the wave exciting forces acting on the central module are significantly reduced. Another reason is that the central module has about 4 times inertia of the outer module. Another pattern in the contour plots is that the vertical motion increases intensively in the outer modules on the weather side (right side of the figure) under the short wave conditions and rapidly decreases on the opposite side. This is consistent with the numerical analysis results of Otto et al. (2019a), which show that at the peak frequency where the maximum motion of the modular floating island occurs, the modules on the lee side exhibit a very small motion, while the modules on the weather side experience a large motion. This feature indicates that the modules on the weather side absorb the majority of the wave kinetic energy under the short wave conditions, which leads to reduced motion responses of the other modules. When comparing the motion responses of two floating islands at the three frequencies, the MARIN model and Floater A show very similar patterns of vertical motion response distribution. This indicates that there is only a small effect of the tail module on the vertical motion of the floating island since it is placed in the opposite direction of the incident wave.

4.2 Effect of Central Modules

The advantage of a modular floating island is that the motion responses of the central modules and the lee-side modules are greatly reduced since the modules on the weather side absorb a large portion of the wave kinetic energy. Due to these characteristics, the central module exhibit a small motion response even if waves approach from various directions. The placement of large facilities like residential structures and essential equipment is therefore possible in the central modules of modular floating islands. In this section, a numerical analysis was conducted to examine the effect of the central module on the motion response of floating island. Fig. 8 illustrates the plan views of the “Floater A” and “Floater B” models depending on whether the

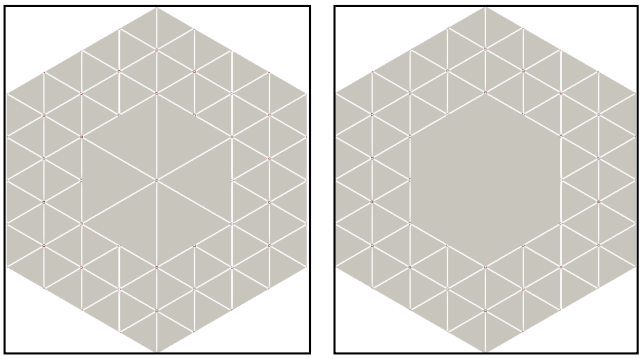

Fig. 8 Module arrangements of floating island model with different central modules (left: Floater A, right: Floater B)

central module of the floating island is divided. The central modules of "Floater A" are composed of six triangle modules, but the central module of "Floater B" is made up of one hexagon module.

Fig. 9 shows the comparison results of the heave and pitch RAOs for the central modules of Floaters A and B. In the case of Floater A, since the central part is made up of six modules, the motion response of the central modules was evaluated by the average of the motion responses of the triangle modules. The central module of Floater B shows smaller heave and pitch responses than that of Floater A in all frequency ranges. It can be seen that the motion performance of the single central module is better than that of divided central modules under all wavelength conditions. In Fig. 9(b), the central modules of Floater A have the maximum pitch response at a wave frequency of about 0.25 rad/s, in which the half of the incident wavelength (493 m) at this frequency is similar to the transverse length of the triangle modules ($\lambda/2L_{x,large} = 1.17$). Floater B shows the maximum pitch RAO at the wave frequency of 0.2 rad/s. Here, the length ratio between the transverse length of the central hexagon module and the half of the incident wavelength is approximately 0.9 ($\lambda/2L_{x,hexagon} = 0.9$). This indicates that the peak period of pitch motion can change depending on whether the central module is divided, and the pitch RAO of the central module has the maximum value under the condition that the wavelength of the incident wave corresponds to about twice the length of the central module. In this section, it was found that when using a single central module, not only heave and pitch motions are reduced, but also the peak frequency of pitch motion shifts to a lower frequency

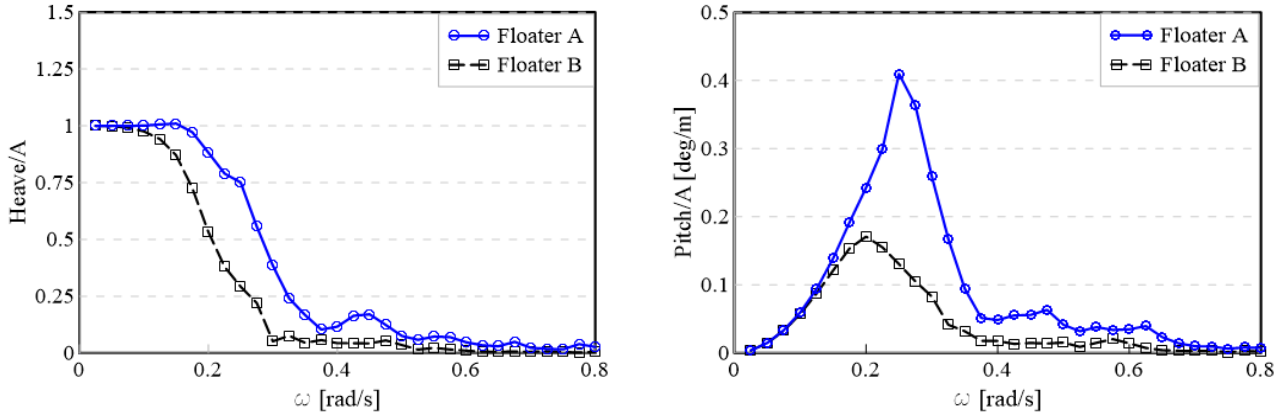

(a) (b)

Fig. 9 Comparison of motion RAOs central modules between the Floater A and B models: (a) Heave motion; (b) Pitch motion

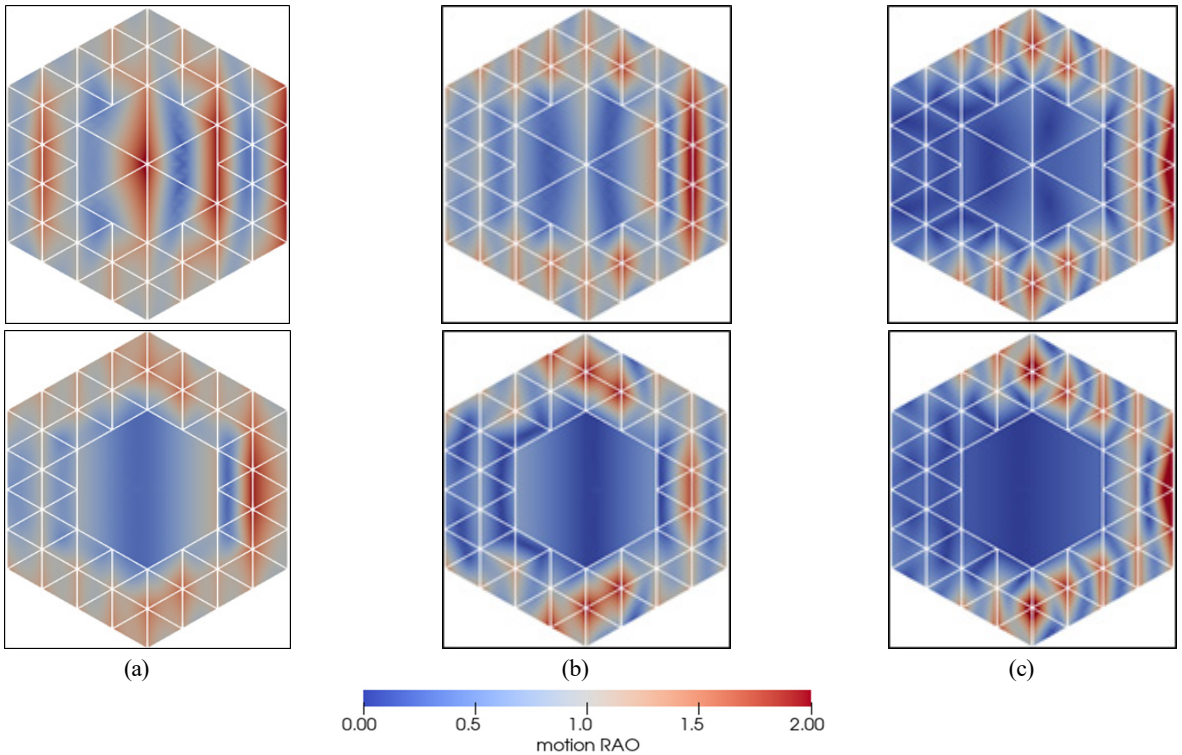

(a) (b) (c)

Fig. 10 Comparison of contour plots of vertical motion responses between floating island models with different central modules: (a) ω = 0.25 rad/s; (b) ω = 0.3 rad/s; (c) ω = 0.35 rad/s

than when using divided central modules. Therefore, a large single central module may be a good design alternative to reduce the wave-induced motion of modular floating island.

To check the effect of the central modules on the overall vertical motion of the floating island, the motion response of the entire floating island was visualized in the frequency range of $\omega = 0.2 - 0.3$ rad/s, where the central modules show a relatively large motion response. Fig. 10 shows contour graphs of the vertical plane motion amplitude distribution for the floating island for the three frequency conditions of $\omega = 0.25$, 0.30, and 0.35 rad/s. First, the central module of Floater B clearly shows a smaller vertical motion than the central modules of Floater A regardless of the wave frequencies. This means that the single central module reduces the local vertical motion responses compared to the divided central modules. Additionally, as discussed in the previous section, as the wave frequency increases, it can be also confirmed that vertical motion is concentrated on the outer module facing the incoming wave. On the other hand, it is remarkable that the vertical motion distribution characteristics of the outer modules differ significantly depending on whether or not the central modules are divided. This is because the vertical force of the connector between the central modules and the outer modules is affected by the motion performance of the central modules, and the mechanical interactions via these connectors significantly changes the motion characteristics of the outer modules. This effect is observed in the outer modules located on the front and side of the central modules.

4.3 Effect of Outer Modules

The outer module absorbs the wave kinetic energy and contributes to the motion reduction of the central module. Therefore, it is necessary to investigate the effect of the arrangement and configuration of the outer module layer on the motion reduction of the central module. In this section, 'Floater C' model was introduced by changing the size of the outer modules, and the effect of the number of outer module layers on

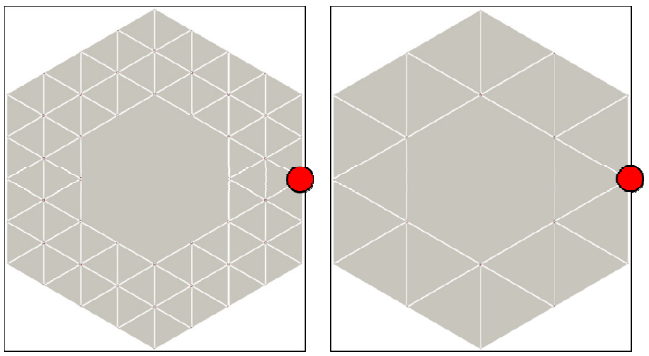

Fig. 11 Module arrangements with single-layer and double-layers outer modules (left: Floater B, right: Floater C)

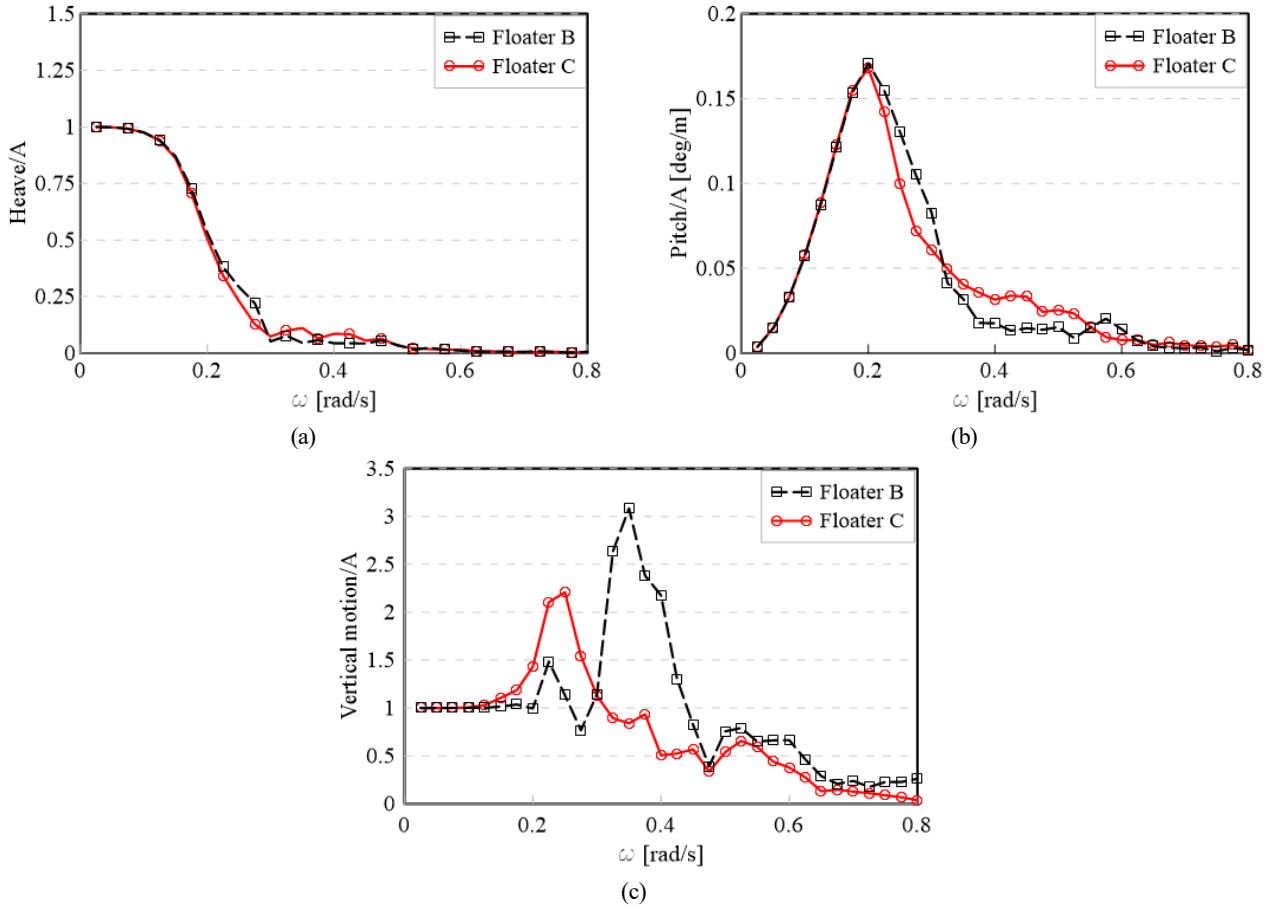

Fig. 12 Comparison of motion RAOs of central modules between floating island models with the single outer layer (Floater C) and double outer layer (Floater B): (a) Heave motion (central module); (b) Pitch motion (central module); (c) Vertical motion (outer module)

the motion response of the floating island was examined. Fig. 11 shows the plan view of the floating island models with single-layer (Floater C) and double-layers (Floater B) of outer modules.

Fig. 12 compares the heave and pitch RAOs between Floater B and Floater C. As shown in the figure, the effect of the outer layer on the central module was insignificant under the long waves in the frequency lower than 0.2 rad/s. However, Floater B and Floater C show a noticeable difference in the motion RAOs of the central module in the frequency higher than 0.2 rad/s. In particular, the motion RAOs of the central modules of both floating islands showed an opposite frequency dependence based on the wave frequency of 0.3 rad/s ($\lambda/L_{x,small}$ = 3.34). In other words, Floater C showed smaller heave and pitch response than Floater B at frequencies lower than 0.3 rad/s, whereas the opposite pattern was seen at frequencies higher than 0.3 rad/s. To examine the detailed motion characteristics, Fig. 12(c) compares the local vertical motion RAO of the outer modules of Floater B and Floater C. Since the motion response of the outer modules varies depending on the position of the module, the local vertical motion was examined for the outer end position of the outer modules (red dot position in Fig. 11), which exhibits a large vertical motion by directly facing the wave. The vertical motion response of the outer modules likewise altered at a frequency of 0.3 rad/s and shows the opposite tendency to the motion of the central modules. At frequencies below 0.3 rad/s and above 0.3 rad/s, the local vertical motion of the outer modules of Floaters B and C was smaller, respectively.

As mentioned above, the central and outer modules of Floater B and Floater C show different motion characteristics depending on the frequency. The motion responses of the floating island in irregular waves were assessed in order to compare the motion performance in real sea states. Based on the Pierson-Moskowitz (PM) spectrum, the significant wave height (H_s) of the irregular wave was set at 11.5 m, and the peak period (T_p) was changed to 14.5 s, 16.0 s, 17.5 s, and 19.0 s.

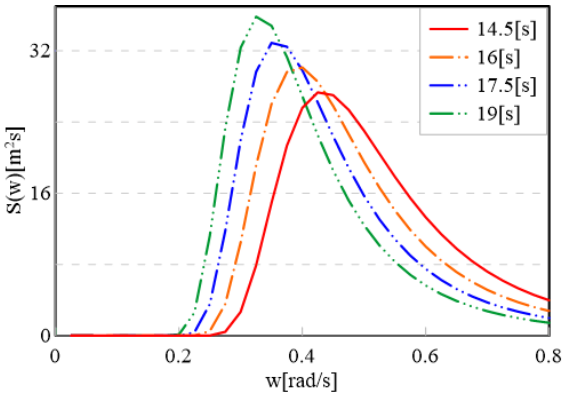

Fig. 13 Wave spectra for 4 irregular wave conditions

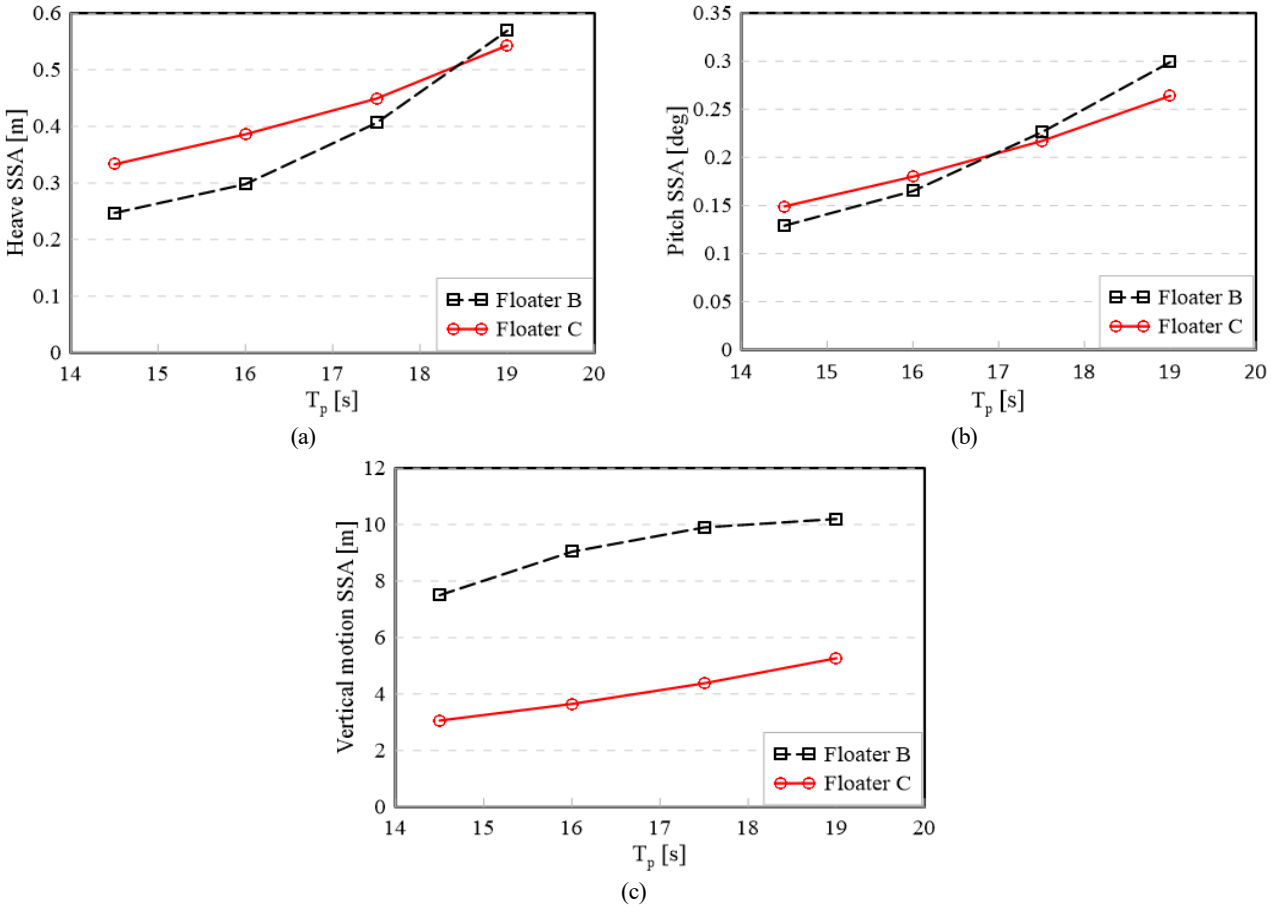

Fig. 14 Comparison of single significant response of heave and pitch motion of Floater B and C in irregular waves: (a) Heave motion (central module); (b) Pitch motion (central module); (c) Vertical motion (outer module)

This allowed for the consideration of a total of four irregular wave conditions. Fig. 13 shows the four irregular wave spectra considered in the motion performance evaluation of this study.

The motion responses of the floating island in irregular waves were calculated based on the frequency-domain spectral method by applying the following equations:

$$S_j(w) = \left|\overline{\eta_j}(w)\right|^2 S_\zeta(w) \tag{11}$$

$$\xi_j = 2\sqrt{\int S_j(w)dw} \tag{12}$$

where S_ζ and S_j are the response spectra of the wave spectrum and the jth motion mode of the floating island, respectively. Furthermore, $\overline{\eta_j}$ denotes the transfer function of the floating island's jth motion mode, and ξ_j denotes the single significant response for the jth motion mode.

The heave and pitch responses of central modules under four irregular wave conditions are compared in Fig. 14(a) and (b). A comparison of the local vertical motion response at the ends of the outer modules is shown in Fig. 14(c). In the case of the central modules, Floater B had a higher sensitivity of motion response according to the change of peak frequency than Floater C. The heave and pitch responses of Floater B increased by about 2.3 times and 2.32 times as the peak period of irregular wave changes from 14.5 s to 19.0 s, respectively. Under the same conditions, the heave and pitch responses of Floater C increased by about 1.63 and 1.77 times, respectively. As a result, the central modules of Floater B showed better motion performance in the sea states with a relatively short period. On the other hand, the motion response of the central modules of Floater C became smaller than that of Floater B under the peak period condition of 18.0 s or longer. This indicates that the double-layer outer part with small unit modules is more effective in calming the central modules than the single-layer outer part, except for the long period condition of 18.0 s or longer. In the case of the outer modules, it can be seen that the vertical motion of Floater C is around 2 to 2.5 times smaller than that of Floater B under the given irregular wave condition. This shows that Floater B, which employs small unit modules in the outer part, absorbs the wave kinetic energy better than Floater C, which employs large outer modules, and the outer modules of Floater B exhibit larger vertical motion responses.

5. Conclusions

The motion response of a modular floating island was numerically analyzed in this study. A potential flow-based numerical analysis method for the modular floating island was proposed. Numerical validation was performed by directly comparing the present calculation results with the model test data for the modular floating island by Waals et al. (2018). In this study, the modular floating island was divided into three parts; a tail module, central modules, and outer modules. The vertical motion responses was examined according to the module size and arrangement by a series of numerical studies. First, the effect of the tail module on the vertical motion was insignificant, whereas the change in the motion response of the floating island was clearly observed depending on the division effect of the central module. It was confirmed that the vertical motion of the central module was reduced and the peak period shifted to a lower frequency range when a single central module was used than divided small central modules. Next, depending to the size of the outer modules and the number of outer layers, the change in heave and pitch of the central modules was negligible in the low frequency region, but significant in the high frequency region. In particular, through irregular wave analysis, the double-layer outer part with small unit modules is more effective in calming the central modules than the single-layer outer part with large unit modules, except under very long period conditions. It was observed that the wave kinetic energy is better absorbed when a small unit module is employed on the outer part. Future research must look more closely at the motion characteristics of the floating island with moorings in the horizontal plane, and the optimization of the unit module shape and connector for the modular artificial floating island.

Conflict of Interest

No potential conflict of interest relevant to this article was reported.

Funding

This study was carried out with the support of the "Development of core source technology for marine green hydrogen for the realization of a carbon-neutral society" project of the Korea Research Institute of Ships & Ocean Engineering affiliated with the Korea Institute of Ocean Science and Technology and the "Development of prediction technology for local wave fields around offshore structures" project of the Research Institute of Marine Systems Engineering of Seoul National University. We would like to express our sincere appreciation for this financial support of our research.

References

Yeh, N., Yeh, P., & Chang, Y. -H. (2015). Aritificial floating islands for environmental improvement. *Renewable and Sustainable Energy Reveic, 47*, 616–622. https://doi.org/10.1016/j.rser.2015.03.090

Lu, H. -L., Ku, C. -R., & Chang, Y. -H. (2015). Water quality improvement with artificial floating islands. *Ecological Engineering, 74*, 371–375. https://doi.org/10.1016/j.ecoleng.2014.11.013

Wang, C. M. & Tay, Z. Y. (2011). Very large floating structures: applications, research and development. *Procedia Engineering, 14*, 62–72. https://doi.org/10.1016/j.proeng.2011.07.007

Lamas-Pardo, M., Iglesias, G., & Carral, L. (2015). A review of very

large floating structures (VLFS) for coastal and offshore uses. *Ocean Engineering, 109*, 677−690. https://doi.org/10.1016/j.oceaneng.2015.09.012

Kashiwagi, M. (1998). A B-spline Galerkin scheme for calculating the hydroelastic response of a very large floating structure in waves. *Journal of Marine Science and Technology, 3*, 37−49. https://doi.org/10.1007/BF01239805

Watanabe, E., Utsunomiya, T., & Wang, C.M. (2004). Hydroelastic analysis of pontoon-type VLFS: a literature survey. *Engineering Structures, 26*(2), 245−256. https://doi.org/10.1016/j.engstruct.2003.10.001

Wu, Y., Wang, D., Riggs, H. R., & Ertekin, R. C. (1993). Composite singularity distribution method with application to hydroelasticity. *Marine Structures, 6*(2-3), 143−163. https://doi.org/10.1016/0951-8339(93)90017-W

Riggs, H. R., Ertekin, R. C., & Mills, T. R. J. (2000). A comparative study of RMFC and FEA models for the wave-induced response of a MOB. *Marine structures, 13*(4-5), 217−232. https://doi.org/10.1016/S0951-8339(00)00029-0

Fu, S., Moan, T., Chen, X., & Cui, W. (2007). Hydroelastic analysis of flexible floating interconnected structures. *Ocean engineering, 34*(11-12), 1516−1531. https://doi.org/10.1016/j.oceaneng.2007.01.003

Kim, J. -G., Cho, S. -P., Kim, K. T., & Lee, P. -S. (2014). Hydroelastic design contour for the preliminary design of very large floating structures. *Ocean Engineering, 78*, 112−123. https://doi.org/10.1016/j.oceaneng.2013.11.006

Gao, R. P., Tay, Z. Y., Wang, C. M. & Koh, C. G. (2011). Hydroelastic response of very large floating structure with a flexible line connection. *Ocean Engineering, 38*, 1957−1966. https://doi.org/10.1016/j.oceaneng.2011.09.021

Nam, B. W., & Hong, S. Y. (2021). Eigenvalue analysis for motion response of a TLP and tender semi considering a complex mooring configuration. *International Journal of Offshore and Polar Engineering, 31*(2),169−177. https://doi.org/10.17736/ijope.2021.mm26

Zhang, H., Xu, D., Xia, S., Qi, E., Tian, C., & Wu, Y. (2015). Nonlinear network dynamic characteristics of mulit-module floating airport with flexible connectors. *Proceedings of the Twenty-fifth International Ocean and Polar Engineering Conference*, Kona, Hawaii, USA, 1583−1590.

Otto, W. J., Waals, O. J., Bunnik, T., & Ceneray, C. (2019a). Wave induced motions of a floating mega island. In: Wang, C., Lim, S., & Tay, Z. (Eds.), *WCFS2019, Lecture notes in civil engineering: Vol. 41.* (pp. 173−189). Springer. https://doi.org/10.1007/978-981-13-8743-2_9

Otto, W. J., Waals, O. J., Bunnik, T. H. J., & Cresp, J. (2019b). Optimization of wave induced motions and forces on a floating island. *Proceedings of the Twenty-ninth International Ocean and Polar Engineering Conference*, Honolulu, Hawaii, USA, 3120−3126.

Waals, O.J ., Bunnik, T. H .J., & Otto, W. J. (2018). Model tests and numerical analysis for a floating mega island. *Proceedings of the 37th International Conference on Ocean. Offshore and Arctic Engineering*, Madrid, Spain. V001T01A016. https://doi.org/10.1115/OMAE2018-78589

Zalar, M., Diebold, L., Baudin, E., Henry, J., & Chen, X. -B. (2007). Sloshing effects accounting for dynamic coupling between vessel and tank liquid Motion. *Proceedings of the 26th International Conference on Offshore Mechanics and Arctic Engineering*, San Diego, USA, 687−701. https://doi.org/10.1115/OMAE2007-29544

Wu, Y., Wang, D., Riggs, H. R., & Ertekin, R. C. (1993). Composite singularity distribution method with application to hydroelasticity. *Marine Structures, 6*(2-3), 143−163. https://doi.org/10.1016/0951-8339(93)90017-W

Choi, Y. R., & Hong, S. Y. (2002). An analysis of hydrodynamic interaction of floating multi-body using higher-order boundary element method. P*roceedings of the Twelfth International Offshore and Polar Engineering Conference.* Kitakyushu, Japan, 303−308.

Author ORCIDs

Author name	ORCID
Park, Hyo-Jin	0000-0002-6491-6400
Kim, Jeong-Seok	0000-0002-0416-4403
Nam, Bo Woo	0000-0003-1125-7453

KSOE

Journal of Ocean Engineering and Technology 37(1), 20-30 February, 2023
https://doi.org/10.26748/KSOE.2022.034

pISSN 1225-0767
eISSN 2287-6715

Original Research Article

A Study on the High-Order Spectral Model Capability to Simulate a Fully Developed Nonlinear Sea States

Young Jun Kim[1], Hyung Min Baek[2], Young Jun Yang[3], Eun Soo Kim[1,4] and Young-Myung Choi[1,4]

[1]*Researcher, Global Core Research Center for Ships and Offshore Plants, Pusan National University, Busan, Korea*
[2]*Ph. D. candidate, Dept. Naval Architecture and Ocean Engineering, Pusan National University, Busan, Korea*
[3]*Professor, Dept. Naval Architecture and Ocean Engineering, Tongmyong University, Busan, Korea*
[4]*Professor, Dept. Naval Architecture and Ocean Engineering, Pusan National University, Busan, Korea*

KEYWORDS: High-order spectral method, Wave realization, Probability of Exceedance, Nonlinear wave, Wave spectrum

ABSTRACT: *Modeling a nonlinear ocean wave is one of the primary concerns in ocean engineering and naval architecture to perform an accurate numerical study of wave-structure interactions. The high-order spectral (HOS) method, which can simulate nonlinear waves accurately and efficiently, was investigated to see its capability for nonlinear wave generation. An open-source (distributed under the terms of GPLv3) project named "HOS-ocean" was used in the present study. A parametric study on the "HOS-ocean" was performed with three-hour simulations of long-crested ocean waves. The considered sea conditions ranged from sea state 3 to sea state 7. One hundred simulations with fixed computational parameters but different random seeds were conducted to obtain representative results. The influences of HOS computational parameters were investigated using spectral analysis and the distribution of wave crests. The probability distributions of the wave crest were compared with the Rayleigh (first-order), Forristall (second-order), and Huang (empirical formula) distributions. The results verified that the HOS method could simulate the nonlinearity of ocean waves. A set of HOS computational parameters was suggested for the long-crested irregular wave simulation in sea states 3 to 7.*

1. Introduction

The performance analysis of an offshore structure operating in the ocean is commonly requested to verify its survivability and operability over its expected design life. The most common way is to conduct an experimental campaign on the offshore platform in the wave basin. On the other hand, it is limited because of the scale effect, difficulty of measurement and modeling, cost, and the limitation of the experimental facility. Numerical analysis can be an alternative to an experiment because it can compensate for the experimental limitations. Nevertheless, it suffers from computational mesh modeling, numerical convergence, and a choice of numerical methods to simplify physical phenomena.

In both experiments and numerical simulations, the quality of ocean waves is the critical factor in modeling a realistic sea state. Therefore, the generated irregular waves experimentally and numerically should be qualified with the target sea state. In those applications, the irregular waves were qualified by comparing the sea spectrum, the significant wave height, and the peak wave period with the target sea state. On the other hand, considering the design of offshore structure dealing with extreme events, such as wave impact, air gap impact, and green water phenomena, the qualification of a local wave elevation, e.g., wave crest, becomes important and prevail nowadays. The measured wave elevation gives a wave crest probability distribution of single realization (PDSR). The PDSR is a probability distribution of the wave crest from one wave realization of a three-hour typical storm duration. The wave time signal in the experiment and numerical simulation with the limited number of irregular waves and different random seeds gives different wave crest PDSR curves. Hence, the PDSR curve made from a random seed can differ. Therefore, it is difficult to confirm the quality of the wave crest PDSR. Numerous wave realizations can be used to obtain the wave crest probability distribution of ensemble realization (PDER), which is a probability distribution of the wave crest from many three-hour realizations.

The obtained distribution of wave crest can be compared with the reference distributions. Longuet-Higgns (1952) reported the wave

Received 5 October 2022, revised 13 December 2022, accepted 13 February 2023
Corresponding author Young-Myung Choi: +82-51-510-2346, youngmyung.choi@pusan.ac.kr

crest distribution of linear waves follows the Rayleigh distribution with assumptions of the Gaussian distribution and the narrow-band spectrum. On the other hand, the Rayleigh distribution underestimates the height of the wave crest when the sea states become severe, which can lead to a wrong design. Forristall (2000) suggested the wave crest distribution based on the second-order theory, which gives better results than the Rayleigh distribution. Later, Huang and Zhang (2018) suggested the semi-empirical formula of PDSR (mean and 99% upper bound and 99% lower bound) and PDER from the numerical wave simulation results of 305 sea states. The idea of Huang and Zhang (2018) was to qualify the PDSR with a single wave realization by comparing the distribution of wave crest probability of occurrence (POE) in the range of bounds of wave crest PDER. They compared the PDER between 100 realizations and 1000 realizations: the wave crest PDER showed a difference of −3% to +4% at the POE level of 10^{-4} and a −6% to +7% difference at the POE level of 10^{-5}.

The irregular waves based on the superposition of linear waves are insufficient to model realistic ocean waves. Goda (1983) reported that the secondary peak due to the interaction of waves and nonlinearities is significant in ocean waves. Therefore, considering the nonlinearity is vital for the qualified local wave elevation. Tick (1963) and Hamada (1965) suggested the second-order irregular wave models. They reported that the second-order effect might not be enough to describe a higher-order interaction between wave components. The high-order spectral (HOS) method is a nonlinear wave generation method extending up to an arbitrary order (West et al., 1987; Dommermuth and Yue, 1987). One of the main strengths of HOS is that the derivatives that appear in nonlinear free surface boundary conditions can be treated in the frequency domain. Therefore, the fast Fourier transform (FFT) can be used in the numerical simulation, which makes the HOS method more efficient than the other numerical methods. The open-source project, called HOS-ocean, which models the open ocean by the HOS method, has been published (Ducrozet et al., 2007; Bonnefoy et al., 2009; Ducrozet et al., 2016). Moreover, they apply the HOS method for the numerical wave tank, which is also published as HOS-NWT (Ducrozet et al., 2012). The nonlinear irregular waves generated from the HOS method have been used to simulate the nonlinear waves in computational fluid dynamics (CFD) (Choi et al., 2018; Lu et al., 2022). Furthermore, those numerical tools have been used to simulate the wave-structure interaction problem (Li et al., 2019; Choi, 2019; Xiao et al., 2019). In addition, there was an attempt to define the standard protocol for irregular wave generation because it is used widely in industry and academia (Bouscasse et al., 2021).

Most academic research on applying the HOS model and CFD is limited to the extreme sea state. A parametric study of the HOS model for a wide range of sea conditions has not been conducted. In this context, this reports the results of a parametric study on the HOS method. As a parametric study, one hundred long-crested irregular wave simulations with different random seeds were performed for each sea state and selected HOS parameters for three hours. The present paper performed a stochastic analysis and analyzed the wave spectrum and wave crest height distribution by comparing them with references.

2. Numerical Wave Model

2.1 High Order Spectral Method

The open ocean is modeled with the rectangular computational domain with a length L in the x direction and a depth h in z direction. The sea bottom was assumed to be flat. The mean free surface was located at $z=0$, and the z-axis was orienting upward. The perfect fluid and irrotational flow were assumed to introduce the velocity potential Φ. The velocity potential satisfied the Laplace's equation in the fluid domain D as given in Eq. (1). The impermissible condition given in Eq. (2) was imposed on the sea bottom at $z=-h$. The periodic boundary condition shown in Eq. (3) is imposed at the lateral boundary.

$$\nabla^2\Phi(x,z,t)=0 \quad in \;\; D \tag{1}$$

$$\frac{\partial\Phi}{\partial z}=0 \quad at \;\; z=-h \tag{2}$$

$$\Phi(x=0,z,t)=\Phi(x=L,z,t)\;, \quad \eta(x=0,t)=\eta(x=L,t) \tag{3}$$

On the free surface $z=\eta(x,t)$, two free surface boundary conditions were imposed. The dynamic and kinematic free surface boundary conditions are given in Eqs. (4) and (5), respectively.

$$\frac{\partial\tilde{\Phi}}{\partial t}+g\eta=-\frac{1}{2}\nabla\tilde{\Phi}\cdot\tilde{\Phi}+\frac{1}{2}(1+\nabla\eta\cdot\nabla\eta)w^2 \tag{4}$$

$$\frac{\partial\eta}{\partial t}=(1+\nabla\eta\cdot\nabla\eta)w-\nabla\tilde{\Phi}\cdot\nabla\eta \tag{5}$$

$\tilde{\Phi}(x;t)=\Phi(x,z=\eta(x);t)$ is the free surface velocity potential, and $w(x)=\partial\Phi/\partial z$ is the vertical velocity at the free surface $z=\eta(x,t)$. The periodic boundary condition enables the free surface velocity potential and wave elevations with modal functions to be expressed as Eqs. (6) and (7).

$$\tilde{\Phi}(x,t)=\sum_{n=0}^{N_x}\widetilde{A_n}(t)\cos(k_n x) \tag{6}$$

$$\eta(x,t)=\sum_{n=0}^{N_x}B_n(t)\cos(k_n x) \tag{7}$$

$\widetilde{A_n}(t)$ and $B_n(t)$ are modal amplitudes of free surface potential and wave elevations, respectively. N_x is the number of modes. $k_n=n\pi/L$ is a pseudo wavenumber adjusted to the domain length. The velocity potential defined in the fluid domain and the vertical fluid velocity are expressed with the perturbation series as follows:

$$\Phi(x,z,t)=\sum_{m=1}^{M}\Phi^{(m)}(x,z,t) \tag{8}$$

$$w(x,z,t)=\sum_{m=1}^{M}w^{(m)}(x,z,t) \tag{9}$$

with

$$\Phi^{(m)}(x,z,t)=\sum_{n=0}^{N_z}A_n^{(m)}(t)\frac{\cosh k_n(z+h)}{\cosh k_n h}\cos(k_n x) \tag{10}$$

where the superscript $q^{(m)}$ represents a quantity of $O(\epsilon^m)$, M is the nonlinear order of the HOS method, where $A_n^{(m)}(t)$ is the modal amplitude of velocity potential of corresponding order, and the vertical fluid velocity can be given in $w^{(m)}=\Phi_z^{(m)}$, respectively. The free surface potential and the vertical fluid velocity on the $z=\eta$ were evaluated by applying the Taylor series expansion as given in Eqs. (4) and (5), respectively.

$$\tilde{\Phi}(x,t)=\Phi(x,z=\eta,t)=\sum_{m=1}^{M}\sum_{k=0}^{M-m}\frac{\eta^k}{k!}\frac{\partial^k\Phi^{(m)}(x,z=0,t)}{\partial z^k} \tag{11}$$

$$w(x,z=\eta,t)=\sum_{m=1}^{M}\sum_{k=0}^{M-m}\frac{\eta^k}{k!}\frac{\partial^{k+1}\Phi^{(m)}(x,z=0,t)}{\partial z^{k+1}} \tag{12}$$

The triangular system, which can be solved explicitly, can be obtained by expanding with respect to the order. The initialization of wave fields for the simulation is taken from the spectrum of irregular waves. The modal amplitudes of the wave elevation and free surface potential are taken as

$$B_n(t=0)=\sqrt{2S(\omega)\Delta k_n}\quad\text{and}\quad\widetilde{A}_n(t=0)=-\frac{i\omega_n}{g}B_n(t=0) \tag{13}$$

where $\omega_n^2=gk_n\tanh k_n h$. After setting the linear wave fields in the HOS simulation domain, the nonlinearity evolves with the simulation time because the nonlinear free surface boundary conditions in Eqs. (4) and (5) make wave interactions. West et al. (1987) and Ducrozet et al. (2007) explained the detailed formulation of the HOS method.

3. Numerical Set-Up

3.1 Wave Condition

The wave conditions used in this study were taken from the sea state code suggested by World Meteorological Organization (WMO) (Lee and Bales, 1984; Lewis, 1989) to use representative wave conditions. Table 1 lists the wave conditions for each sea state code. In the present study, five wave conditions from sea state 3 to sea state 7, colored in Table 1, were considered, and the selected range corresponds to 90% of the annual sea state occurrence.

A modified two-parameter Pierson-Moskowitz (P-M) spectrum is applied to describe the wave spectrum in a frequency domain (Kim, 2008) as expressed in Eq. (11). Here, $\omega_p=2\pi/T_p$ is the peak angular frequency, and H_s is the significant wave height of each sea state. Fig. 1 presents the considered wave spectra for different sea states.

$$S(\omega)=\frac{5}{16}H_s^2\omega_p^4\omega^{-5}\exp\left[-\frac{5}{4}\left(\frac{\omega}{\omega_p}\right)^{-4}\right] \tag{14}$$

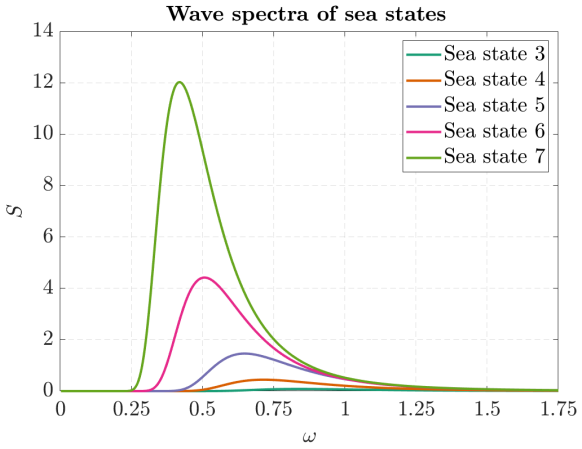

Fig. 1 Wave spectra for different sea states

3.2 HOS Computational Setup and Computational Parameters

The HOS fluid domain had a dimension of $L_x=15\lambda_p$ in the horizontal direction, and the deep water condition was assumed. Two

Table 1 Annual sea state occurrences and wave parameters with respect to the sea states

Sea state	Mean significant wave height (m)	Most probable peak period (s)	Most probable peak wavelength (m)	Steepness (%)	Occurrence probability (%)
0–1	0.05	-	-	-	0.70
2	0.3	7.5	87.82	0.34	6.80
3	0.88	7.5	87.82	1.00	23.70
4	1.88	8.8	120.90	1.55	27.80
5	3.25	9.7	146.90	2.21	20.64
6	5.0	12.4	240.07	2.08	13.15
7	7.5	15.0	351.29	2.13	6.05
8	11.5	16.4	419.93	2.74	1.11
>8	>14	20	624.52	>2.24	0.02

Table 2 Considered HOS orders and the number of HOS modes

Order	HOS modes		
	$N_x = 128$	$N_x = 256$	$N_x = 512$
$M=1$	○	○	○
$M=2$	○	○	○
$M=3$	○	○	○
$M=4$	○	○	○

computational parameters in the HOS method are important. The first was the order of nonlinearity, e.g., HOS order (M), and the second was the number of HOS modes (N_x) corresponding to the number of spatial discretizations. Four HOS orders and three levels of HOS modes were adopted, as summarized in Table 2. Each HOS simulation was conducted for the three-hours, and 100 simulations with different random seeds were performed for each simulation setup. The HOS waves were measured at $L_x = 5\lambda_p$. For example, Fig. 2 shows a HOS wave time series of sea state 7 with the HOS order $M=4$ and the HOS modes $N_x = 512$.

4. Results and Discussions

4.1 Spectral Analysis

The wave spectrum was obtained from the wave elevation time series using Welch's overlapped segment averaging estimator (Welch, 1967), where the window interval was approximately $15\,T_p$. The averaged wave spectrum can be taken from 100 wave spectra and compared with the target wave spectrum. Fig. 3 gives an example of normalized wave spectra of sea state 7. The solid black line is a reference wave spectrum, and each colored marked lines are the wave spectrum with different combinations of HOS parameters. The wave spectra with HOS modes $N_x = 128$ clearly showed an overestimated spectrum compared to the target spectrum. While with other computational setups, the difference between each setup was minimal, and the difference between each spectrum quantitatively is challenging.

The difference ratio of each wave spectrum is compared. Fig. 4 illustrates the difference ratio of the wave spectrum with respect to the angular frequency. The tolerance criterion of the wave spectral analysis is ±5% within the frequency range $f \in [0.75f_p; 1.5f_p]$, where f_p is the peak frequency of the target sea state. Note that this spectral qualification criterion was adopted from previous studies (Canard et al., 2020; Canard et al., 2022). The red-colored region presents the target tolerance zone. First, the wave spectra obtained with $N_x = 128$ were overestimated compared with the target spectra for all sea states regardless of the HOS order. For all combinations of the HOS parameters except for the HOS modes $N_x = 128$, the difference ratio of wave spectrum lie in the ±5% tolerance within the target frequency range. A comparison of the difference ratio with respect to the HOS order revealed a relatively large variation as the HOS order increases.

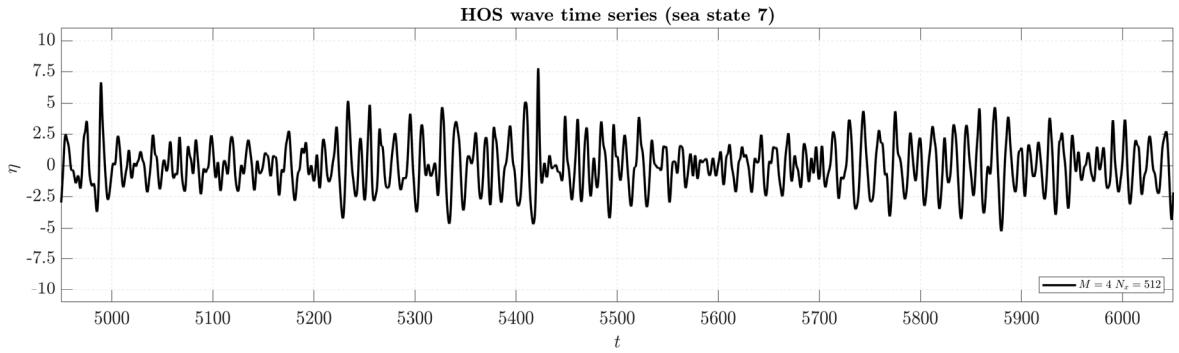

Fig. 2 Example of the HOS wave time series ($N_x = 512$, $M=4$)

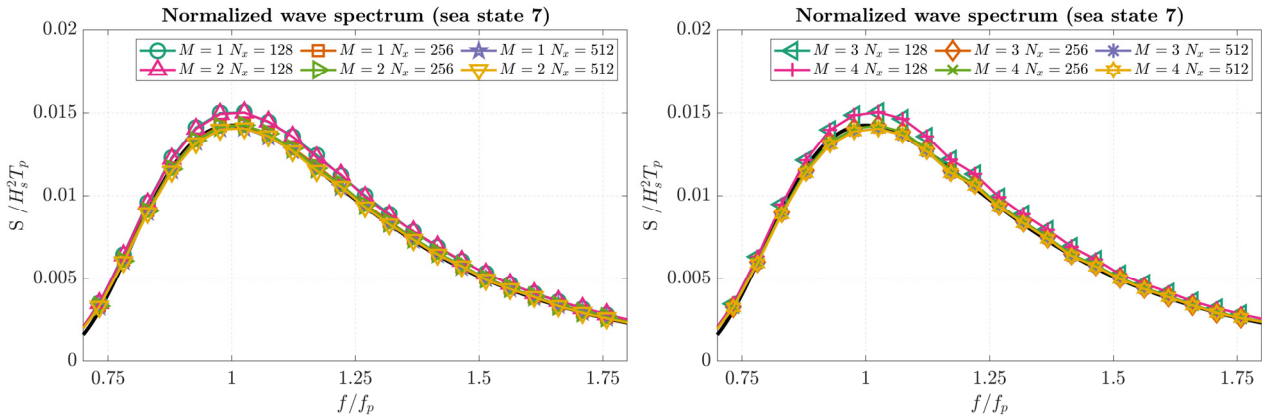

Fig. 3 Normalized wave spectra of sea state 7 with different combinations of HOS parameters

A quantitative comparison of the wave spectrum for each HOS computational parameter was conducted. The maximum difference ratio and the average absolute difference ratio of the wave spectrum in the target frequency range were evaluated using Eqs. (15) and (16), and the values are presented in Table 3.

$$\text{Maximum difference} = \max\left(\frac{S(f)-S_{Target}(f)}{S_{Target}(f)}\right), \quad f \in [0.75f_p; 1.5f_p] \tag{15}$$

$$\text{Average absolute difference} = mean\left(\left|\frac{S(f)-S_{Target}(f)}{S_{Target}(f)}\right|\right), \quad f \in [0.75f_p; 1.5f_p] \tag{16}$$

Table 3 lists the computational setup where their maximum and averaged absolute difference ratio is larger than 10% is colored red, larger than 5% is colored yellow, and less than 5% is colored green. As shown in Fig. 4, all results with HOS modes $N_x = 128$ have maximum and average absolute difference ratios larger than 5%. The difference ratio decreased as the number of modes increased. In addition, the difference ratio tends to increase as the HOS order increases, but the increment is relatively small.

For all sea states, the smallest average absolute difference ratio was measured with the computational setup of HOS modes $N_x = 512$ and HOS orders $M = 1$. The largest maximum difference ratio with HOS modes $N_x = 256$ was 4.00% (sea state 4, $N_x = 256$, $M = 4$), and the largest maximum difference ratio with HOS modes $N_x = 512$was 3.82% (sea state 5, $N_x = 512$, $M = 3$). The largest average absolute difference ratio with HOS modes $N_x = 256$ was 1.58% (sea state 5, $N_x = 256$, $M = 3$), and the largest average absolute difference ratio with HOS modes $N_x = 512$ was 1.58% (sea state 5, $N_x = 512$, $M = 3$). The average absolute difference ratio with HOS modes $N_x = 256$ and $N_x = 512$ was suppressed by under 2%. In addition, approximately 1% of the average absolute difference ratio is measured with HOS mode $N_x = 512$ and HOS order $M = 2$. Therefore from the spectral analysis, the HOS modes $N_x = 512$ is recommended for the HOS wave generation.

4.2 Wave Crest Probability Distribution Analysis

As discussed in the Introduction, both the PDSR and the PDER of the HOS waves were compared with the Rayleigh (first-order), the Forristall (second-order), and the Huang (semi-empirical formula) distributions. Eqs. (17)–(19) describe the mathematical formula of the Rayleigh, the Forristall, and the Huang distributions, respectively. Each distribution describes the POE of the measured wave crest from the mean free surface (η_c). In Eq. (20), U_r is the Ursell number, S_1 is

Table 3 Maximum and averaged difference of wave spectrum with respect to sea states and HOS parameters

	Sea state 3						Sea state 4					
	Maximum difference (%)			Average absolute difference (%)			Maximum difference (%)			Average absolute difference (%)		
Order (M) \ Mode (N_x)	128	256	512	128	256	512	128	256	512	128	256	512
1	8.26	2.69	1.38	6.80	1.32	0.70	8.30	2.87	1.54	6.75	1.31	0.69
2	8.09	2.51	1.48	6.74	1.29	0.72	8.41	2.86	1.62	6.67	1.28	0.78
3	8.07	2.81	1.66	6.75	1.31	0.81	9.42	3.99	2.62	6.57	1.36	1.11
4	8.11	2.81	1.66	6.73	1.31	0.81	8.78	4.00	2.06	6.58	1.36	1.09

	Sea state 5						Sea state 6					
	Maximum difference (%)			Average absolute difference (%)			Maximum difference (%)			Average absolute difference (%)		
Order (M) \ Mode (N_x)	128	256	512	128	256	512	128	256	512	128	256	512
1	8.47	3.15	1.82	6.83	1.37	0.74	7.52	2.03	1.44	6.56	1.14	0.60
2	9.65	3.70	2.23	6.63	1.24	0.97	8.43	3.27	1.84	6.48	1.31	1.04
3	10.11	3.07	3.82	6.44	1.58	1.58	9.44	3.11	2.60	6.37	1.42	1.36
4	9.94	3.06	2.87	6.44	1.57	1.35	9.44	3.13	2.58	6.37	1.41	1.36

	Sea state 7					
	Maximum difference (%)			Average absolute difference (%)		
Order (M) \ Mode (N_x)	128	256	512	128	256	512
1	8.01	2.49	1.40	6.73	1.29	0.74
2	8.19	3.34	2.06	6.51	1.23	0.86
3	9.24	3.15	2.60	6.47	1.42	1.31
4	9.25	3.16	2.57	6.48	1.42	1.32

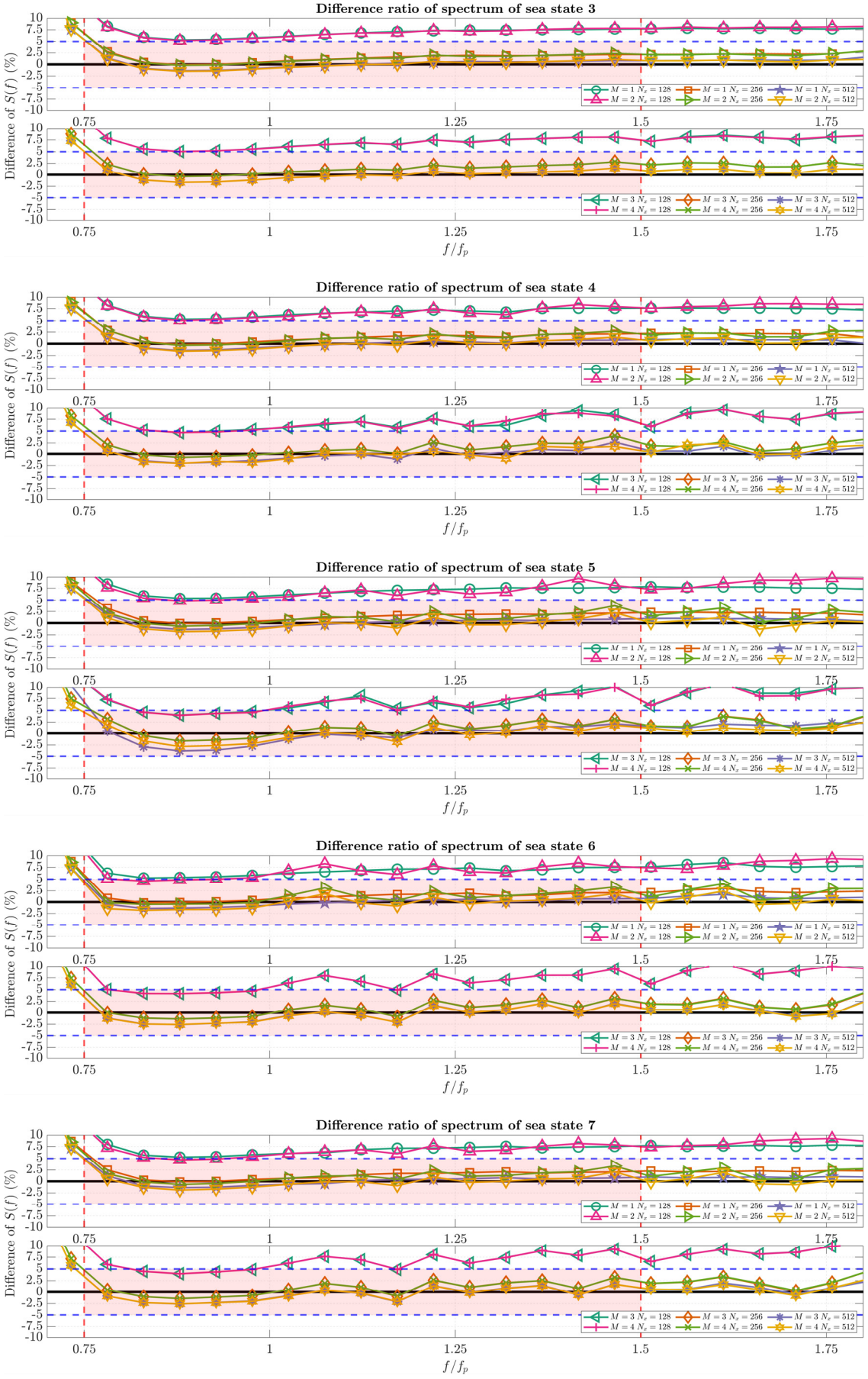

Fig. 4 Difference ratio between the measured wave spectrum and the target wave spectrum. The red zone is the target tolerance zone.

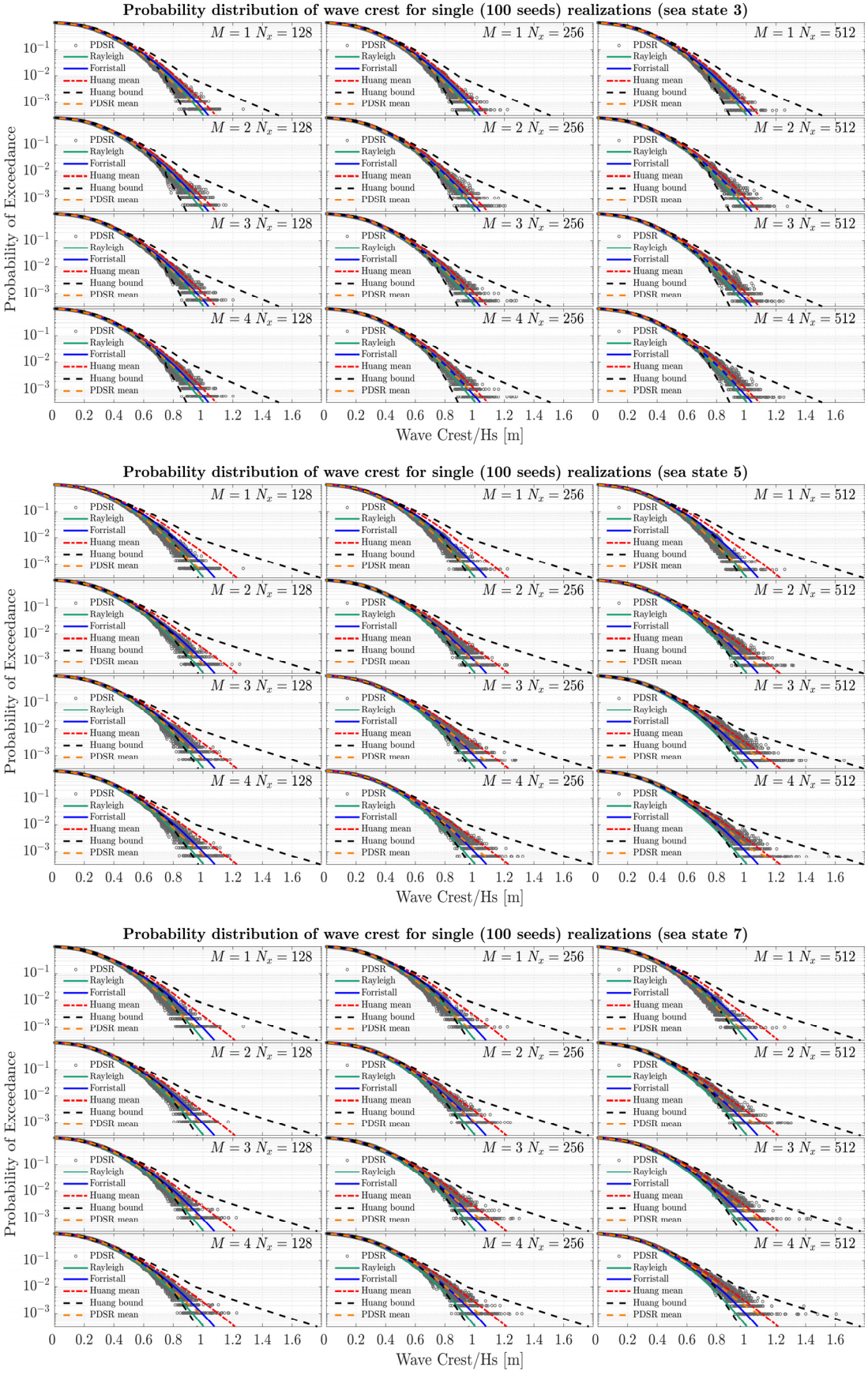

Fig. 5 PDSR and mean PDSR of 100 realizations made with different combinations of HOS parameters for sea states 3, 5, and 7. These were compared with the Rayleigh (first-order), the Forristall (second-order), and the Huang (semi-empirical formula) distributions.

Table 4 Coefficients for Huang semi-empirical PDSR and PDER formula

	POE > 10^{-2}				POE < 10^{-2}			
	PDSR Mean	Upper 99%	Lower 99%	PDER	PDSR Mean	Upper 99%	Lower 99%	PDER
a_0	0.3712	0.3516	0.3708	0.3733	0.2894	0.1334	0.3752	0.3242
a_1	1.0087	2.3892	0.9835	0.9398	12.3011	13.0432	9.1269	11.7467
a_2	-43.0667	-105.4167	-39.9404	-40.0095	-662.6320	-751.0935	-446.8393	-652.1470
a_3	567.5292	1557.3914	598.3819	512.0601	12153.3466	14727.6571	7837.5720	12308.3001
a_4	-1173.1204	-5807.4512	-2144.4920	-849.0734	-68031.8045	-87711.0810	-42682.1177	-70529.2504
a_5	0.1276	0.0791	0.2427	0.1294	0.3779	0.0840	0.8351	0.3785
a_6	0.3115	0.3550	-0.5379	0.2882	-3.7904	-5.2045	-5.7942	-3.8837
b_0	2.006	1.620	2.212	2.0411	1.5277	0.7965	2.4637	1.7321
b_1	4.841	19.720	10.951	3.6068	67.2118	44.9229	82.5688	72.7179
b_2	-321.181	-909.665	-637.673	-272.2806	-3683.1338	-2525.6956	-4300.5362	-4093.6916
b_3	846.332	10465.556	6707.056	-58.9649	63759.0846	47184.1324	68857.4691	72132.2957
b_4	27223.189	-22952.443	-10244.141	32786.2976	-336712.3631	-270084.1075	-337914.749	-386504.7502
b_5	0.832	-3.726	4.505	0.9003	-8.1382	-13.3160	2.5661	-9.9594

the steepness parameter, k_1 is the wavenumber, T_1 is the mean wave period, and d is the water depth. The Huang PDSR and PDER coefficients in Eq. (19) are summarized in Table 4.

$$P(\eta_c > \eta) = \exp\left[-8\frac{\eta^2}{H_s^2}\right] \tag{17}$$

$$P(\eta_c > \eta) = \exp\left[-\left(\frac{\eta}{\alpha H_s}\right)^{\beta}\right] \quad \begin{matrix}\alpha = 0.3536 + 0.2892 S_1 + 0.106 U_r \\ \beta = 2 - 2.1597 S_1 + 0.0968 U_r^2\end{matrix} \tag{18}$$

$$P(\eta_c > \eta) = \exp\left[-\left(\frac{\eta}{\alpha' H_s}\right)^{\beta'}\right] \tag{19}$$

$$\alpha' = a_0 + a_1 S_1 + a_2 S_1^2 + a_3 S_1^3 + a_4 S_1^4 + a_5 U_r + a_6 U_r^2$$
$$\beta' = b_0 + b_1 S_1 + b_2 S_1^2 + b_3 S_1^3 + b_4 S_1^4 + b_5 U_r^2$$

$$U_r = \frac{H_s}{k_1^2 d^3} \quad S_1 = \frac{2\pi}{g}\frac{H_s}{T_1^2} \quad k_1 = \frac{4\pi^2}{g T_1^2} \tag{20}$$

Fig. 5 presents the PDSR curves from 100 realizations and compares them with the reference distributions. Each graph presents a sea state, and every subplot presents a combination of HOS parameters. The name of each computational setup is written inside the subplot, and all subplot shares the same axis limits. Each marker presents a wave crest height probability, and the mean PDSR curve is an average of all wave crest height probability distributions from 100 wave realizations. The analyses of the PDSR markers and the mean PDSR curve are described as follows

First, the PDSR markers and the mean PDSR curves were compared with the reference distributions. With the HOS mode $N_x = 128$, the change of HOS order did not influence the mean PDSR curves significantly, and the mean PDSR curves mostly follow the Rayleigh distribution regardless of the wave condition. With HOS modes $N_x = 256$ and $N_x = 512$, a meaningful difference was measured with the change in the HOS order. When the first-order ($M = 1$) was applied, the mean PDSR curves followed the Rayleigh distribution regardless of the number of HOS modes. When the second-order ($M = 2$) was used, the mean PDSR curves followed the Forristall distribution. This trend was presented more distinctly for the higher sea states.

The third-order ($M = 3$) and the fourth-order ($M = 4$) HOS simulations with HOS modes $N_x = 256$ and $N_x = 512$ were compared for sea states 5 and 7. The mean PDSR curves mostly lied between the Forristall distribution and the Huang mean distribution. The mean PDSR curve showed a significant increase as the number of HOS mode increased. Moreover, the variations of the PDSR markers from the mean PDSR curve has changed as the number of HOS mode increased. For example, in the case 'sea state 7/$M = 4/N_x = 256$' and 'sea state 7/$M = 4/N_x = 512$', the number of PDSR markers under the Huang 99% lower bound decreased, and the number of PDSR markers close to the Huang 99% upper bound increased. This result suggests that HOS mode $N_x = 512$ is required to generate extreme wave events. One reason for this variation of PDSR markers is the increase in the Nyquist frequency and the increase in HOS mode. The increase in Nyquist frequency leads to more proper modeling of high-frequency wave components and the nonlinearity of waves.

Second, the PDSR markers were compared with the Huang 99% bounds. Considering the concept of the Huang 99% bounds, the PDSR markers are expected to mostly be in the Huang 99% bounds. Therefore, the analysis counts all wave crest heights with their POE lower than 10^{-2} and compares them with the Huang bounds. Table 5 lists the occurrence rate of the measured wave crest height POE not being inside the Huang bounds for POE lower than 10^{-2} for each sea state and each HOS computational parameter. The computational setup with an occurrence rate higher than 10% is colored red, higher than 5% is colored yellow, and lower than 5% is colored green (Table 5).

For sea states 3 and 4, which are almost linear wave conditions, the influence of HOS parameters was smaller than in the other sea states. On the other hand, for the sea states 5 to 7, more than half of the PDSR

Table 5 Occurrence rate of the measured wave crest height POE not being inside of the Huang bounds for POE lower than 10^{-2}.

Out of Huang bound (%)	Sea state 3			Sea state 4		
Order (M) \ Mode (N_x)	128	256	512	128	256	512
1	8.73%	9.21%	9.04%	27.93%	25.00%	24.79%
2	2.50%	0.63%	0.10%	8.20%	1.81%	2.53%
3	2.72%	0.26%	0.05%	5.93%	1.75%	0.06%
4	2.67%	0.21%	0.20%	6.13%	1.31%	0.00%

Out of Huang bound (%)	Sea state 5			Sea state 6			Sea state 7		
Order (M) \ Mode (N_x)	128	256	512	128	256	512	128	256	512
1	65.43%	71.11%	69.11%	61.18%	58.60%	60.67%	61.44%	57.97%	58.80%
2	34.43%	15.42%	3.79%	29.91%	11.38%	3.08%	35.56%	13.31%	5.30%
3	38.86%	8.01%	0.73%	31.82%	5.34%	1.17%	34.44%	7.20%	1.40%
4	37.14%	8.35%	1.33%	31.45%	6.28%	1.17%	34.33%	8.13%	2.00%

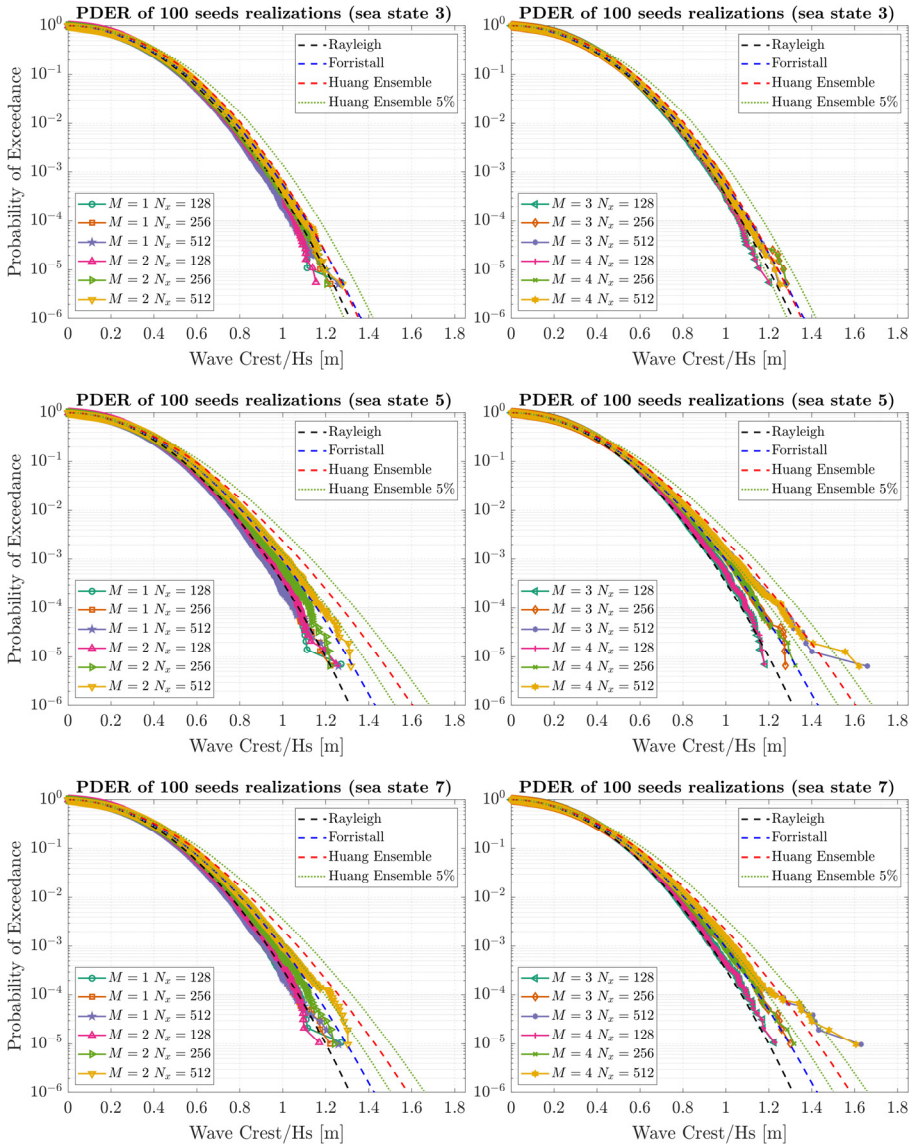

Fig. 6 PDER of 100 realizations with different combinations of HOS parameters for all sea states. These are compared with the Rayleigh (first-order), the Forristall (second-order) and the Huang (semi-empirical formula) distributions.

markers measured from first-order ($M=1$) HOS simulations were lower than the Huang 99% lower bound. The occurrence rate gradually decreases as the HOS order increases from $M=1$ to $M=3$. While the difference between $M=3$ and $M=4$ was minimal. Similarly, the occurrence rate decreases as the number of HOS modes increases. The lowest occurrence rate for each sea state was commonly found with HOS setup $M=3/N_x=512$ or $M=4/N_x=512$, and those values were retained under 2%.

Fig. 6 compares PDER curves of 100 realizations and the reference distributions for sea states 3, 5, and 7. An additional reference distribution presenting the 5% bound of the Huang ensemble distribution was added as an indicator. For sea states 3, due to the lack of nonlinearity, the difference between each PDER curve with different computational setups was smaller than the other sea states. For sea states 5 and 7, a significant change in wave crest height was observed, particularly at the POE level of 10^{-5}.

The PDER curves obtained from the first-order HOS simulations for all sea states agree well with the Rayleigh distribution. The PDER curves of the second-order HOS simulations matched well with the Forristall distribution when the number of HOS modes was higher than $N_x=256$. The third- and fourth-order PDER results usually lie between the Forristall distribution and the Huang PDER distribution, while the difference between the two HOS orders is minimal. The $M=3/N_x=512$ and $M=4/N_x=512$ setups showed the best compromise among all HOS computational setups with the Huang ensemble distribution. Within the POE level between 10^{-2} and 10^{-4}, the HOS PDER curves follow the −5% bound of Huang ensemble distribution. Within the POE level between 10^{-4} and 10^{-6}, HOS PDER curves show overestimated wave crest probability compared to the Huang ensemble distribution. On the other hand, the number of realizations is insufficient to conclude the PDER curve's accuracy at the POE level of 10^{-5}.

5. Conclusions

This paper performed a parametric study on the open-source program HOS-Ocean. With three numbers of HOS modes (N_x) and four levels of HOS orders (M), twelve combinations of HOS computational parameters were applied to the HOS simulations to find the recommended HOS parameters for irregular wave generation. Therefore, 100 three-hour realizations of HOS waves were made for five sea states, and the quality waves were verified by following qualification procedures.

First, the spectral analysis was performed with twelve combinations of HOS setup and five sea states, and the averaged wave spectrum was compared with the target wave spectrum. The maximum and average spectral differences were quantitatively analyzed within the target frequency range using ±5% tolerance. Second, the nonlinearity of irregular waves with respect to the HOS parameters and the variation of sea states were checked by comparing the POE of the wave crest height. The PDSR and PDER of 100 realizations were compared with the reference probability distributions, and the influence of HOS parameters and sea states on the nonlinearity of irregular waves was investigated. As a result, the following conclusions were acquired.

(1) The results with HOS modes $N_x=128$ show overestimated wave spectrum and underestimated wave crest height regardless of the HOS order. Consequently, the HOS mode was larger than $N_x=128$ is required for the current HOS computational setup, regardless of the sea state.

(2) The minimum spectral difference (averaged absolute difference ratio) was found when the first order was applied. The spectral difference increases as the HOS order increases. On the other hand, regardless of the HOS order and the sea state, the maximum difference ratio was maintained below 5%, and the averaged absolute difference ratio was kept below 2% with HOS modes $N_x=256$ and $N_x=512$.

(3) The wave crest height PDSR and PDER for different combinations of HOS parameters were compared with the reference distributions.

- When the first-order HOS order was used, the wave crest height was significantly underestimated even for sea states 3 and 4. This underestimation clearly showed that it is important to check both the wave spectrum and the wave crest height POE for the irregular wave analysis.
- Comparing the PDSR of the second-, third-, and fourth-order HOS simulation with the Hunag 99% bounds, the HOS wave crest generated using two combinations of HOS parameters $M=3/N_x=512$ and $M=4/N_x=512$were considered adequate for all sea states. For sea state 3, other HOS setups, such as $M=2/N_x=256$ or $M=2/N_x=512$ were considered appropriate.

(4) The HOS setups, $M=3/N_x=512$ and $M=4/N_x=512$, satisfy the ±5% tolerance in the spectral analysis. The amount of nonlinearity of waves measured using the two HOS setups was verified by comparing the wave crest height POE with the Huang PDSR and PDER distributions. The difference in wave properties between the two HOS setups was small. In conclusion, considering that the HOS domain length is $15\lambda_p$, the suggested HOS computational parameter would be $\lambda_p/\Delta x \geqq 35$ with $M=3$.

Conflict of Interest

No potential conflict of interest relevant to this article was reported.

Funding

This work was supported by Pusan National University Research Grant, 2021 and supported by BK21 FOUR Graduate Program for Green-Smart Naval Architecture and Ocean Engineering of Pusan National University.

References

Bouscasse, B., Califano, A., Choi, Y. M., Haihua, X., Kim, J. W., Kim,

Y. J., Lee, S. H., Lim, H. -J., Park, D. M., Peric, M., Shen, Z., & Yeon S. M. (2021). Qualification criteria and the verification of numerical waves: Part 2 CFD-based numerical wave tank. *Proceedings of* 40th International Conference on Ocean, Offshore and Arctic Engineering, OMAE2021-63710. https://doi.org/10.1115/OMAE2021-63710

Bonnefoy, F., Ducrozet, G., Le Touzé, D., & Ferrant, P. (2009). Time-domain simulation of nonlinear water waves using spectral methods. *In Advances in Numerical Simulation of Nonlinear Water Waves.* World Scientic.

Canard, M., Ducrozet, G., & Bouscasse, B. (2020). Generation of 3hr long-crested waves of extreme sea states with HOS-NWT solver. *Proceedings of the International Conference on Offshore Mechanics and Arctic Engineering,* OAME2020-18930. https://doi.org/10.1115/OMAE2020-18930

Canard, M., Ducrozet, G., & Bouscasse, B. (2022). Varying ocean wave statistics emerging from a single energy spectrum in an experimental wave tank. *Ocean Engineering, 246*, 110375. https://doi.org/10.1016/j.oceaneng.2021.110375

Choi, Y.M. (2019). Two-way coupling between potential and viscous flows for a marine application [Doctoral dissertation, Ecole Centrale de Nantes].

Choi, Y.M., Bouscasse, B., Seng, S., Ducrozet, G., Gentaz, L., & Ferrant, P. (2018). Generation of regular and irregular waves in Navier-stokes CFD solvers by matching with the nonlinear potential wave solution at the boundaries, *Proceedings of 37th International Conference on Ocean, Offshore and Arctic Engineering, Madrid, Spain,* OMAE2018-78077. https://doi.org/10.1115/OMAE2018-78077

Dommermuth, D., & Yue, D. (1987). A high-order spectral method for the study of nonlinear gravity waves. *Journal of Fluid Mechanics, 184*, 267-288. https://doi.org/10.1017/S002211208700288X

Ducrozet, G., Bonnefoy, F., Le Touzé, D., & Ferrant, P. (2007). 3-D HOS simulations of extreme waves in open seas. *Natural Hazards and Earth System Sciences, 7*(1), 109−122. https://doi.org/10.5194/nhess-7-109-2007

Ducrozet, G., Bonnefoy, F., Le Touzé, D., & Ferrant, P. (2012). A modied high-order spectral method for wavemaker modeling in a numerical wave tank. E*uropean Journal of Mechanics - B/Fluids, 34*, 19−34. https://doi.org/10.1016/j.euromechflu.2012.01.017

Ducrozet, G., Bonnefoy, F., Le Touzé, D., & Ferrant, P. (2016). HOS-ocean: Open-source solver for nonlinear waves in open ocean based on High-Order Spectral method. *Computer Physics Communications, 203*, 245−254. https://doi.org/10.1016/j.cpc.2016.02.017

Forristall, G. Z. (2000). Wave crest distributions: Observations and second-order theory. *Journal of Physical Oceanography, 30*(8), 1931−1943. https://doi.org/10.1175/1520-0485(2000)030<1931:WCDOAS>2.0.CO;2

Goda, Y. (1983). Analysis of wave grouping and spectra of long-travelled swell. *Report of Port and Harbour Research Institute, 22*(1), 3−41.

Hamada, T. (1965). The secondary interactions of surface waves. *Report of Port and Harbour Research Institut.*

Huang, Z., & Zhang, Y. (2018). Semi-empirical single realization and ensemble crest distributions of long-crest nonlinear waves. *Proceedings of the ASME 2018 37th International Conference on Ocean, Offshore and Arctic Engineering* (Vol. 1, V001T01A032). American Society of Mechanical Engineers. https://doi.org/10.1115/OMAE2018-78192

Kim, C. H. (2008). *Nonlinear waves and offshore structures,* World Scientific. https://doi.org/10.1142/4906

Lee, W. T., & Bales, S. L. (1984). Environmental data for design of marine vehicles. In *Ship Structure Symposium.*

Lewis, E. V. (1989). *Principles of naval architecture second revision: Volume III- Motions in waves and controllability.* Society of Naval Architects and Marine Engineers.

Li, Z., Deng, G., Queutey, P., Bouscasse, B., Ducrozet, G., Gentaz, L., Touzé, D. Le, Ferrant, P., Le Touzé, D., & Ferrant, P. (2019). Comparison of wave modeling methods in CFD solvers for ocean engineering applications. *Ocean Engineering, 188*, 106237. https://doi.org/10.1016/j.oceaneng.2019.106237

Longuet-Higgns, M. S. (1952). On the statistical distribution of the heights of sea waves. *Journal of Marine Research, 11*(1), 245−266.

Lu, X., Dao, M.H., Le, Q.T. (2022). A GPU-accelerated domain decomposition method for numerical analysis of nonlinear waves-current-structure interactions. *Ocean Engineering, 259*, 111901. https://doi.org/10.1016/j.oceaneng.2022.111901

Tick, L. J. (1963). *Nonlinear probability models of ocean waves.* Prentice-Hall.

Welch, P. D. (1967). The use of fast Fourier transform for the estimation of power spectra: A method based on time averaging over short, modified periodograms. *IEEE Transactions on Audio and Electroacoustics, 15*(2), 70−73. https://doi.org/10.1109/TAU.1967.1161901

West, B. J., Brueckner, K. A., Janda, R. S., Milder, D. M., & Milton, R. L. (1987), A new numerical method for surface hydrodynamics. *Journal of Geophysical Research, 92*(C11), 11803−11824. https://doi.org/10.1029/JC092iC11p11803

Xiao, Q., Zhu, R., & Huang, S. (2019). Hybrid time-domain model for ship motions in nonlinear extreme waves using HOS method. *Ocean Engineering, 192*, 106554. https://doi.org/10.1016/j.oceaneng.2019.106554

Author ORCIDs

Author name	ORCID
Kim, Young Jun	0000-0002-1648-6485
Baek, Hyung Min	0000-0002-8363-6746
Yang, Young Jun	0000-0002-8635-2474
Kim, Eun Soo	0000-0002-1132-3046
Choi, Young-Myung	0000-0002-7397-3933

KSOE

Journal of Ocean Engineering and Technology 37(1), 31-37 February, 2023
https://doi.org/10.26748/KSOE.2022.039

pISSN 1225-0767
eISSN 2287-6715

Original Research Article

A Study on Design Variables for Increasing the Breaking Strength of Synthetic Fiber Chain

Kyeongsoo Kim[1], Seonjin Kim[2], Hyunwoo Cho[1], Dokyoun Kim[3], Yongjun Kang[3] and Taewan Kim[2]

[1]*Senior Researcher, Special Ships Advanced Technology Center, Research Institute of Medium & Small Shipbuilding, Changwon-si, Korea*
[2]*Professor, Department of Mechanical Engineering, Pukyong National University, Busan, Korea*
[3]*Director, Technical Research Center, DSR Corp., Busan, Korea*

KEYWORDS: Fiber chain, Synthetic fiber, Breaking strength, Design variables, Main effect

ABSTRACT: *In this study, a fiber chain was developed to replace a steel chain using high-modulus polyethylene DM20. The pick count, wrapping count, and inner length were selected as the main design variables of the fiber chain and were analyzed to increase the breaking strength. Orthogonal array experiments were conducted, and the results were analyzed with respect to the breaking strength. The analysis revealed that the pick count and wrapping count had meaningful effects at significance levels within 5%. The main effect analysis revealed that a smaller pick count, larger wrapping count, and longer inner length caused the breaking strength to increase. With the wrapping count fixed at 1, a pick count less than -0.65, and an inner length greater than 0.38, the breaking strength was calculated to be greater than 300 kN. These results are expected be important factors in the derivation of an optimal combination of design variables to attain a fiber chain with a targeted strength.*

1. Introduction

An ordinary link chain used in industry consists of several steel rings. A link chain is used to transport heavy goods by connecting them to machinery such as cranes and winches and fixing heavy objects in designated positions. The wire diameter of a load chain, which is a representative type of link chain, is selected based on the required load capacity. However, a steel chain has a disadvantage of its weight increasing in proportion to the working load and wire diameter, which significantly reduces the workability and limits the scope of application. Therefore, industrial sites that directly use chains demand a steel chain that is lightweight with high usability, and marine engineering research is underway to develop new products that use fiber as a modified material. Operations involving chains reveal that the tensile force is the most important product specification factor, and it is necessary to study design technology for a fiber chain that can meet the required specifications.

Steel is mostly used in industrial applications, but synthetic fiber has been used for a long time in mooring systems for ships and offshore structures. Among synthetic fiber chains used for lifting large loads, synthetic fiber ropes were first proposed for use as mooring lines in the 1960s, and since then, extensive studies have been conducted for their practical use (Banfield and Casey, 1998). Del Vecchio (1992) was the first to carry out systematic research on the mechanical behavior of polyester ropes. The dynamic stiffness, creep, and fatigue behavior of polyester ropes were examined as essential characteristics for application of polyester ropes in deepwater moorings. Petruska et al. (2010) installed the first offshore polyester mooring system in the Campos Basin, Brazil.

Over time, polyester ropes have become the preferred option of mooring line installation up to a depth of 1500 m. However, with increasing number of natural resources being discovered at increasing water depths, it remains to be explored whether polyester ropes can be utilized at these depths and whether they can provide sufficient stiffness to maintain adequate platform offsets (Davies et al., 2002). As offshore oil and gas surveys move to deep seas, mooring with polyester ropes has faced two challenges. The first problem is the size and weight of polyester ropes that are often considerably thick and long, which may exceed the allowable capacity of anchor handling boats and cause problems in installation (Chi et al., 2009; Det Norske Veritas, 2018). The second problem is that polyester ropes can have large elongations, which may lead to horizontal offsets exceeding the riser limit at depths of >2000 m (Fernandes et al., 1999).

To address these limitations, ultra-high-molecular-weight

Received 25 November 2022, revised 19 January 2023, accepted 25 January 2023
Corresponding author Taewan Kim: +82-51-629-6142, tw0826@pknu.ac.kr

polyethylene (UHMWPE) was developed. Also known as high-modulus polyethylene (HMPE), it has been widely applied as the most suitable material for deep-sea mooring lines. HMPE ropes are lighter than polyester ropes under equivalent minimum breaking load conditions and have smaller diameters and higher stiffnesses. Thus, HMPE ropes have technical as well as operational advantages over traditional polyester ropes for applications in deep-sea mooring (Peter et al., 2011; Davies et al., 2015). HMPE mooring systems with high stiffness are better for risers in terms of offset than polyester mooring lines, and HMPE ropes typically break at 2−2.5% elongation after use, while polyester ropes break at 12−15% elongation.

While the positions of offshore structures are held static, the waves apply a cyclic load on the mooring lines, which changes the fiber elongation, so the mooring line is subjected to an extension-retraction fatigue load. In one study, an HMPE rope showed a longer fatigue life than a polyester rope with the same structure, and its axial compression fatigue properties were not inferior to those of an aramid fiber sample (Garrity and Fronzaglia, 2008, Leite and Boesten, 2011). A hybrid rope prepared with a combination of HMPE and polyester has been proposed for mooring systems located in areas with risk of storms and hurricanes, where rope stiffness and elasticity are required at the same time. Theoretical and numerical studies of polyester mooring lines have been conducted for coupled dynamic analysis with deep-sea floating platforms (Bunsell et al., 2009, Leite et al., 2011, Tahar and Kim, 2008).

The mechanical behavior of synthetic fiber ropes directly impacts mooring responses (Weller et al., 2014). Berryman et al. (2002) examined the residual strength of HMPE ropes for use in mooring lines of mobile offshore drilling units (MODUs) for 110 days and showed that the HMPE rope was still in good condition compared to the initial state. Williams et al. (2002) performed small-scale static tensile testing using polyester elements and sub-rope components to examine damaged ropes. Ward et al. (2006) tested the length-to-diameter ratio's effects on polyester ropes used for mooring to determine the effect of damage on their residual strengths and developed guidelines for mitigating damage in polyester rope mooring lines. Da Costa Mattos and Chimisso (2011) modeled creep tests of HMPE fibers used in ultra-deep-sea mooring ropes and compared the expected lifetime and elongation (%) of the test specimens at various load levels and temperatures. Cédric et al. (2020) analyzed the extension load sensitivity characteristics of HMPE ropes according to the initial load change, and Gen et al. (2021) conducted an experimental study on the dynamic stiffness of full-size HMPE ropes under long-term cyclic loading conditions.

Several studies have proposed polyester and HMPE as suitable materials for preparing synthetic fiber ropes for mooring and examined their applications. With a fiber chain, strength and durability similar to those of mooring ropes are required to transport heavy objects, but their usage and required characteristics vary from those of mooring ropes. Kim et al. (2021) analyzed the quasi-static stiffness and durability change characteristics of HMPE and liquid crystal polymer (LCP) materials to select fiber materials suitable for a fiber chain. HMPE DM20 material showed excellent dynamic stiffness and high breaking strength in the same lifetime. However, there have been few studies on the strength design of fiber chains using synthetic fiber materials. Therefore, in this study, a fiber chain was designed to meet tensile force requirements using HMPE DM20 material, and the design variables were analyzed to improve the breaking strength.

2. Component Design

2.1 Design Geometry

Each link in a fiber chain is made by repeatedly winding fiber fabric to form a belt shape with a constant inner diameter and fixing the fabric using separate stitches. Many such links are connected to realize the chain length, and the product is completed by adding a shackle at the end of the chain. A fiber chain can be used with a crane or winch for heavy-duty lifting. Fig. 1 shows examples of its application by Green Pin® and the geometry of a fiber chain link. The main design variables of a link are the fabric width, inner diameter length, and number of times that the fabric is repeatedly wound to form a link.

2.2 Basic Design

The capstan equation was used for the fundamental design of the fiber chain in consideration of the load gradient:

$$T_{load} = T_{hold} \times e^{\mu\phi} \tag{1}$$

where, T_{load} represents the tension applied on the line, T_{hold} represents the resulting force exerted at the opposite side of the cylinder, μ is the coefficient of friction between the line and cylinder material, and ϕ is

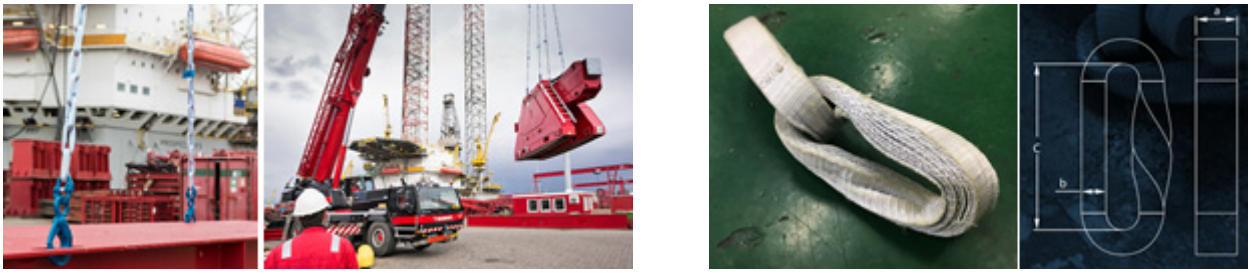

(a) (b)

Fig. 1 Design geometry: (a) Application examples in the heavy-duty lifting; (b) Geometry information for fiber chain

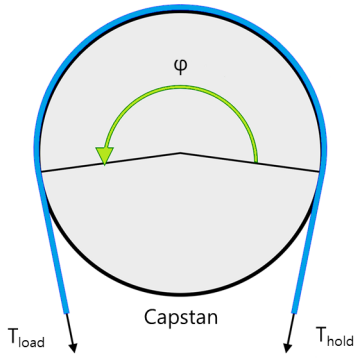

Fig. 2 Diagram of the capstan equation applied to the basic design of fiber chain

Table 1 Load gradient calculation results according to the wrapping count

T_{load} (t)	T_{hold} (t)	μ	Wrapping count
32	17.07	0.1	1
32	9.11	0.1	2
32	4.86	0.1	3
32	2.59	0.1	4
32	1.38	0.1	5
32	0.74	0.1	6
32	0.39	0.1	7
32	0.21	0.1	8
32	0.11	0.1	9
32	0.06	0.1	10

the total angle swept by all the turns of the line. The capstan equation is also known as Eytelwein's formula and relates the holding force of a flexible line to the loading force when the line is wound around a cylinder. Because of the interaction between frictional forces and tension forces, the tension on the line around the cylinder may differ from one side of the cylinder to the other. A small holding force applied on one side of the cylinder may exhibit a much larger loading force on the opposite side, depending on the wrapping count. This is how a capstan-type device operates. A fiber chain is configured using the wrapping count at a constant inner diameter, so a foundation design with a gradual load was developed using the capstan equation. Tthe layout of the equation is provided in Fig. 2.

The load according to the wrapping count can be calculated at the design breaking strength of 32 t based on the use of HMPE DM20 and assuming that the coefficient of friction is 0.1 and a wrapping count of 10, as provided in Table 1. When the wrapping count was set at its maximum of 10, the load applied to the outermost fabric of the fiber chain was calculated as 0.06 t, which is within the allowed range of the design standard.

2.3 Fabric Design

The manufacturing process for the fiber chain involved braiding yarn to produce the fiber chain fabric and loading the braid onto a loom to weave the fabric in the form of webbing. The woven fabric was then wound to produce chain links. The webbed fabric took the form of a strip, and the fabric was woven according to the pick count. The pick count is the number of intersection points for the wrap and weft contained in 25.4 mm, which affects the shape stability of the fabric and tensile performance until failure. Thus, different pick counts were used to analyze the tensile strength characteristics.

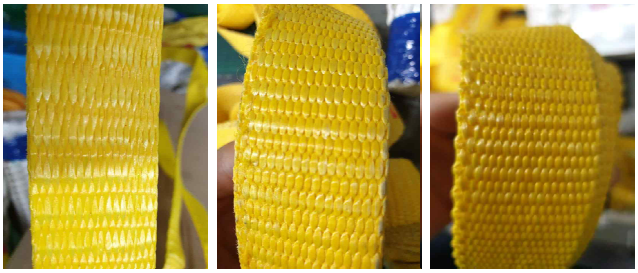

(a) (b) (c)

Fig. 3 Woven fabric shape according to the pick count: (a) 10.7; (b) 13.7; (c) 14.7

Table 2 Breaking strength results of woven fabrics according to the pick count

Pick count (/25.4 mm)	Breaking strength (kN)	Elongation (% at break)
10.7	52.1	3.50
13.7	43.9	4.33
14.7	42.4	5.17

The shape of the webbing fabric woven with a 30 mm width is shown in Fig. 3. The pick count values used in the fabric webbing were 10.7, 13.7, and 14.7, and a tensile strength test (ISO 2307- Fiber ropes, 2019) was performed on the woven fabric. The breaking strength results according to the pick count are provided in Table 2. As revealed by the breaking strength values, a smaller pick count resulted in a higher breaking strength for the woven fabric. Breaking strengths of 52.1 and 42.4 kN were observed for pick counts of 10.7 and 14.7, respectively. Because the fiber chain fabric was subjected to a tensile load in the weft direction, a lower pick count resulted in better tensile strength, and a larger pick count produced a larger fiber density, which improved the shape stability and increased the elongation. It can be seen that the shape stability and the breaking strength are parameters to consider in the design of the fiber chain.

3. Experiment Method

3.1 Range of Design Variables

The breaking strength is the primary performance factor to consider for a fiber chain. Because a fiber chain should be designed to satisfy a target strength, an experimental design method was applied to analyze the influences of the design factors on the breaking strength and derive the optimal combination of factors. During the manufacture of a fiber chain, the valid design variables include the pick count, wrapping

Table 3 The range of design variables

Pick count (/25.4 mm)	Wrapping count	Inner length (mm)
-1	-1	-1
0	0	0
1	1	1

count, and inner length. Therefore, a factorial experiment design with these design variables was conducted, and their correlations to the breaking strength were analyzed. The ranges of the design variables are provided in Table 3. The inner length is the minimum length to start wrapping the fabric. For each design variable, the variance range was set by employing one upper level and one lower level from the reference model.

3.2 Factorial Design

The design of experiments method was used to minimize the number of experiments conducted by designing an apparatus on a statistical basis. An analysis of the results based on a statistical evaluation of the hypothesis made it possible to define the relationship between the input and output variables as a function and provide the maximum amount of information with minimum experimentation and cost. In this study, an orthogonal array with three factors was adopted to analyze the relationship between the input parameters (design variables) and an output parameter (breaking strength) through experiments.

3.3 Breaking Test Method

The fiber chain specimens were fabricated, and tensile strength tests were conducted with various values for the design variables: the pick count, wrapping count, and inner length. Rope tensile-strength test equipment with 150 t capacity at DSR Corp. was used to apply loading conditions to the fiber chain. This test equipment and the experiment are shown in Fig. 4. ISO 2307 standards were used in the tests.

4. Results and Discussion

4.1 Pre-tension for Fiber Chain

A synthetic fiber rope is subjected to pre-tension due to the uneven torsional stress and torsional strength of the inner lower rope. This pre-tension improves the shape stability of the synthetic fiber rope. The effect of pre-tension on the tensile strength of the fiber chain was analyzed prior to the complete experiment because a fiber chain shares many similarities in the material and manufacturing process with a synthetic fiber rope. Generally, the pre-tension of a synthetic fiber rope is within 60% of the breaking load. When more than 85% of the breaking load is applied, the rope core may undergo plastic deformation, which significantly decreases the elastic modulus despite the increased elongation. Because of this risk of a decreased elastic modulus, a load within 60% of the breaking load is applied. Therefore, the fiber chain was prepared with pre-tension equivalent to 50% of the breaking load, and the effect was analyzed.

Fiber chain samples with a width of 30 mm were produced and used in strength tests with and without pre-tension. As summarized in the test results in Table 4, the fiber chain without pre-tension showed a breaking strength of 239.8 kN and elongation of 41.5%, while the fiber chain with pre-tension demonstrated a breaking strength of 286 kN and elongation of 14.5%. The breaking strength was the average value of three tests, and the deviations from the mean in test results were 5.41 and 8.34, respectively. The pre-tension effect caused a 16% difference in the breaking strength and a 27% difference in the elongation.

The yarn of the fiber chain gained residual tensile strength in the spinning process with torsional stress produced in the twisting and weaving processes. The residual tensile stress and torsional stress were major factors affecting the structural elongation of the fiber chain. Because the imposition of pre-tension could partially or completely eliminate the residual tensile strength and torsional stress, the increased breaking strength under the pre-tension effect was postulated to be due to the increase in the elastic modulus of the fiber chain. In addition, the fabric structure of the fiber chain became denser as a result of the pre-tension, and the elongation rate decreased.

Table 4 Breaking test results for pre-tension effect

Pre-tension	Breaking strength (kN)	Elongation (% at break)
Not	239.8	41.5
Implemented	286.1	14.5

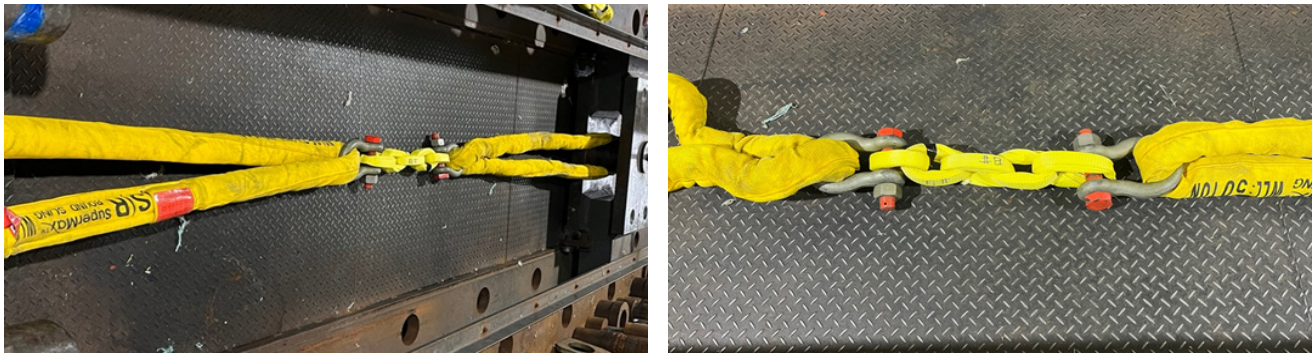

(a) (b)

Fig. 4 Test equipment: (a) Photograph of the breaking test equipment; (b) Fiber chain specimen on the test equipment

4.2 Test Results

The results of the breaking strength experiments with various design variable values are presented using an orthogonal array in Table 5. The analysis of variance (ANOVA) results for the breaking strength in relation to the pick count, wrapping count, and inner length are shown in Table 6. The ANOVA results indicate the degree of freedom (DF), sum of the adjusted squared deviation (Adj SS), sum of the adjusted mean square (Adj MS), standard error of the regression (S), coefficient of the determination (R^2), F-statistic, and P-value for each term in the model. The variance (the sum of the deviation squared) determines the magnitude of the change with respect to the measurement. The sum of the deviation squared divided by the degree of freedom is the sum of the mean squared (unbiased variance). The F-statistics refer to the ratio of variances, and the P-value is the expected value of variance. An evaluation of a variable was conducted using the F-statistic and P-value, while the P-value was used in this experiment.

The Adj SS values for the pick count, wrapping count, and inner length were 1548.83, 532.04, and 151.0, respectively, as shown in Table 6. The variations in the breaking strength due to the pick count and wrapping count were greater than those of the inner length. This occurred because the density of the warp and weft constituting the cross-sectional layer of the fiber chain were direct factors in the breaking strength, and the wrapping count affected the capstan effect. The ANOVA of the breaking strength showed that the F-value was 21.66 for the pick count and 7.44 for the wrapping count, and the expected variance P-value was less than or equal to 0.05 for both variables. Therefore, it was concluded that the pick count and wrapping count were the main factors influencing the breaking strength at a significance level of 5%.

Table 5 Test results

Order	Design variables			Breaking strength (kN)
	Pick count (/25.4 mm)	Wrapping count	Inner length (mm)	
1	-1	-1	-1	296.4
2	-1	0	0	312.8
3	-1	1	1	327.2
4	0	-1	0	276.3
5	0	0	1	284.1
6	0	1	-1	295.3
7	1	-1	1	281.2
8	1	0	-1	270.5
9	1	1	0	288.1

Table 6 Analysis of general linear model on breaking strength

Source	DF	Adj SS	Adj MS	F-test	P-value
Pick count	1	1548.83	1548.83	21.66	0.006
Wrapping count	1	532.04	532.04	7.44	0.041
Inner length	1	151.00	151.00	2.11	0.206
Error	5	357.50	71.50	-	-
Total	8	-	-	-	-

S = 8.45575, R^2 = 86.19%

4.3 Main Effect Analysis

Fig. 5 displays the main effects of the pick count, wrapping count, and inner length on the breaking strength. In the main effect plot, the dotted line in the middle represents the total average of the breaking strengths, and each dot corresponds to the average value at a specific level. The breaking strength appeared larger-the-better characteristics with respect to the changes in the design variables. The main effect plots for the changes in the levels of the design variables in Fig. 5 reveal that the breaking strength increased as the pick count decreased, the wrapping count increased, and the inner length increased.

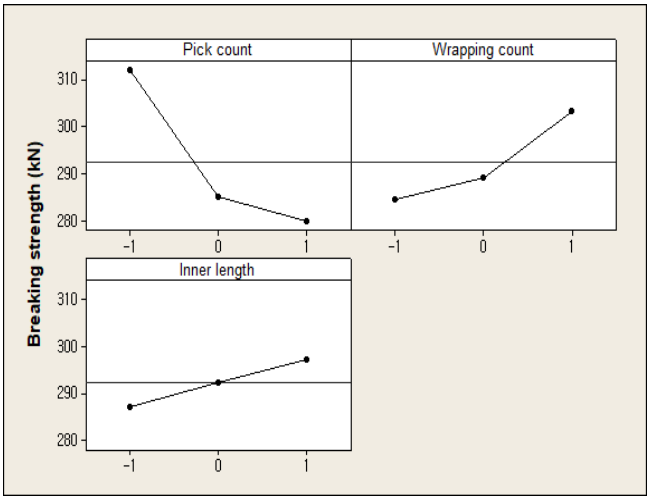

Fig. 5 Main effect plot for breaking strength

The sensitivity of each design variable to the breaking strength was determined using the delta values (difference between the maximum and minimum values) of the objective function, which are summarized in Table 7. The variable with the highest sensitivity was determined to be the pick count with a delta value of 32.1, followed by the wrapping count and inner length. The analysis revealed that the level changes in the pick count resulted in a change of up to 11.8% for the breaking strength, while changes in the wrapping count and inner length caused 6.7% and 3.5% changes, respectively. A large strength variance was observed in the pick count range from -1 to 0 and in the wrapping count range from 0 to 1.

Table 7 Sensitivity of design variables

Level	Pick count (/25.4 mm)	Wrapping count	Inner length (mm)
-1	312.1	284.6	287.4
0	285.2	289.1	292.4
1	279.9	303.5	297.4
Delta	32.1	18.8	10.0

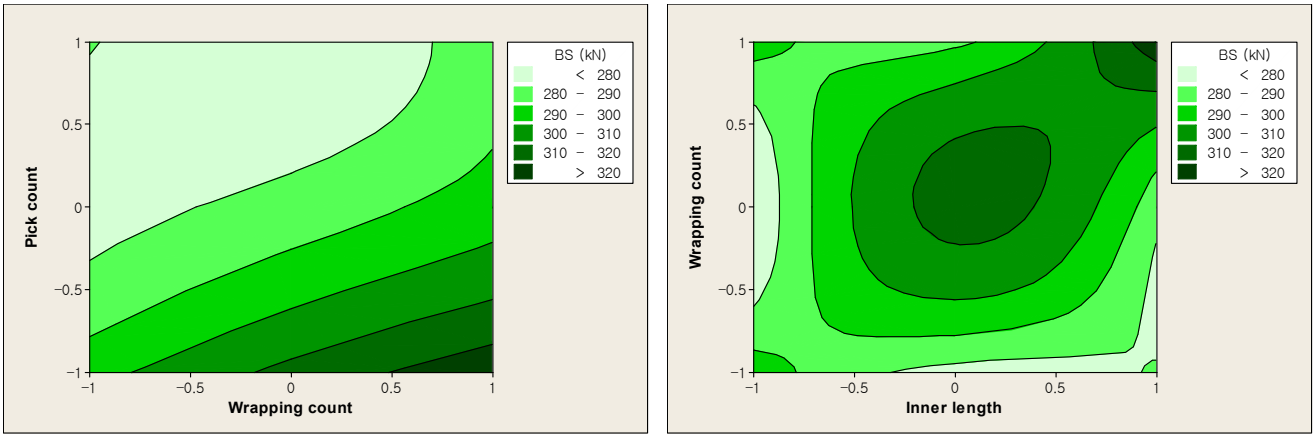

Fig. 6 Contour plot for breaking strength according to design variables

4.4 Contour Plot Analysis

A contour plot represents the response curve for a combination of design variables, and the value of an objective function is constant on each contour line. The contour lines for the pick count and wrapping count with respect to the breaking strength are plotted in Fig. 6. The maximum breaking strength is observed at a wrapping count of 1 and a pick count of -1 in Fig. 5, and the figure displays the contour lines under the same conditions. Using the results of the contour plot analysis, the breaking strength can be estimated to be greater than 300 kN when the wrapping count is fixed at 1, the pick count is less than -0.65, and the inner length is greater than 0.38. The combination of design variables made it possible to identify the region of optimal conditions that satisfy the target strength. Through additional experimentation and analysis, the derivation of a optimal design-variable combination is expected.

5. Conclusions

A fiber chain satisfying a target strength requirement was designed using HMPE DM20 to develop a replacement for a steel chain. The strength characteristics of the fiber chain in relation to the design variables were analyzed. The results of the study are summarized as follows. For the fundamental design of a fiber chain in consideration of the load gradient, the tensile force in relation to the wrapping count was calculated using the capstan equation. The load applied on the outermost fabric with a wrapping count of 10 was calculated to be 0.06 tons, which was within the allowed range. For the fabrication design of the fiber chain, the strength characteristics in relation to the pick count were analyzed. The trend of an increase in the breaking strength with decreasing pick count was observed in the chain fabric. As the pick count increased, the fabric density increased, which improved the shape stability and increased the elongation rate.

The effect of pre-tension accounting for 50% of the design strength was analyzed. The presence of pre-tension produced differences of approximately 16% in the breaking strength and 27% in the elongation. The relationships between the design variables and breaking strength were analyzed by conducting experiments using an orthogonal array. The results of the main effect analysis determined that the breaking strength increased with a decrease in the pick count, an increase in the wrapping count, and an increase in the inner length.

The sensitivity of the breaking strength to the design variables was analyzed using the delta values. Level changes in the pick count, wrapping count, and inner length produced maximum changes of 11.8%. 6.7%, and 3.5% in the breaking strength, respectively. The contour lines of the pick count and wrapping count were plotted with respect to the breaking strength. With the wrapping count fixed at 1, a pick count less than -0.65, and an inner length greater than 0.38, the breaking strength was calculated to be greater than 300 kN. The design variable characteristics of the analyzed fiber chain are expected to be utilized as important factors when deriving an optimal combination of design variables that satisfy target strength requirements.

Conflict of Interest

No potential conflict of interest relevant to this article is reported.

Funding

This research was supported by the Ministry of Trade, Industry & Energy (MOTIE) of Korea (S2641260).

References

Banfield, S., & Casey, N. (1998). Evaluation of fiber rope properties for offshore mooring. *Ocean Engineering, 25*(10), 861–79. https://doi.org/10.1016/S0029-8018(97)10017-8

Del Vecchio, C. J. M. (1992). *Light weight materials for deep water moorings* [Doctoral dissertation]. University of Reading.

Petruska, D. J., Kelly, P., Stone, B., Ahjem, V., Zimmerman, E. H., Garrity, R., & Veselis,Y. (2010). *SS: Fiber moorings, recent experiences and research: Updating API RP 2SM on synthetic fiber rope for offshore moorings* [Conference presentation]. Offshore Technology Conference, Houston, USA. https://doi.org/10.4043/20836-MS

Davies, P., Francois, M., Grosjean, F., Baron, P., Salomon, K., &

Trassoudaine, D. (2002). *Synthetic mooring lines for depths to 3000 meters* [Conference presentation]. Offshore Technology Conference, Houston, USA. https://doi.org/10.4043/14246-MS

Chi, C. H., Lundhild, E. M., Veselis, T., & Huntley, M. (2009).*Enabling ultra-depwater mooring with aramid fiber rope technology* [Conference presentation]. Offshore Technology Conference, Houston, USA. https://doi.org/10.4043/20074-MS

Det Norske Veritas. (2018).*Offshore fibre ropes* (Offshore Standard DNV-OS-E303).

Fernandes, A. C., Del Vecchio, C. J. M., Castro, G.A.V. (1999). Mechanical properties of polyester mooring cables. *International Journal of Offshore and Polar Engineering, 9*(03), 208−213.

Peter, D., Yvan, R., Loic, D., & Patrice, W. (2011). Mechanical behaviour of HMPE and aramid fibre ropes for deep sea handling operations. *Ocean Engineering, 38*(17−18), 22208−2214. https://doi.org/10.1016/j.oceaneng.2011.10.010

Davies, P., Francois, M., Lacotte, N., Vu, T. D., & Durville, D. (2015). An empirical model to predict the lifetime of braided HMPE handling ropes under cyclic eend over sheave (CBOS) loading. *Ocean Engineering, 97*, 74−81. https://doi.org/10.1016/j.oceaneng.2015.01.003

Garrity, R., & Fronzaglia, W. (2008). The use of HMPE mooring lines in deepwater MODU mooring systems. In *OCEANS 2008*, Quebec City, QC, Canada, IEEE, 1−4. https://doi.org/10.1109/OCEANS.2008.5151912

Leite, S., & Boesten, J. (2011). *HMPE mooring lines for deepwater MODUs* [Conference presentation]. Offshore Technology Conference Brazil, Rio de Janeiro, Brazil, https://doi.org/10.4043/22486-MS

Bunsell, A. R. (2009). *Handbook of tensile properties of textile and technical fibres.* Woodhead Publishing.

Tahar, A., & Kim, M. H. (2008). Coupled-dynamic analysis of floating structures with polyester mooring lines. *Ocean Engineering, 35*(17−18), 1676−1685. https://doi.org/10.1016/j.oceaneng.2008.09.004

Weller, S. D., Davies, P., Vickers, A. W., & Johanning, L. (2014). Synthetic rope responses in the context of load history: Operational performance. *Ocean Engineering, 83*, 111−124. https://doi.org/10.1016/j.oceaneng.2014.03.010

Berryman, C. T., Dupin, R. M., & Gerrits, N. S. (2002). *Laboratory study of used HMPE MODU mooring lines* [Conference presentation]. Offshore Technology Conference, Houston, USA. https://doi.org/10.4043/14245-MS

Williams, J. G., Miyase, A., Li, D. H., & Wang, S. S. (2002). Small-scale testing of damaged synthetic fiber mooring ropes [Conference presentation]. Offshore Technology Conference, Houston, USA. https://doi.org/10.4043/14308-MS

Ward, E. G., Ayres, R. R., Banfield, S. J., O'Hear, N., & Laurendine, T. (2006). *The residual strength of damaged polyester ropes* [Conference presentation]. Offshore Technology Conference, Houston, USA. https://doi.org/10.4043/18150-MS

Da Costa Mattos, H. S., & Chimisso, F. E. G. (2011). Modelling creep tests in HMPE fibres used in ultra-deep-sea mooring ropes. *International Journal of Solids And Structures. 48*(1), 144−152. https://doi.org/10.1016/j.ijsolstr.2010.09.015

Cédric, B., Peter, D., Guilhem, B., Yann, M., & Julien, B. (2020). Influence of bedding-in on the tensile performance of HMPE fiber ropes. *Ocean Engineering, 203*, 107144. https://doi.org/10.1016/j.oceaneng.2020.107144

Gen, L., Wenhua, L., Shanyin, L., Hangyu, L., Yangyuan, G., & Yuqing, S. (2021). Dynamic stiffness of braided HMPE ropes under long-term cyclic loads: A full-scale experimental investigation. *Ocean Engineering. 230*, 109076. https://doi.org/10.1016/j.oceaneng.2021.109076

Kim, K, Kim, T., Kim, N., Kim, D., Kang, Y., & Kim, S. (2021). Evaluating the mechanical properties of fiber yarns for developing synthetic fiber chains. *Journal of Ocean Engineering and Technology. 35*(6), 426−433. https://doi.org/10.26748/KSOE.2021.072

International Organization for Standardization. (2019). *Fibre ropes - Determination of certain physical and mechanical properties* (ISO 2307:2019).

Author ORCIDs

Author name	ORCID
Kim, Kyeongsoo	0000-0003-3429-8063
Kim, Seonjin	0000-0001-7755-2581
Cho, Hyunwoo	0000-0002-0161-6013
Kim, Dokyoun	0000-0002-8946-9483
Kang, Yongjun	0000-0001-8964-7916
Kim, Taewan	0000-0001-7464-3752

KSOE

Journal of Ocean Engineering and Technology 37(1), 38-48 February, 2023
https://doi.org/10.26748/KSOE.2022.046

pISSN 1225-0767
eISSN 2287-6715

Original Research Article

Tracking of ARPA Radar Signals Based on UK-PDAF and Fusion with AIS Data

Chan Woo Han[1], Sung Wook Lee[2] and Eun Seok Jin[3]

[1]*Graduated Student, Department of Naval Architecture and Ocean System Engineering, Korea Maritime and Ocean University, Busan, Korea*
[2]*Associate Prof., Department of Naval Architecture and Ocean Systems Engineering, Korea Maritime and Ocean University, Busan, Korea*
[3]*Department leader, Head of Smart Ship R&D Department, DSME R&D Institute, Daewoo Shipbuilding & Marine Engineering Co. Ltd., Siheung, Korea*

KEYWORDS: Sensor fusion, AIS, Radar, Unscented Kalman filter, Probabilistic data association filter

ABSTRACT: *To maintain the existing systems of ships and introduce autonomous operation technology, it is necessary to improve situational awareness through the sensor fusion of the automatic identification system (AIS) and automatic radar plotting aid (ARPA), which are installed sensors. This study proposes an algorithm for determining whether AIS and ARPA signals are sent to the same ship in real time. To minimize the number of errors caused by the time series and abnormal phenomena of heterogeneous signals, a tracking method based on the combination of the unscented Kalman filter and probabilistic data association filter is performed on ARPA radar signals, and a position prediction method is applied to AIS signals. Especially, the proposed algorithm determines whether the signal is for the same vessel by comparing motion-related components among data of heterogeneous signals to which the corresponding method is applied. Finally, a measurement test is conducted on a training ship. In this process, the proposed algorithm is validated using the AIS and ARPA signal data received by the voyage data recorder for the same ship. In addition, the proposed algorithm is verified by comparing the test results with those obtained from raw data. Therefore, it is recommended to use a sensor fusion algorithm that considers the characteristics of sensors to improve the situational awareness accuracy of existing ship systems.*

1. Introduction

Ship collision is a major marine accident that incurs severe economic loss and causes death and environmental pollution. Although ships are equipped with cutting-edge technological devices, e.g., electric chart display and information system, automatic radar plotting aid (ARPA), automatic identification system (AIS), and integrated navigation system (INS), several studies on marine accidents confirmed that more than 80% of marine accidents are related to human factors (Hu et al., 2020). Thus, studies related to autonomous vessels have been conducted to eliminate human factors that cause marine accidents. The International Maritime Organization categorizes the level of autonomy of a maritime autonomous surface ship into four stages. A ship with automated processes and decision-making support is classified as Level 1, a ship with remote control and the ability to board sailors is classified as Level 2, a ship with remote control but no sailors is classified as Level 3, and a ship with complete autonomy and decision-making capabilities is classified as Level 4. With the ongoing development of information and communications technology, studies have been conducted on vessels that independently recognize circumstances, avoid collisions, and plan routes to satisfy a high level of autonomy.

Autonomous vessels avoid collision based on the following four steps: detection and circumstantial recognition, decision-making, route planning, and control (Woo, 2018). During the detection and circumstantial recognition stage, obstacles are detected, and circumstances are determined using heterogenous sensors installed in the ship. During the decision-making stage, the collision risk is determined for the operating vessel. During the route planning stage, the evasion steering of the ship is ascertained based on the risk of collision, and the target route is decided accordingly. Finally, the control stage includes the regulation of the steering gear and propeller for mobility that is required for sailing along the target route. Thus, a high level of accuracy is essential for the initial detection and

Received 30 December 2022, revised 5 January 2023, accepted 18 January 2023
Corresponding author Sung Wook Lee: +82-51-410-4303, swlee@kmou.ac.kr
It is noted that this paper is revised edition based on proceedings of KAOST 2022 in Jeju (Han et al., 2022).

circumstantial recognition stage to establish a safe autonomous navigation system, and the demand for the sensor fusion technique has been increasing accordingly.

With regard to sensor fusion related to ships, Kim et al. (2014) studied the vessel information fusion algorithm using the blackboard system that can manifoldly consider various types of information based on AIS and ARPA signals. However, uncertainties such as the global positioning system (GPS) location error (i.e., situations where GPS signals cannot be received), discord in AIS data update time, and instability in radar data were not considered. Habtemariam et al. (2015) studied the fusion algorithm of the measurement level that combines the AIS and radar signals based on the joint probabilistic data association (JPDA) framework and performed simulations based on the Monte Carlo Runs. In the corresponding study, they developed a fusion track to initialize based on the radar measurements, allocated the ID list of AIS signals based on the initial distribution, and proposed an algorithm that provides updated information based on AIS or radar data according to the presence of the AIS signal. However, in real situations, time was not considered during the study; moreover, the study was performed for circumstances that include both signal data.

This study proposes a fusion algorithm of AIS and UK-PDAF-based ARPA radar signal tracking data that are applicable in actual environments for the real-time recognition of circumstances (Schreier, 2017). AIS data after reception is managed based on the maritime mobile service identity (MMSI) number, and a prediction method that was implemented based on the sailing information of the vessel within the AIS location payload is used to overcome the difficulties of combining abnormal phenomenon data. Moreover, after the reception of ARPA data, UKPDAF is used for tracking and predicting to manage units of tracks and prevent abnormal phenomena based on the ARPA data. The distance of the vessel traffic and motion variable obtained from the AIS and ARPA signals, respectively, are periodically compared to perform fusion between the two signals. Lastly, this research proceeded with measurement tests from vessels that actually navigate by boarding on a training ship of Korea Maritime & Ocean University to verify the validity of the proposed sensor fusion technique.

2. Tracking Method

2.1 Unscented Kalman Filter (UKF)

This study used a tracking algorithm based on the UKF to track objects (Labbe, 2014). Table 1 lists the prediction and update steps of the linear KF and UKF for better understanding. Eqs. (1)-(3) define the prediction steps of the linear KF and UKF, and Eqs. (4)-(10) define the update steps. The symbols listed in Table 1 are presented in Table 2.

Table 1 Algorithms of UKF and linear KF

	Linear KF	UKF	
Prediction step		$\boldsymbol{X}_i = f(\mathrm{x}_i)$	(1)
	$\bar{\mathrm{x}} = \mathrm{F}\mathrm{x}$	$\bar{\mathrm{x}}_m = \sum_{i=1}^{2n+1} \mathrm{W}_i^M \boldsymbol{X}_i$	(2)
	$\bar{\mathrm{P}} = \mathrm{F}\mathrm{P}\mathrm{F}^T + \mathrm{Q}$	$\bar{\mathrm{P}} = \sum_{i=1}^{2n+1} \mathrm{W}_i^C \{\boldsymbol{X}_i - \bar{\mathrm{x}}_m\}\{\boldsymbol{X}_i - \bar{\mathrm{x}}_m\}^T + \mathrm{Q}$	(3)
Update step		$\boldsymbol{Z}_i = h(\boldsymbol{X}_i)$	(4)
		$\boldsymbol{\mu}_z = \sum_{i=1}^{2n+1} \mathrm{W}_i \boldsymbol{Z}_i$	(5)
	$\mathrm{y} = \boldsymbol{z} - \mathrm{H}\mathrm{x}$	$\mathrm{y} = \boldsymbol{z} - \boldsymbol{\mu}_z$	(6)
	$\mathrm{S} = \mathrm{H}\mathrm{P}\mathrm{H}^T + \mathrm{R}$	$\mathrm{P}_z = \sum_{i}^{2n+1} \mathrm{W}_i^C \{\boldsymbol{Z}_i - \boldsymbol{\mu}_z\}\{\boldsymbol{Z}_i - \boldsymbol{\mu}_z\}^T + \mathrm{R}$	(7)
	$\mathrm{K} = \mathrm{P}\mathrm{H}^T\mathrm{S}^{-1}$	$\mathrm{K} = \left[\sum_{i}^{2n+1} \mathrm{W}_i^C \{\boldsymbol{X}_i - \bar{\mathrm{x}}_m\}\{\boldsymbol{Z}_i - \boldsymbol{\mu}_z\}^T\right] \mathrm{P}_Z^{-1}$	(8)
	$\mathrm{x} = \bar{\mathrm{x}} + \mathrm{K}\mathrm{y}$	$\mathrm{x} = \bar{\mathrm{x}}_m + \mathrm{K}\mathrm{y}$	(9)
	$\mathrm{P} = (\mathrm{I} - \mathrm{K}\mathrm{H})\bar{\mathrm{P}}$	$\mathrm{P} = \bar{\mathrm{P}} - \mathrm{K}\mathrm{P}_z\mathrm{K}^T$	(10)

Table 2 Variables of the KF and UKF

Variable	Definition
x, $\bar{\mathrm{x}}$, $\bar{\mathrm{x}}_m$	State variable, Predicted state variable, Unscented transform predicted state variable
P, $\bar{\mathrm{P}}$, Q, R	Error covariance, Predicted error covariance, Covariance noise and Measurement noise matrix
$\boldsymbol{X}_i$, $\boldsymbol{Z}_i$	State transitioned state and Measurement transformed state
S, P_z, K	Innovation covariance, Unscented transformed innovation covariance, Kalman gain
y	Difference between measured value and predicted value
W^M, W^C	State transition weights and covariance weights for unscented transform

2.2 Probabilistic Data Association Filter (PDAF)

In real situations, several measurement values exist for a single tracking round; Fig. 1 illustrates this situation. At time t, numerous measurement values (Track #2) can either exist for each round of tracking, or there may be a situation where no measurement value exists (Track #1). The KF uses a single measurement value for a single round of tracking; however, the PDAF is significantly different because it uses multiple measurement values for a single round of tracking.

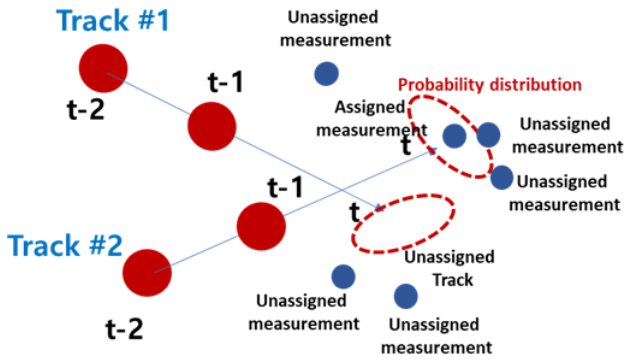

Fig. 1 Matching measurements for tracking

In this study, the PDAF first determines the Mahalanobis distance, which represents the statistical distance between current measurements and the location of previously tracked objects. If this distance is smaller than the validation gate, the corresponding measurement value is used to update the UK-PDAF. Based on this process, the value that represents the extent of the contribution of the selected measurement value to the update of the tracking object was determined, followed by the new state estimation of the target object (hereafter target) using a combined innovation technique that corresponds to innovation covariance for updating the Kalman gain.

2.2.1 Measurement value validation

The validation step involves the process of selecting relevant values among kth measurements and using the selected values for state estimation. The range of validation used during the selection process is known as the validation gate, and the volume of the validation gate is defined as

$$V_k = V_U(g)\,|\gamma_G \mathbf{S}(\mathrm{k})\,|^{1/2}$$

$$V_U(q) = \frac{\pi^{q/2}}{\Gamma(\frac{1}{2}q+1)} = \begin{cases} \dfrac{\pi^{\frac{q}{2}}}{(\frac{q}{2})!}, & q \ \ even \\ \dfrac{2^{q+1}(\frac{q+1}{2})!\pi^{\frac{q-1}{2}}}{(q+1)!}, & q \ \ odd \end{cases} \tag{11}$$

Here, q denotes the dimension of the measurement value and γ_G denotes the threshold of the gate. $\mathbf{S}(\mathrm{k})$ represents the innovation covariance matrix, which is expressed in Eq. (12).

$$\mathbf{S}(\mathrm{k}) = \mathbf{H}\mathbf{P}_{\mathrm{k}}\mathbf{H}^{\mathrm{T}} + \mathbf{R}_{\mathrm{k}} \tag{12}$$

2.2.2 Data association

The estimation process would be more reliable if the state with the conditional mean of the measurement values within the validation gate mentioned in the measurement validation step is considered. Thus, a data association step is included (Eq. (13)).

$$X_k = E[\overline{X}_k|Z_k] = \sum_{i=0}^{N_v} E[\overline{X}_k|\theta_{i,k}, Z_{i,k}]P(\theta_{i,k}|Z_k) \tag{13}$$

In Eq. (13), N_v denotes the number of valid measurements, $\theta_{i,k}$ denotes the ith valid measurement at time k, and $Z_{i,k}$ denotes the incident observed from the actual target. Moreover, $\theta_{0,k}$ denotes the incident where the valid measurements are obtained from a clutter (reflected signal that obstructs the target detection) instead of the target. Based on the aforementioned equation, it is assumed that only one measurement is derived from a single target. Therefore, $\theta_{i,k}$ $(i=0,1,\ldots,N_v)$ are exclusive events, and the probability of $\theta_{i,k}$, which is the combination of probability $\beta_{i,k}$ that the ith measurement will be derived from the actual target and probability $\beta_{0,k}$ that the measurement will be a clutter rather than an observation based on a real target, is defined in Eq. (14).

$$\beta_{i,k} \equiv P(\theta_{i,k}|Z_k) = e_{i,k}\left[b_k + \sum_{j=1}^{N_v} e_{j,k}\right]^{-1}, \quad i=1,2,\ldots,N_v$$

$$\beta_{0,k} \equiv P(\theta_{0,k}|Z_k) = b_k\left[b_k + \sum_{j=1}^{N_v} e_{j,k}\right]^{-1}, \quad i=0$$

$$e_{i,k} = e^{-\frac{1}{2}v_{i,k}^T S_k^{-1} v_{i,k}} \tag{14}$$

$$b_k = \left(\frac{2\pi}{\gamma_G}\right)^{\frac{q}{2}} \frac{N_v(1-P_D P_G)}{V_U(q)P_D}$$

Here, P_G denotes the probability that an accurate measurement exists within the validation gate and P_D denotes the probability that an accurate value is observed using the radar sensor. Both values are determined using the sensor. The derived probability of relevance is used in determining the error covariance and UK-PDAF estimation values, and the corresponding process is expressed in Eq. (15).

$$X_k = \sum_{i=0}^{N_v} \beta_{i,k}\overline{X}_k = \overline{X}_k + \mathbf{K}_{\mathrm{k}}\sum_{\mathrm{i}=1}^{\mathrm{N_v}}[\beta_{\mathrm{i,k}}\mathrm{V_{i,k}}] \tag{15}$$

$$\mathbf{P_k} = \beta_0\overline{\mathbf{P}}_{\mathrm{k}} + (1-\beta_0)[\overline{\mathbf{P}}_{\mathbf{k}} - \mathbf{K_k}\mathbf{S_k}\mathbf{K_k}^{\mathrm{T}}] + \mathbf{K}_{\mathrm{k}}\left[\sum_{\mathrm{i}=0}^{\mathrm{N_v}}\beta_{\mathrm{i,k}}\mathrm{V_{i,k}}\mathrm{V_{i,k}^T} - \mathrm{V_{i,k}}\mathrm{V_{i,k}^T}\right]\mathbf{K}_{\mathrm{k}}^{\mathrm{T}}$$

Here, $v_{i,k} = \sum_{i=1}^{N_v}\beta_{i,k}(Z_k - \overline{Z}_k)$ represents the combined innovation technique

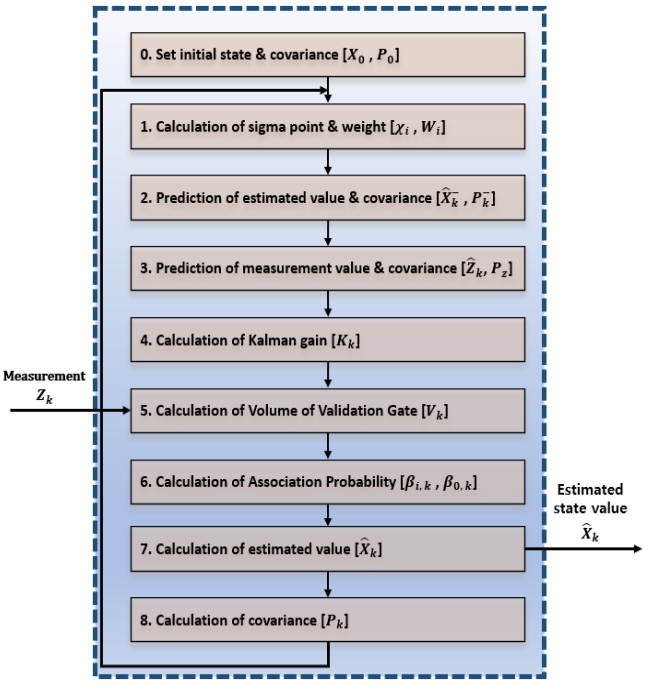

Fig. 2 Flow chart of UK-PDAF

This study develops a multi-tracking algorithm that can track (estimate) the state of the target (other ship) based on the ARPA radar measurement values obtained using the UK-PDAF-based tracking algorithm that combines the PDAF and UKF. Fig. 2 shows the flow chart of the corresponding algorithm.

3. Sensor Fusion

3.1 Location Prediction Technique Based on AIS Data

The data transfer period of AIS signals is determined based on the speed state of the vessel where the AIS system is installed, and refined data are transmitted according to the determined period. However, in reality, signals are missed owing to an increase in the load of the AIS communication channel and poor communication, from which the AIS signal period may become abnormal. Fig. 3 illustrates the aforementioned situation. As shown in Fig. 3, the red line circle represents the AIS signal received under normal circumstances, and the red dotted line circle presents the AIS signal that was not received owing to the aforementioned circumstances. The red-filled circle enclosed within a blue boundary shows the route generated from the ARPA and predicted signal through tracking. The blue-filled circle presents the actual measured signals of the ARPA radar. AIS and ARPA signals were received before step four (t-4) and step three (t-3) from the current time, within which two signals were fused. However, before step two (t-2), AIS signals were not received and updated, and only radar signals were received. Therefore, there was a significant difference between signals as time passed. This phenomenon exhibited a significant difference with regard to the track considering its location periodically updated and managed, which resulted in a loss in the combined relationship between the heterogenous signals (AIS and ARPA) for the same vessel.

To account for such uncertainty in the AIS signal, this study predicted the location of the AIS signal during sensor fusion to minimize the error caused by the long-term inability to receive the AIS signal. Moreover, the AIS signal was designed to possess a regular periodic effect identical to the ARPA signal for its use in the sensor fusion algorithm. The AIS-data-based location prediction method is defined in Eq. (16).

$$\begin{aligned} \phi_p &= \mathrm{asin}(\sin\phi_A \cdot \cos\delta + \cos\lambda_A \cdot \sin\delta \cdot \cos\theta) \\ \lambda_p &= \lambda_A + \mathrm{atan2}(\sin\theta \cdot \sin\delta \cdot \cos\phi_A, \sin\phi_A \cdot \sin\phi_p) \\ \delta &= \frac{0.5144 \cdot v \cdot (t_S - t_A)}{R} \end{aligned} \tag{16}$$

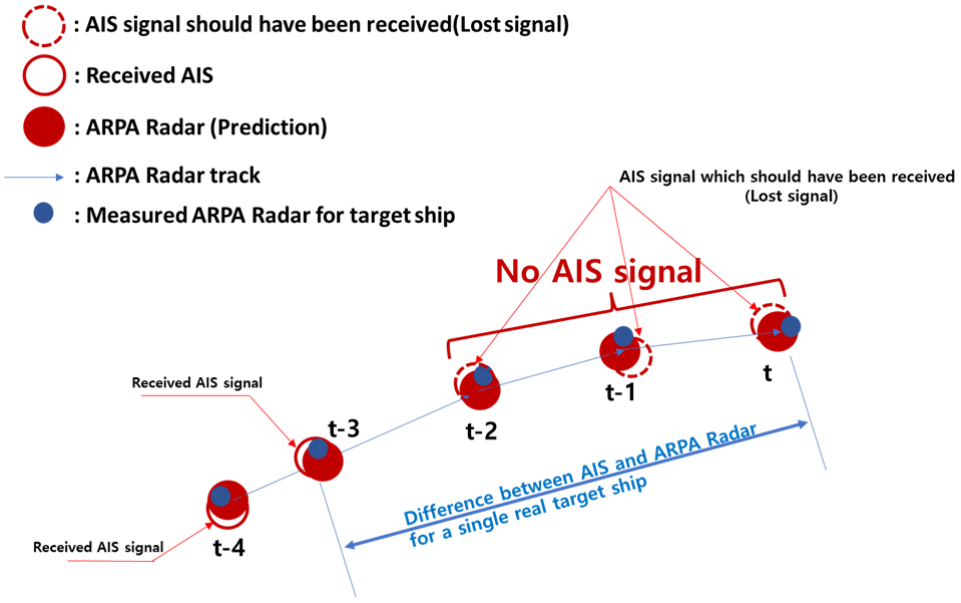

Fig. 3 Delay problem of AIS signals in real situations

Here, ϕ_p and λ_p indicate the predicted latitude and longitude during sensor fusion, respectively. ϕ_A and λ_A indicate the latitude and longitude of the received AIS signal, respectively. v denotes the ground speed, θ denotes the course over the ground, δ denotes the angular distance, t_S denotes the time of sensor fusion, and t_A denotes the reception time of the corresponding AIS signal.

3.2 Sensor Fusion Algorithm

This section introduces the sensor fusion algorithm for determining whether two vessels are identical. Fig. 4 shows a flow chart of the sensor fusion algorithm. Moreover, the first to fourth steps of this algorithm are represented by Eqs. (17)–(20), and each step is performed with AIS signals based on each ARPA radar signal that exists during sensor fusion. There is a possibility that certain AIS signals overlap and combine with multiple ARPA signals because the corresponding process is performed based on the ARPA signals. Therefore, the ARPA signals underwent four steps, and the AIS signals added to the fusion candidate during the first step were used in the fifth step for verification. In this study, it was determined whether the heterogenous signals at 3-s intervals were associated with the same vessel based on the proposed sensor fusion algorithm, and the distinction process of step 1 was presented as the first fusion step.

$$\alpha_{F_1} = \{a | d_{ar} \le \epsilon_d, a \in A, r \in R\} \tag{17}$$

$$\alpha_{F_2} = \{a | \delta_c \le \epsilon_c, \delta_c = |C_a - C_r|, a \in \alpha_{F_1}, r \in R\} \tag{18}$$

$$\alpha_{F_3} = \{a | \delta_s \le \epsilon_s, \delta_s = |S_a - S_r|, a \in \alpha_{F_2}, r \in R\} \tag{19}$$

$$a_{F_4} = \{a | d_{ar} = \min(D), a \in \alpha_{F_3}, r \in R\} \tag{20}$$

During step 1 of sensor fusion, AIS signals that are within the threshold distance are selected based on the ARPA (Eq. (17)). In step 2, the AIS signals among the selected ones with the course over the ground within the threshold were selected (Eq. (18)). In step 3, the AIS signals among those that passed step 2 with the ground speed within the threshold were selected (Eq. (19)). Herein, the course over the ground represents the angle of the sailing direction of the vessel, and it is measured up to 360° clockwise based on the latitude of 0°. In step 4, if the number of AIS signals that passed step 3 was high, the AIS signals with the minimum distance were selected (Eq. (20)). The

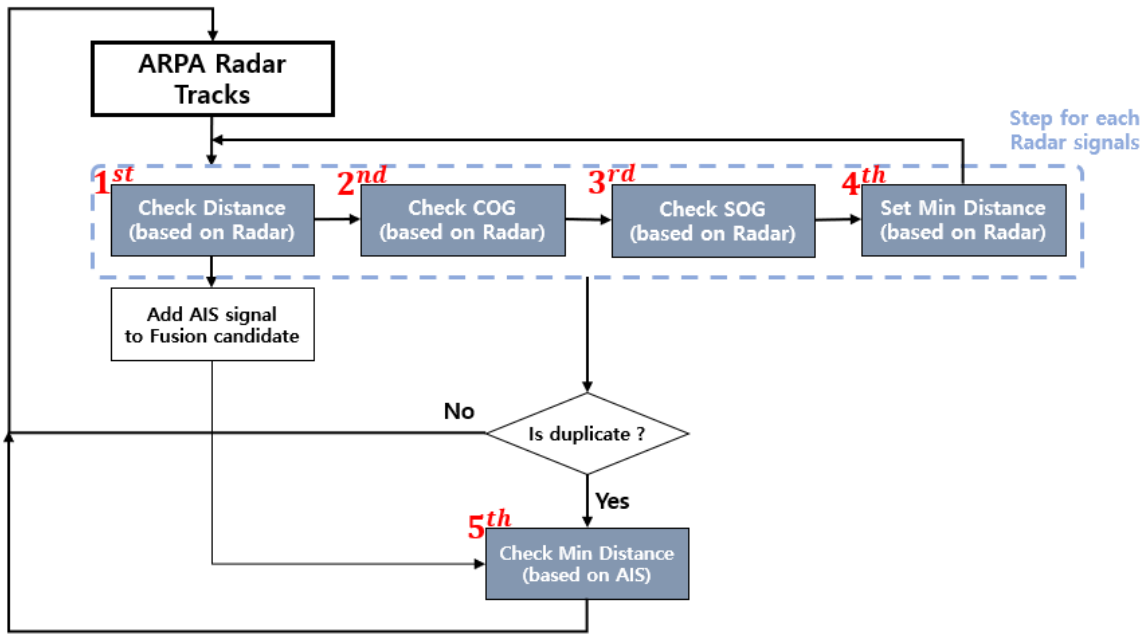

Fig. 4 Flow chart of the sensor fusion algorithm

Table 3 Variables of the sensor fusion algorithm

Variable	Definition
A, R	Set of AIS signals, Set of ARPA Radar signals
α_{F_n}	Set of AIS signals that have passed n steps
d_{ar}, δ_c, δ_s	Relative distance, Difference in course over ground, Difference in speed over ground
ϵ_d, ϵ_c, ϵ_s	Threshold of distance, Threshold of course over ground, Threshold of speed over ground
C_a, C_r	Course over ground of AIS signal, Course over ground of ARPA radar signal
S_a, S_r	Speed over ground of AIS signal, Speed oveer ground of ARPA radar signal
D	Set of distances to AIS signals that have passed the third step

definitions of the symbols in Eqs. (17)-(20) are summarized in Table 3. In this study, in order to consider both the training ship which is as field-test site was not moving during measuring and the error according to the sensor performance, the threshold for the distance between the training ship and the traffic ship, course over the ground, and ground speed was limited to 200m, 20°, and 2 knot(1.09 m/s), respectively.

4. Validation

To validate the proposed sensor fusion algorithm, the sailing equipment of Hannara Ship as the training ship of Korea Maritime & Ocean University was used for the actual measurement of the surrounding vessels. Abnormal phenomena occurred during the actual measurement, and Table 4 lists the heterogenous signals of abnormal phenomena.

Table 4 Classification of the validation case

Case	Abnormal phenomenon	Target number	MMSI of target AIS
1	O	1	440129690
2	O	2	440300740
3	O	3	440008970
4	X	4	440008970
5	X	5	440300740

In Table 4, the second and third columns indicate the presence of abnormality and target number automatically assigned by the ARPA system, respectively. The fourth column lists the MMSI number as the criteria to be discerned for the vessel based on AIS reception signals.

4.1 Result and Abnormal Phenomenon of Case 1

In Case 1, the AIS signal with MMSI number 440129690 was successfully fused with the ARPA signal with target number using the proposed method; however, an abnormal phenomenon occurred owing to the long-term non-reception of the AIS signal, which occurs owing to an increase in the AIS communication channel load, as described in Section 3.1. Fig. 5 shows the real-time measurements of this phenomenon. As shown in Fig. 5(a), the yellow line connects the green triangle (AIS signal) within circle A, and the red circle (ARPA signal) indicates that data were combined due to the fused AIS and ARPA signals. However, the radar signal location was updated, as shown in B of Fig. 5(b), after the end of the data update period (3-s update period of radar display). However, the AIS signal remained in location A of the circle without being received; Although it was the potential cause of failed sensor fusion, the AIS signal is connected to the ARPA signal as shown in Fig. 5(c), again.

Fig. 6 shows the change according to the number of fusion trials with regard to the difference between the locations of the vessel obtained from the AIS and ARPA signals ($\Delta D = Position_{AIS} - Position_{ARPA\ Radar}$) based on the analytical results of the phenomenon that occurred in Case 1. In the figure, the horizontal axis shows the number of fusion trials, and the vertical axis shows the difference in location. Moreover, the red dotted line presents the distance threshold mentioned in Section 3.2. Owing to abundant AIS data, some are indicated among the reception signals (Fig. 6) (within 500 m based on ARPA radar signal), and distinguishing the indicated symbols and colors becomes difficult. Therefore, the signals over than the red dotted line(200m threshold from the own ship) show that the locations of the traffic ships are at a far distance from the own ship(training ship). What each symbol has a parabola shape means that the traffic ship approached to the own ship in a certain duration and passed to far away.

Meanwhile, R440129690 (difference between the locations obtained based on Case 1 target 1 ARPA signal and the AIS signal with MMSI 440129690) in Fig. 6(a) shows that the fusion frequency increases with measurement time, and rapidly increases according to the long-term non-reception of the AIS signal. Fig. 6(b) shows that the aforementioned problem is resolved (R440129690, U440129690 of Fig. 6(b)) by updating the AIS signal using the proposed AIS-data-based location prediction algorithm for the same situation.

Table 5 lists the success rate of fusion with regard to the total number of attempts (138 times) for the aforementioned circumstance, and the application of the proposed method results in a higher success rate than that of the sensor fusion without additional processing.

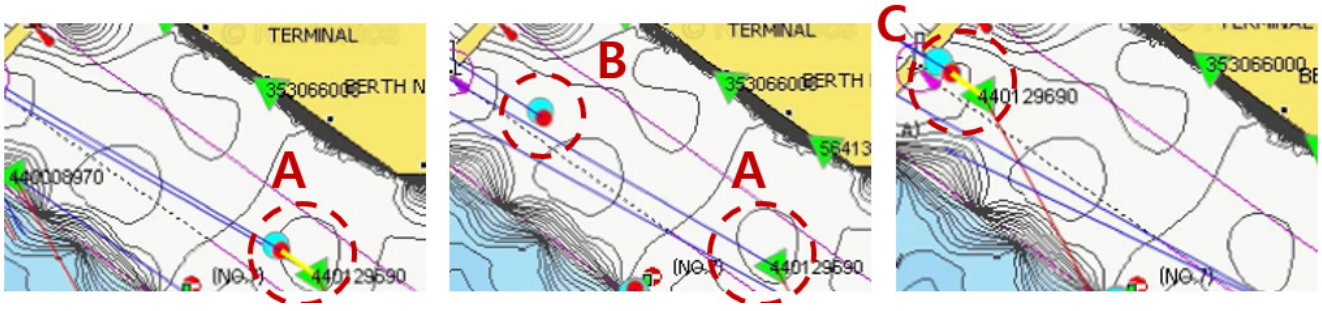

(a) (b) (c)

Fig. 5 Abnormal phenomenon in Case 1: (a) Initial state of associating each signal; (b) disassociated state after a certain time elapses; (c) reassociated state after more time elapses and AIS data are received

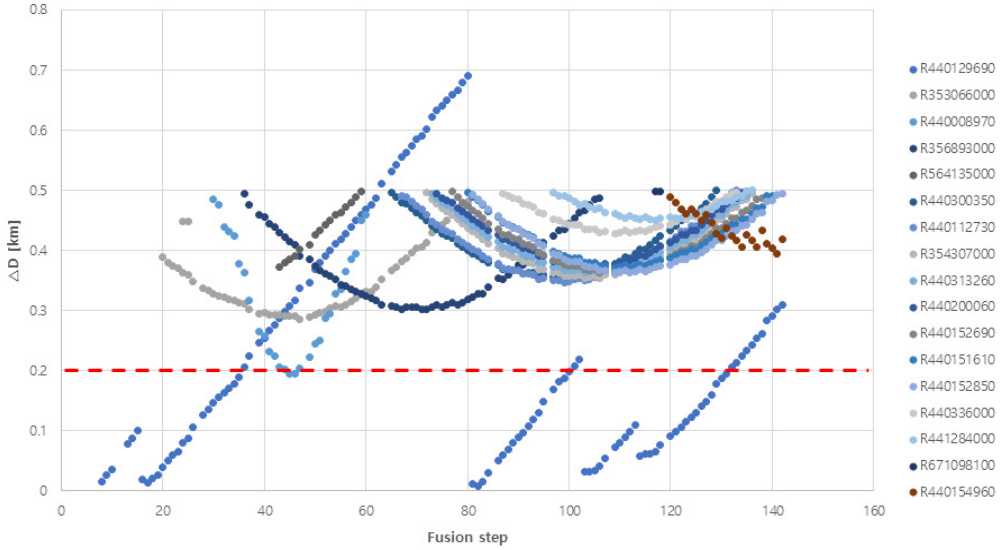

(a)

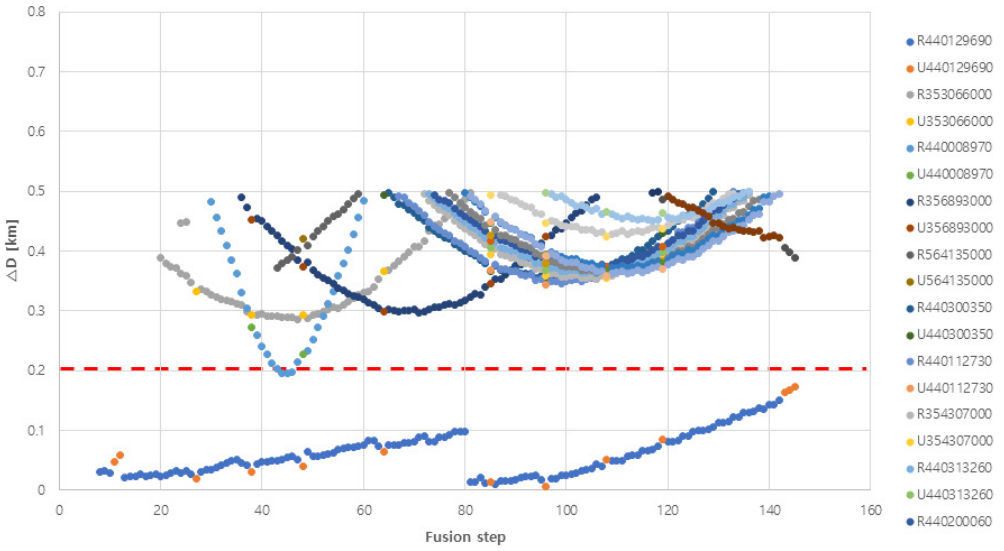

(b)

Fig. 6 Relative distance in Case 1: (a) Relative distance based on the raw data; (b) Relative distance based on the processed data

Table 5 Comparison results in Case1

Step	Raw data	Present method	Rate of change
First step	70 (50.7%)	138 (100.0%)	49.3%
Second step	122 (88.4%)	133 (96.3%)	7.9%
Third step	122 (88.4%)	133 (96.3%)	7.9%
Fusion	67 (48.5%)	133 (96.3%)	47.8%

4.2 Result and Abnormal Phenomenon of Case 2

In Case 2, fusion was successfully performed using the proposed method for the AIS signal with MMSI 440300740 and ARPA signal with target number 2; however, abnormalities may occur if a vessel that corresponds to a heterogenous signal turns rapidly. Fig. 7 shows the actual measurement phenomena in chronological order. Fig. 7(a) shows the circumstance of having succeeded in fusing AIS and ARPA signals during initial reception, and Fig. 7(b) shows the circumstance

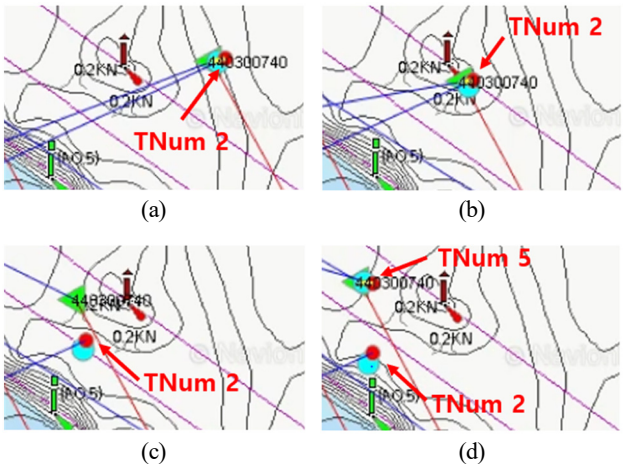

(a) (b) (c) (d)

Fig. 7 Abnormal phenomenon in Case2; (a) Initial state; (b)State before turning motion; (c) State during turning motion; (d) State after turning motion

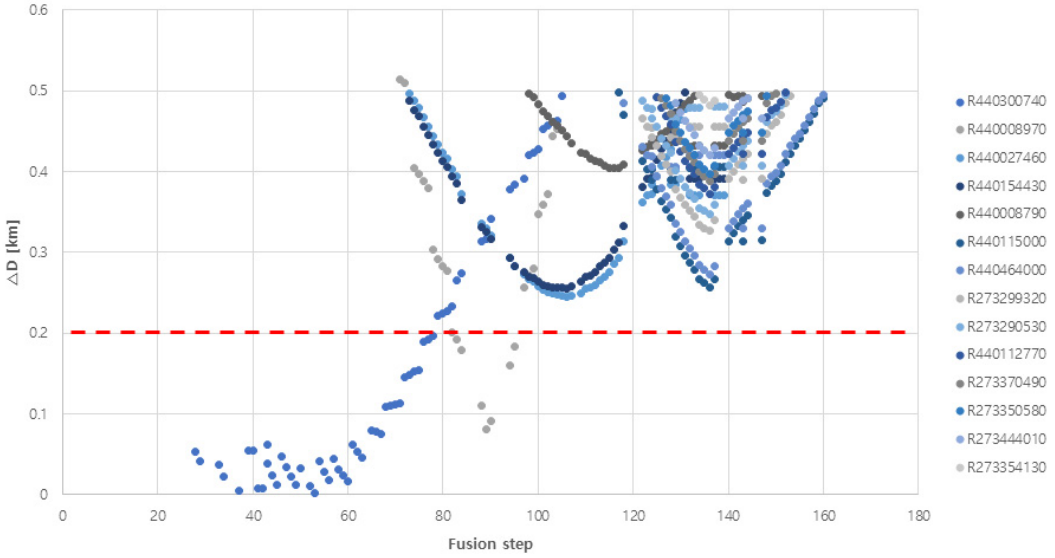

(a)

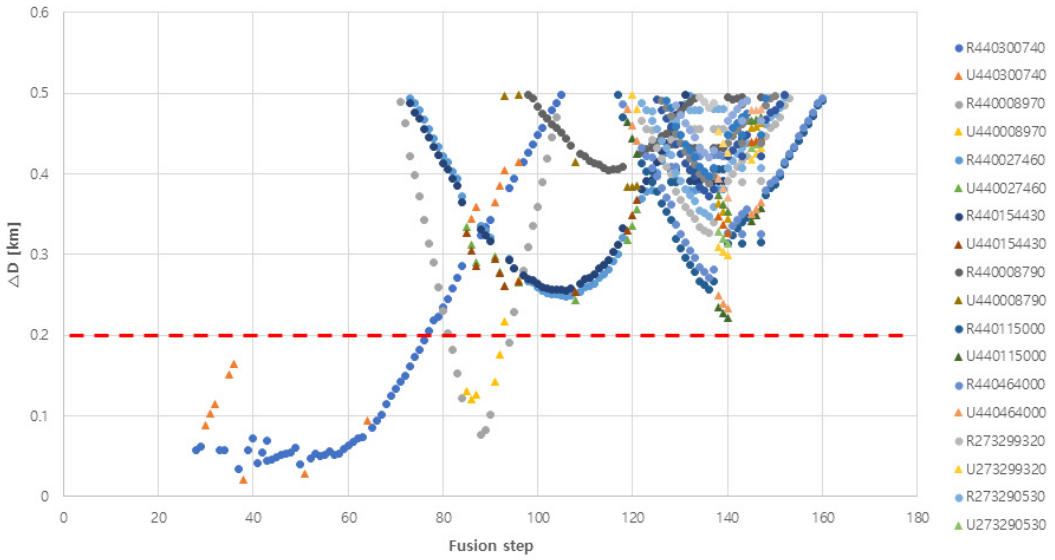

(b)

Fig. 8 Relative distance in Case 2: (a) Relative distance based on the raw data; (b) relative distance based on the processed data

when the turning motion begins. Then, a heterogenous signal or identical change must be evident for the target vessel according to its motion; however, as shown in Fig. 7(c) for TNum2 (target number 2 ARPA radar signal), the state did not change. Fig. 7(d) shows the successful fusion with the AIS signal as time passed and TNum5 had additionally been generated. This occurrence was maintained even when TNum2 departed from the sea and was determined as the malfunctioning of the ARPA device considering that the AIS signal successfully fused with additionally generating ARPA signals.

Fig. 8 shows the change that occurred based on the number of fusion attempts with regard to the difference (ΔD) between the locations of the vessel obtained from the AIS and ARPA signals (based on the analysis results of Case 2).

Meanwhile, as shown in Fig. 8(a) for R440300740 (blue circle), the number of fusion attempts increased with an increase in the measurement time, and ΔD rapidly increased owing to abnormal occurrences. Fig. 8(b) shows the application of the proposed technique for the same situation.

Table 6 lists the success rates of fusion for the total number of attempts (78 times) for the aforementioned circumstance, and the rate was higher when the proposed method was used instead of applying sensor fusion without processing.

Table 6 Comparison results of Case 2

Step	Raw data	Present method	Rate of change
First step	44 (56.4%)	50 (64.1%)	7.7%
Second step	19 (24.3%)	21 (26.9%)	2.6%
Third step	60 (76.9%)	70 (89.7%)	12.8%
Fusion	19 (24.3%)	21 (26.9%)	2.6%

4.3 Result and Abnormal Phenomenon of Case 3

In Case 3, an abnormal phenomenon occurred during the fusion attempted for the ARPA radar signal with target number 3 and AIS signal with MMSI 440008970 using the proposed method. Fig. 9 shows the chronological order of the actual measurement phenomenon. Fig. 9(a) shows the initial situation of receiving heterogeneous signals of Case 3, and the rectangle marked in red dotted line shows that the heterogenous signal within the shape is for the same vessel. However, as the data update period (the AIS signal motion data transmission period) passed, the location of the AIS signal was updated (Fig. 9(b)); however, the ARPA radar signal data were updated without changing the location. Considering that the corresponding ARPA radar signals were at a state of halt in this study, this situation was determined as a false setting of a standstill object considered as a target. Therefore, the data of this case were not considered.

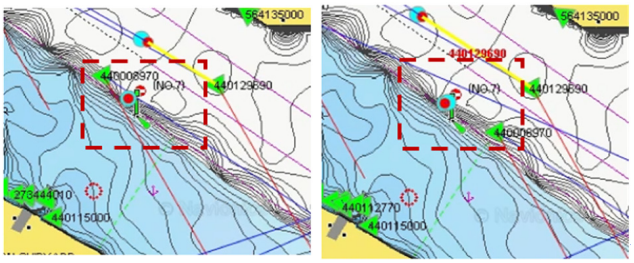

(a) (b)

Fig. 9 Abnormal phenomenon in Case 3: (a) Initial state; (b) state after some time

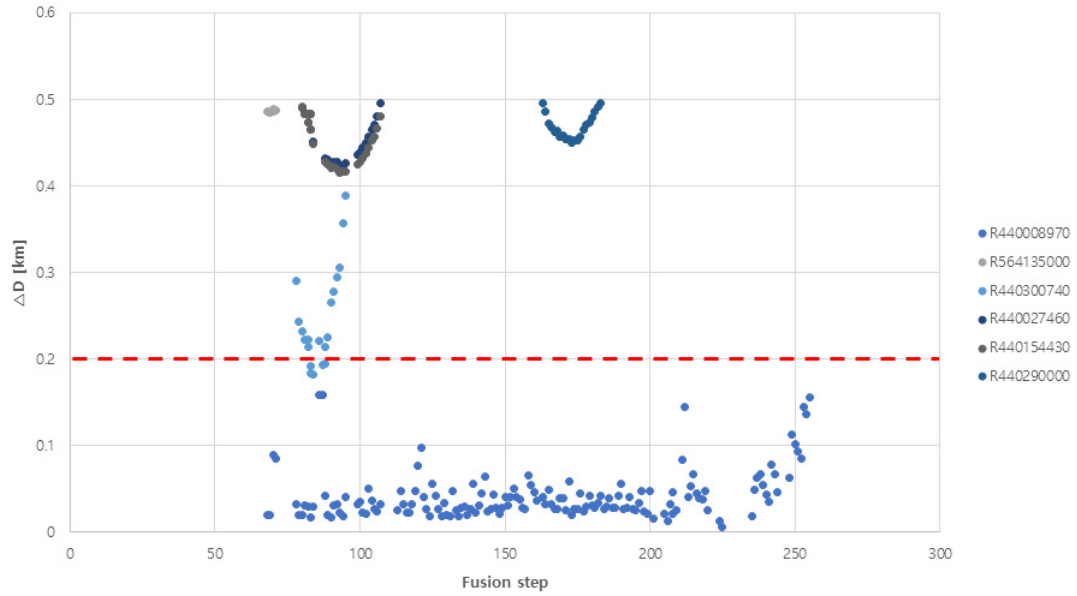

(a)

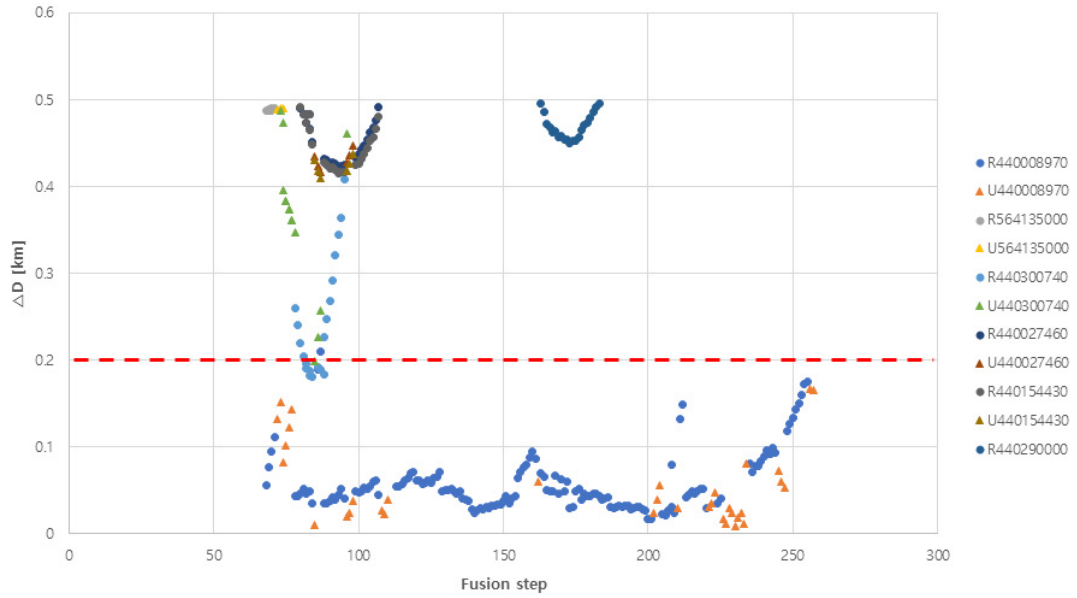

(b)

Fig. 10 Relative distance in Case 4: (a) Relative distance based on the raw data; (b) relative distance based on the processed data

4.4 Result and Abnormal Phenomenon of Case 4

In Case 4, the AIS signal with MMSI 440008970 and ARPA signal with target number 4 were successfully fused using the proposed method, and no typical abnormalities were observed. Fig. 10 shows the change based on the number of attempts of fusion with regard to the difference (ΔD) in the locations of the vessel obtained from the AIS and ARPA signals (based on the analysis results of Case 4).

As shown in Fig. 10(a) (R440008970 (blue circle)), the increase in the measurement time indicated that ΔD varied within the threshold value. Fig. 10(b) shows the case of updating the signal based on the proposed location prediction and object-tracking algorithms for an identical situation, and the change toward the appearance of a data distributional tendency can be identified. Table 7 lists the fusion success rates with respect to the total number of attempts (189 times) for the aforementioned circumstance, and processing as proposed in this study exhibited higher success rates than sensor fusion without any other additional processing.

Table 7 Comparison results of Case 4

Step	Raw data	Present method	Rate of change
First step	154 (56.4%)	188 (64.1%)	18.0%
Second step	149 (24.3%)	176 (26.9%)	14.3%
Third step	147 (76.9%)	174 (89.7%)	14.3%
Fusion	147 (24.3%)	173 (26.9%)	13.8%

4.5 Result and Abnormal Phenomenon of Case 5

In Case 5, the AIS signal with MMSI 440300740 and ARPA signal

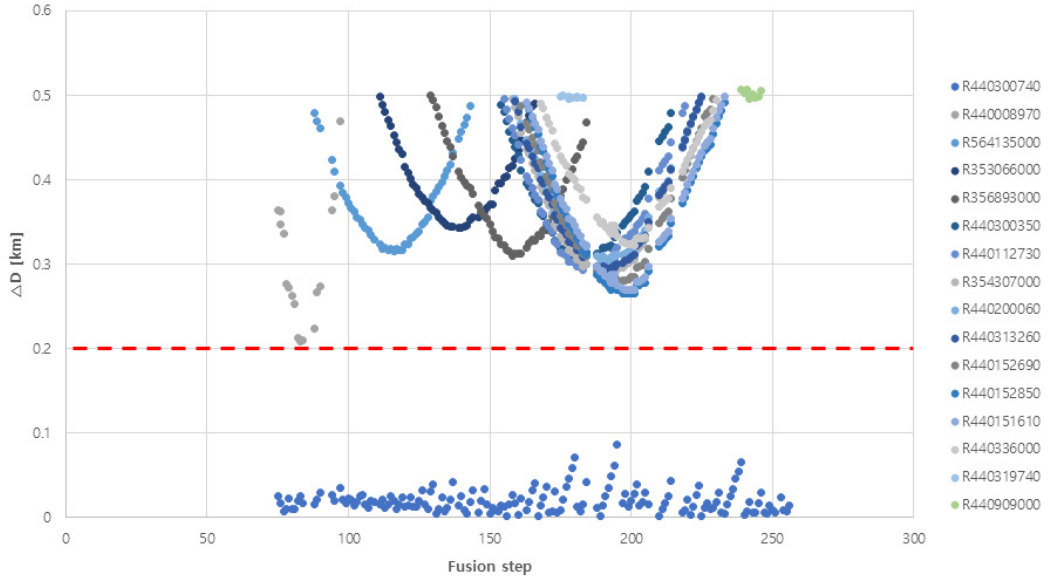

(a)

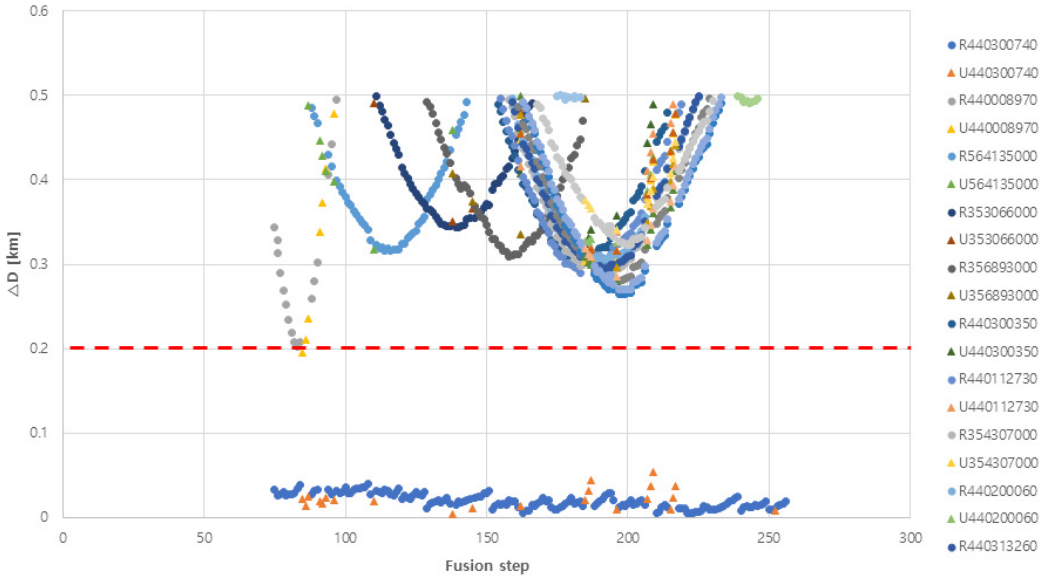

(b)

Fig. 11 Relative distance in Case 5: (a) Relative distance based on the raw data; (b) relative distance based on the processed data

Table 8 Comparison results of Case 5

Step	Raw data	Present method	Rate of change
First step	160 (87.9%)	182 (100.0%)	18.0%
Second step	160 (87.9%)	182 (100.0%)	14.3%
Third step	160 (87.9%)	182 (100.0%)	14.3%
Fusion	160 (87.9%)	182 (100.0%)	13.8%

with target number 5 succeeded in fusion using the proposed method, and no typical abnormalities were observed similar to Case 4. Fig. 11(a) shows the change based on the number of attempts of fusion with regard to the difference (ΔD) between the location of own ship and the locations of the vessel obtained from the AIS and ARPA signals (based on the analysis results of the phenomena of Case 5).

Meanwhile, as shown in Fig. 11(a) for R440300740, ΔD varied within the threshold value with an increase in the measurement time. Fig. 11(b) shows the case of updating the signals using the location prediction algorithm and the proposed object tracking algorithm for the same situation, from which a change toward data having distributional tendency and reduced range of distributed difference between the heterogenous signal locations can be identified.

Table 8 lists the rate of success with regard to the attempted fusion (182 times) for the aforementioned situation, and the success rate was higher when the proposed method was applied rather than proceeding with sensor fusion without processing.

5. Conclusions

This study considered the characteristics of ARPA and AIS signals to propose the sensor fusion algorithm that could determine whether two vessels are identical in real time. To overcome the abnormal phenomenon of signals that may occur in real environments, a UK-PDAF-based multiple-object tracking algorithm was developed to track ARPA signals, and an AIS-data-based location prediction technique was used to reduce the number of errors according to the AIS signal period (time). Moreover, the results of the field tests performed (Cases 1, 4, and 5) to verify the validity of the proposed algorithm indicated that an identical vessel can be recognized at an average probability of 95%; Case 2 was excluded because it experienced ARPA malfunctioning, and in Case 3, the target was mistakenly selected. However, owing to the lack of real measurement data, the application of the proposed techniques was limited for numerous cases. Therefore, in the future, a large number of actual measurements will be necessary to verify the utility of the proposed method. Finally, this study performed object tracking again after receiving the tracked results from the ARPA; however, further studies are required to ultimately track objects based on radar images.

Conflict of Interest

The authors declare that they have no conflict of interests.

Funding

This study was sponsored by Daewoo Shipbuilding & Marine Engineering in 2022 and was supported by the Korea Institute of Energy Technology Evaluation and Planning (KETEP) grant funded by the Korea government (MOTIE) (Project Number:20213030020200, Project Name: Development of fully-coupled aero-hydro-servo-elastic-soil analysis program for offshore wind turbine system).

References

Han, J. W. Lee, S. W., Joe, H. J. & Jin, E. S. (2022). A Study on the tracking of ARPA radar signal based on UK-PDAF and fusion with AIS data. *Proceedings of KAOST 2022 in Jeju.*

Hu, Y., Zhang, A., Tian, W., Zhang, J., & Hou, Z. (2020). Multi-ship collision avoidance decision-making based on collision risk index. *Journal of Marine Science and Engineering, 8*(9), 640. https://doi.org/10.3390/jmse8090640

Woo, J. (2018). *Collision avoidance for an unmanned surface vehicle using deep reinforcement learning* [Doctoral Thesis. Seoul National University Graduate School].

Kim, D. Y., Park, G. K., & Kim, H. Y. (2014). A study on the ship information fusion with AIS and ARPA radar using by blackboard system. *Journal of the Korean Institute of Intelligent Systems, 24*(1), 16−21. https://doi.org/10.5391/JKIIS.2014.24.1.016

Habtemariam, B., Tharmarasa, R., McDonald, M., & Kirubarajan, T. (2015). Measurement level AIS/radar fusion. *Signal Processing, 106*, 348−357. https://doi.org/10.1016/j.sigpro.2014.07.029

Schreier, M.(2017). Bayesian environment representation, prediction, and criticality assessment for driver assistance systems. *at - Automatisierungstechnik, 65*(2), 151−152. https://doi.org/10.1515/auto-2016-0129

Labbe, R. (2014). Kalman filter math. *Kalman and bayesian filters in python, Chap 7*(246), 4.

Author ORCIDs

Author name	ORCID
Han, Chan Woo	0000-0001-8559-022X
Lee, Sung Wook	0000-0001-6089-303X
Jin, Eun Seok	0000-0002-0388-3748

Instructions for Authors

General information

To submit a manuscript to the Journal of Ocean Engineering and Technology (JOET), it is advised to first carefully read the aims and the scope section of this journal, as it provides information on the editorial policy and the category of papers it accepts. Unlike many regular journals, JOET usually has no lag in acceptance of a manuscript and its publication. Authors that find a match with the aims and the scope of JOET are encouraged to submit as we publish works from all over the world. JOET adheres completely to guidelines and best practices published by professional organizations, including Principles of Transparency and Best Practice in Scholarly Publishing (joint statement by COPE, DOAJ, WAME, and OASPA (http://doaj.org/bestpractice) if otherwise not described below. As such, JOET would like to keep the principles and policies of those professional organizations during editing and the publication process.

Research and publication ethics

Details on publication ethics are found in http://joet.org/authors/ethics.php. For the policies on research and publication ethics not stated in the Instructions, Guidelines on Good Publication (http://publicationethics.org/) can be applied.

Requirement for membership

One of the authors who submits a paper or papers should be member of the Korean Society of Ocean Engineers (KSOE), except a case that editorial board provides special admission of submission.

Publication type

Article types include scholarly monographs (original research articles), technical articles (technical reports and data), and review articles. The paper should have not been submitted to other academic journal. When part or whole of a manuscript was already published to conference papers, research reports, and dissertations, then the corresponding author should note it clearly in the manuscript.

Copyright

After published to JOET, the copyright of manuscripts should belong to KSOE. A transfer of copyright (publishing agreement) form can be found in submission website (http://www.joet.org).

Manuscript submission

Manuscript should be submitted through the on-line submission website (http://www.joet.org). The date that manuscript was received through on-line website is the official date of receipt. Other correspondences can be sent by an email to the Editor in Chief or secretariat. The manuscript must be accompanied by a signed statement that it has been neither published nor currently submitted for publication elsewhere. The manuscript should be written in English or Korean. Ensure that online submission are in a standard word processing format. Corresponding author must write the manuscript using the JOET template provided in Hangul or MS Word format. Ensure that graphics are high-resolution. Be sure all necessary files have been uploaded/ attached.

Authors' checklist

Please refer to “Authors' Checklist” for details.

Article structure

Manuscript must be edited in the following order: (1) Title, (2) Authors' names and affiliations, (3) Keywords, (4) Abstract, (5) Nomenclature (optional), (6) Introduction, (7) Main body (analyses, tests, results, and discussions), (8) Conclusions, (9) Conflict of interest, (10) Funding (optional), (11) Acknowledgements (optional), (12) References, (13) Appendices (optional), (14) Author’s ORCIDs.

Abstract

A concise and factual abstract is required. The abstract should state briefly the background, purpose and methods of the research, the principal results and conclusions. An abstract should be written in 150-200 words. References are not cited in abstract whenever possible. Also, non-standard or uncommon abbreviations should be avoided, but if essential they must be defined at their first mention in the abstract itself.

Keywords

Immediately after the abstract, provide a maximum of 5 or 6 keywords.

Unit

Use the international system units(SI). If other units are mentioned, please give their equivalent in SI.

Equations

All mathematical equations should be c1early printed/typed using well accepted explanation. Superscripts and subscripts should be typed clearly above or below the base line. Equation numbers should be given in Arabic numerals enclosed in parentheses on the right-hand margin.

Tables

Tables should be numbered consecutively with Arabic numerals. Each table should be fully titled. All tables should be referred to in the texts.

Figures

Figures should be numbered consecutively with Arabic numerals. Each figure should be fully titled. All figures should be referred to in the texts. All the illustrations should be of high quality meeting with the publishing requirement with legible symbols and legends.

Conflict of interest

It should be disclosed here according to the statement in the Research and publication ethics regardless of existence of conflict of interest. If the authors have nothing to disclose, please state: “No potential

conflict of interest relevant to this article was reported."

Funding

Funding to the research should be provided here. Providing a FundRef ID is recommended including the name of the funding agency, country and if available, the number of the grant provided by the funding agency. If the funding agency does not have a FundRef ID, please ask that agency to contact the FundRef registry (e-mail: fundref.registry@crossref.org). Additional detailed policy of FundRef description is available from http://www.crossref.org/fundref/. Example of a funding description is as follows:

The study is supported by the Inha University research fund (FundRef ID: 10.13039/501100002632), and the Korea Health Personnel Licensing Examination Institute research fund (FundRef ID: 10.13039/501100003647).

Acknowledgments

Any persons that contributed to the study or the manuscript, but not meeting the requirements of an authorship could be placed here. For mentioning any persons or any organizations in this section, there should be a written permission from them.

References in text

References in texts follow the APA style. Authors can also see how references appear in manuscript text through the 'Template'.

Reference list

Reference list follows the APA style. Authors can see how references should be given in reference section through the 'Template'.

Appendices

The appendix is an optional section that can contain details and data supplemental to the main text. If there is more than an appendix, they should be identified as A, B, C, etc. Formulae and equations in appendices should be given separate numbering: Eq. (A1), Eq. (A2), etc.; in a subsequent appendix, Eq. (B1) and so on. Similarly for tables and figures: Table A1; Fig. A1, etc.

ORCID (Open Researcher and Contributor ID)

All authors are recommended to provide an ORCID. To obtain an ORCID, authors should register in the ORCID web site: http://orcid.org. Registration is free to every researcher in the world. Example of ORCID description is as follows:

Joonmo Choung: https://orcid.org/0000-0003-1407-9031

Peer review and publication process

The peer review process can be broadly summarized into three groups: author process, review process, and publishing process for accepted submissions. General scheme is presented in Figure 1.

Check-in process for review

If the manuscript does not fit the aims and scope of the Journal or does not adhere to the Instructions to Authors, it may be rejected immediately after receipt and without a review. Before reviewing, all submitted manuscripts are inspected by Similarity Check powered by iThenticate (https://www.crossref.org/services/similarity-check/), a plagiarism-screening tool. If a too high degree of similarity score is found, the Editorial Board will do a more profound content screening.

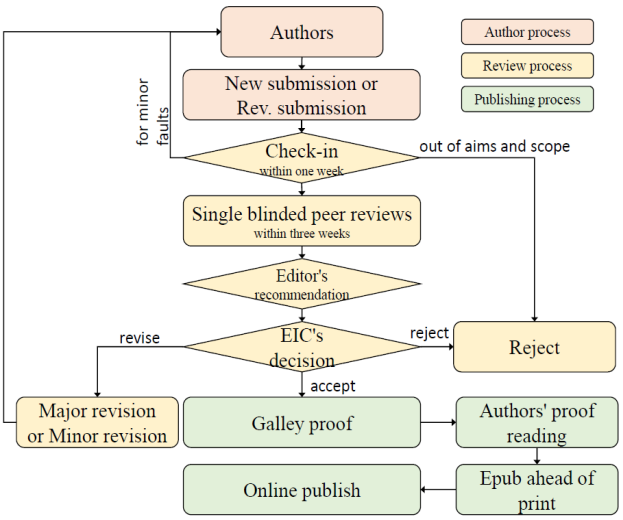

Figure 1 Flow chart of the peer review and publication process of JOET

The criterion for similarity rate for further screening is usually 15%; however, rather than the similarity rate, the Editorial Board focuses on cases where specific sentences or phrases are similar. The settings for Similarity Check screening are as follows: It excludes quotes, bibliography, small matches of 6 words, small sources of 1%, and the Methods section.

Number of reviewers

Reviewers will be selected from the list of reviewers. Manuscripts are then peer reviewed by at least 2 experts in the corresponding field, usually by 2.

Peer review process and the author response to the reviewer comments

JOET adopts single blind review, which means that the authors do not know the identity of the reviews. All papers, including those invited by the Editor, are subject to peer review.

The review period is 4 weeks. Usually the first decision is made within a week after completion of the review. The Editorial Board's decision after the review will be one of followings: Accept, Minor revision, Major revision, or Rejection. The Editorial Board may request the authors to revise the manuscript according to the reviewers' comments. If there are any requests for revision of the manuscript by the reviewers, the authors should do their best to revise the manuscript. If the reviewer's opinion is not acceptable or is believed to misinterpret the data, the author should reasonably indicate that. After revising the manuscript, the author should upload the revised files with a separate response sheet to each item of the reviewer's commentary. The author's revisions should be completed within 3 months after the request. If it is not received by the due date, the Editorial Board will notify the author. To extend the revision period beyond 3 months, the author should negotiate that with the Editorial Board. The manuscript review process can be provided for up two rounds. If the authors wish further review, the Editorial Board may consider it. The Editorial Board will make a final decision on the approval of the submitted manuscript for publication and can request any further corrections, revisions, and deletions of the article text if necessary. Statistical editing is also performed if the data requires professional statistical review by a statistician.

Processing after acceptance

If the manuscript is finally accepted, the galley proof will be sent to the corresponding author after professional manuscript editing and English proofreading. Proofreading should be performed for any misspellings or errors by the authors. Proofreading manuscript for publication is provided to the corresponding author, and the corresponding author must review the proofreading manuscript. Corresponding authors are responsible for the content of the proofreading manuscript and any errors. After final proofreading, the manuscript may appear at the journal homepage as an article in press with a unique DOI number for rapid communication. All published articles will be replaced by the replacement XML file and a final PDF.

Feedback after publication

If the authors or readers find any errors, or contents that should be revised, it can be requested from the Editorial Board. The Editorial Board may consider erratum, corrigendum or a retraction. If there are any revisions to the article, there will be a CrossMark description to announce the final draft. If there is a reader's opinion on the published article with the form of Letter to the editor, it will be forwarded to the authors. The authors can reply to the reader's letter. Letter to the editor and the author's reply may be also published.

How the journal handle complaints and appeals

The policy of JOET is primarily aimed at protecting the authors, reviewers, editors, and the publisher of the journal. If not described below, the process of handling complaints and appeals follows the guidelines of the Committee of Publication Ethics available from: https://publicationethics.org/appeals

- *Who complains or makes an appeal?*

Submitters, authors, reviewers, and readers may register complaints and appeals in a variety of cases as follows: falsification, fabrication, plagiarism, duplicate publication, authorship dispute, conflict of interest, ethical treatment of animals, informed consent, bias or unfair/inappropriate competitive acts, copyright, stolen data, defamation, and legal problem. If any individuals or institutions want to inform the cases, they can send a letter via the contact page on our website: https://www.joet.org/about/contact.php. For the complaints or appeals, concrete data with answers to all factual questions (who, when, where, what, how, why) should be provided.

- *Who is responsible to resolve and handle complaints and appeals?*

The Editorial Board or Editorial Office is responsible for them. A legal consultant or ethics editor may be able to help with the decision making.

- *What may be the consequence of remedy?*

It depends on the type or degree of misconduct. The consequence of resolution will follow the guidelines of the Committee of Publication Ethics (COPE).

Article processing charge

Payment due

Article processing charge (APC) covers the range of publishing services JOET provides. This includes provision of online tools for editors and authors, article production and hosting, and customer services. Upon editorial acceptance of an article for the regular review service and upon submission of an article for the fast review service, the corresponding author will be notified that payment is due.

APC

The APC up to 6 pages is ₩300,000 (or ＄300) and ₩650,000 (or ＄650) for the for the regular and fast review services, respectively. An extra APC of $100 per page is charged for papers longer than 6 pages, No taxes are included in this charge. For the fast review service, an advance fee of ₩250,000 ($250) should be paid on submission.

Payment methods

Credit card payment can be made online using a secure payment form as soon as the manuscript has been editorially accepted. We will we send a receipt by email once payment has been processed. Please note that payment by credit card carries a surcharge of 10% of the total APC.

Invoice payment is due within 7 days of the manuscript receiving editorial acceptance. Receipts are available on request.

JOET Template 2022.08.27

Journal of Ocean Engineering and Technology 00(0), 000-000, December, 2100
https://doi.org/10.26748/KSOE.2100.000
pISSN 1225-0767
eISSN 2287-6715

Original Research Article, Technical Article, Review Article, etc

Title of Article

Firstname Lastname[1], Firstname Lastname[2] and Firstname Lastname[3]

[1]*Professor, Department of OO, OO School, OO University, Busan, Korea*
[2]*Graduate Student, Department of OO, OO University, Seoul, Korea*
[3]*Senior Researcher, Department of OO, OO Engineering. Corp., Seoul, Korea*

KEYWORDS: Lumped mass line model, Explicit method, Steel lazy wave riser (Provide a maximum of 5 or 6 keywords.)

ABSTRACT:

Abstract Construction Guidelines
1) Describe the research background and aims in 1-2 sentences
2) Describe the research/analysis method (method section) in 2-3 sentences.
3) Describe the research/analysis results (results) in 2-3 sentences.
4) Describe the research conclusion in 1-2 sentences.
Abstract Editing Guidelines
1) Review English grammar.
2) Describe in 150-200 words.
3) When using an abbreviation or acronym, write the acronym after full words.
4) Abbreviations (acronyms) used only once should be written in full words only, and no acronyms.
5) References are not included in the abstract.

Nomenclature (Optional)

ITOC	Increment of total operating cost ($/yr)
LHV	Lower heating value (kJ/kg)
Pw	Power (kW)
T	Temperature (K)
V	Volume (m^3)
ρ	Density (kg/m^3)

1. Introduction

The introduction should briefly place the study in a broad context and highlight why it is important. It should define the purpose of the work and its significance. The current state of the research field should be reviewed carefully and key publications cited. Please highlight controversial and diverging hypotheses when necessary. Finally, briefly mention the main aim of the work and highlight the principal conclusions. As far as possible, please keep the introduction comprehensible to scientists outside your particular field of research.

Received 00 February 2100, revised 00 October 2100, accepted 00 October 2100
Corresponding author Firstname Lastname: +82-51-759-0656, e-mail@e-mail.com
It is a recommended paper from the proceedings of 2019 spring symposium of the Korea Marine Robot Technology (KMRTS).

2. General Information for Authors

2.1 Research and Publication Ethics

Authorship should be limited to those who have made a significant contribution to the conception, design, execution, or interpretation of the reported study. All those who have made significant contributions should be listed as co-authors. Where there are others who have participated in certain substantive aspects of the research project, they should be acknowledged or listed as contributors.

The corresponding author should ensure that all appropriate co-authors and no inappropriate co-authors are included on the paper, and that all co-authors have seen and approved the final version of the paper and have agreed to its submission for publication.

Details on publication ethics are found in the journal's website (http://joet.org/authors/ethics.php). For the policies on research and publication ethics not stated in the Instructions, Guidelines on Good Publication (http://publicationethics.org/) can be applied.

2.2 Requirement for Membership

One of the authors who submits a paper or papers should be member of The Korea Society of Ocean Engineers (KSOE), except a case that editorial board provides special admission of submission.

2.3 Publication Type

Article types include scholarly monographs (original research articles), technical articles (technical reports and data), and review articles. The paper should have not been submitted to another academic journal. When part or whole of a manuscript was already published to conference papers, research reports, and dissertations, then the corresponding author should note it clearly in the manuscript.

Example: It is noted that this paper is revised edition based on proceedings of KAOST 2100 in Jeju.

2.4 Copyright

After published to JOET, the copyright of manuscripts should belong to KSOE. A transfer of copyright (publishing agreement) form can be found in submission website (http://www.joet.org).

2.5 Manuscript Submission

Manuscript should be submitted through the on-line submission website (http://www.joet.org). The date that manuscript was received through on-line website is the official date of receipt. Other correspondences can be sent by an email to the Editor in Chief or secretariat. The manuscript must be accompanied by a signed statement that it has been neither published nor currently submitted for publication elsewhere. The manuscript should be written in English or Korean. Ensure that online submission is in a standard word processing format. Corresponding author must write the manuscript using the JOET template provided in Hangul or MS Word format. Ensure that graphics are high-resolution. Be sure all necessary files have been uploaded/ attached.

2.5.1 Authoer’s checklist

Authoer’s checklist and Transfer of copyright can be found in submission homepage (http:/www.joet.org).

3. Manuscript

Manuscript must be edited in the following order: (1) Title, (2) Authors' names and affiliations, (3) Keywords, (4) Abstract, (5) Nomenclature (optional), (6) Introduction, (7) Main body (analyses, tests, results, and discussions), (8) Conclusions, (9) Conflict of interest, (10) Funding (optional), (11) Acknowledgements (optional), (12) References, (13) Appendices (optional), (14) Author’s ORCIDs.

3.1 Unit

Use the international system units (SI). If other units are mentioned, please give their equivalent in SI.

3.2 Equations

All mathematical equations should be clearly printed/typed using well accepted explanation. Superscripts and subscripts should be typed clearly above or below the base line. Equation numbers should be given in Arabic numerals enclosed in parentheses on the right-hand margin. The parameters used in equation must be defined. They should be cited in the text as, for example, Eq. (1), or Eqs. (1)–(3).

$$G_{GEV}(x;\mu,\sigma,\xi)=\begin{cases}\exp[-(1+\xi(x-\mu)/\sigma)^{-1/\xi}] & \xi\neq 0\\ \exp[-\exp(-(x-\mu)/\sigma)] & \xi=0\end{cases} \quad (1)$$

in which μ, σ, and ξ represent the location ("Shift" in figures), scale, and shape parameters, respectively.

3.3 Tables

Tables should be numbered consecutively with Arabic numerals. Each table should be typed on a separate sheet of paper and be fully titled. All tables should be referred to in the texts.

Table 1 Tables should be placed in the main text near to the first time they are cited

Item	Buoyancy riser
Segment length[1)] (m)	370
Outer diameter (m)	1.137
Inner diameter (m)	0.406
Dry weight (kg/m)	697
Bending rigidity ($N\cdot m^2$)	1.66E8
Axial stiffness (N)	7.098E9
Inner flow density ($kg\cdot m^3$)	881
Seabed stiffness ($N/m/m^2$)	6,000

[1)]Tables may have a footer.

3.4 Figures

Figures should be numbered consecutively with Arabic numerals. Each figure should be fully titled. All the illustrations should be of high quality meeting with the publishing requirement with legible symbols and legends. All figures should be referred to in the texts. They should be referred to in the text as, for example, Fig. 1, or Figs. 1−3.

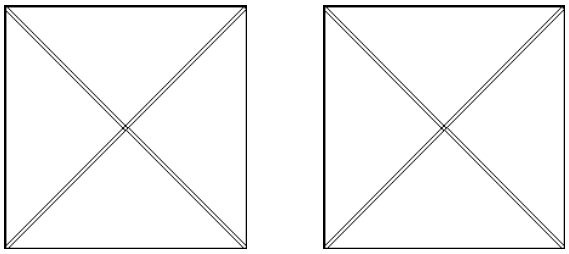

(a) (b)

Fig. 1 Schemes follow the same formatting. If there are multiple panels, they should be listed as: (a) Description of what is contained in the first panel; (b) Description of what is contained in the second panel. Figures should be placed in the main text near to the first time they are cited

3.5 How to Describe the References in Main Texts

- JOET recommends to edit authors' references using MS-Word reference or ZOTERO plug-in
- How to add a new citation and source to a document using MS-Word is found in MS Office web page: https://support.microsoft.com/en-us/office/add-citations-in-a-word-document-ab9322bb-a8d3-47f4-80c8-63c06779f127
- How to add a new citation and source to a document using ZOTERO is found in zotero web page: https://www.zotero.org/

4. Results

This section may be divided by subheadings. It should provide a concise and precise description of the experimental results, their interpretation as well as the experimental conclusions that can be drawn. Tables and figures are recommended to present the results more rapidly and easily. Do not duplicate the content of a table or a figure with in the Results section. Briefly describe the core results related to the conclusion in the text when data are provided in tables or in figures. Supplementary results can be placed in the Appendix.

5. Discussion

Authors should discuss the results and how they can be interpreted in perspective of previous studies and of the working hypotheses. The findings and their implications should be discussed in the broadest context possible. Future research directions may also be highlighted

6. Conclusions

This section can be added to the manuscript.

Conflict of Interest

It should be disclosed here according to the statement in the Research and publication ethics regardless of existence of conflict of interest. If the authors have nothing to disclose, please state: “No potential conflict of interest relevant to this article was reported.”, “The authors declare no potential conflict of interest.”, “The authors declare that they have no conflict of interests.”

Funding (Optional)

Please add: “This research was funded by Name of Funder, grant number XXX” and “The OOO was funded by XXX”. Check carefully that the details given are accurate and use the standard spelling of funding agency names at https://search.crossref.org/funding

Acknowledgments (Optional)

In this section you can acknowledge any support given which is not covered by the author contribution or funding sections. This may include administrative and technical support, or donations in kind (e.g., materials used for experiments). For mentioning any persons or any organizations in this section, there should be a written permission from them.

References

JOET follows the American Psychological Association (APA) style.

- Some samples are found in following web pages: https://apastyle.apa.org/style-grammar-guidelines/references/examples or https://www.ntnu.edu/viko/apa-examples
- JOET recommends editing authors’ references using MS-Word reference or ZOTERO plug-in
- How to add a new citation and source to a document using MS-Word is found in MS Office web page: https://support.microsoft.com/en-us/office/add-citations-in-a-word-document-ab9322bb-a8d3-47f4-80c8-63c06779f127
- How to add a new citation and source to a document using ZOTERO is found in ZOTERO web page: https://www.zotero.org/

Appendix (Optional)

The appendix is an optional section that can contain details and data supplemental to the main text. For example, explanations of experimental details that would disrupt the flow of the main text, but nonetheless remain crucial to understanding and reproducing the research shown; figures of replicates for experiments of which representative data is shown in the main text can be added here if brief, or as Supplementary data. Mathematical proofs of results not central to the paper can be added as an appendix.

All appendix sections must be cited in the main text. In the appendixes, Figures, Tables, etc. should be labeled starting with ‘A’, e.g., Fig. A1, Fig. A2, etc.

Examples:

https://doi.org/10.26748/KSOE.2019.022

https://doi.org/10.26748/KSOE.2018.4.32.2.095

Author ORCIDs

All authors are recommended to provide an ORCID. To obtain an ORCID, authors should register in the ORCID web site: http://orcid.org. Registration is free to every researcher in the world. Example of ORCID description is as follows:

Author name	**ORCID**
So, Hee	0000-0000-000-00X
Park, Hye-Il	0000-0000-000-00X
Yoo, All	0000-0000-000-00X
Jung, Jewerly	0000-0000-000-00X

Authors' Checklist

The following list will be useful during the final checking of a manuscript prior to sending it to the journal for review. Please submit this checklist to the KSOE when you submit your article.

< Checklist for manuscript preparation >

☐ I checked my manuscript has been 'spell-checked' and 'grammar-checked'.

☐ One author has been designated as the corresponding author with contact details such as
- E-mail address
- Phone numbers

☐ I checked abstract 1) stated briefly the purpose of the research, the principal results and major conclusions, 2) was written in 150−200 words, and 3) did not contain references (but if essential, then cite the author(s) and year(s)).

☐ I provided 5 or 6 keywords.

☐ I checked color figures were clearly marked as being intended for color reproduction on the Web and in print, or to be reproduced in color on the Web and in black-and-white in print.

☐ I checked all table and figure numbered consecutively in accordance with their appearance in the text.

☐ I checked abbreviations were defined at their first mention there and used with consistency throughout the article.

☐ I checked all references mentioned in the Reference list were cited in the text, and vice versa according to the APA style.

☐ I checked I used the international system units (SI) or SI-equivalent engineering units.

< Authorship checklist >

JOET considers individuals who meet all of the following criteria to be authors:

☐ Made a significant intellectual contribution to the theoretical development, system or experimental design, prototype development, and/or the analysis and interpretation of data associated with the work contained in the article.

☐ Contributed to drafting the article or reviewing and/or revising it for intellectual content.

☐ Approved the final version of the article as accepted for publication, including references.

< Checklist for publication ethics >

☐ I checked the work described has not been published previously (except in the form of an abstract or as a part of a published lecture or academic thesis).

☐ I checked when the work described has been published previously in other proceedings without copyright, it has clearly noted in the text.

☐ I checked permission has been obtained for use of copyrighted material from other sources including the Web.

☐ I have processed Plasgiarism Prevention Check through reliable web sites such as www.kci.go.kr, http://www.ithenticate.com/, or https://www.copykiller.org/ for my submission.

☐ I agree that final decision for my final manuscript can be changed according to results of Plasgiarism Prevention Check by JOET administrator.

☐ I checked one author at least is member of the Korean Society of Ocean Engineers.

☐ I agreed all policies related to 'Research and Publication Ethics'

☐ I agreed to transfer copyright to the publisher as part of a journal publishing agreement and this article will not be published elsewhere including electronically in the same form, in English or in any other language, without the written consent of the copyright-holder.

☐ I made a payment for reviewing of the manuscript, and I will make a payment for publication on acceptance of the article.

☐ I have read and agree to the terms of Authors' Checklist.

Title of article	:	
Date of submission	: DD/MM/YYYY	
Corresponding author	:	signature
Email address	:	

※ E-mail this with your signature to ksoehj@ksoe.or.kr

Publishing Agreement

ARTICLE DETAILS

Title of article :

Corresponding author :

E-mail address :

DOI : https://doi.org/10.26748/KSOE.2XXX.XXX

YOUR STATUS

I am one author signing on behalf of all co-authors of the manuscript.

ASSIGNMENT OF COPYRIGHT

I hereby assign to the Korean Society of Ocean Engineers, the copyright in the manuscript identified above and any tables, illustrations or other material submitted for publication as part of the manuscript (the "Article"). This assignment of rights means that I have granted to Korean Society of Ocean Engineers the exclusive right to publish and reproduce the Article, or any part of the Article, in print, electronic and all other media (whether now known or later developed), in any form, in all languages, throughout the world, for the full term of copyright, and the right to license others to do the same, effective when the Article is accepted for publication. This includes the right to enforce the rights granted hereunder against third parties.

SCHOLARLY COMMUNICATION RIGHTS

I understand that no rights in patents, trademarks or other intellectual property rights are transferred to the Journal owner. As the author of the Article, I understand that I shall have: (i) the same rights to reuse the Article as those allowed to third party users of the Article under the CC-BY-NC License, as well as (ii) the right to use the Article in a subsequent compilation of my works or to extend the Article to book length form, to include the Article in a thesis or dissertation, or otherwise to use or re-use portions or excerpts in other works, for both commercial and non-commercial purposes. Except for such uses, I understand that the assignment of copyright to the Journal owner gives the Journal owner the exclusive right to make or sub-license commercial use.

USER RIGHTS

The publisher will apply the Creative Commons Attribution-Noncommercial Works 4.0 International License (CC-BY-NC) to the Article where it publishes the Article in the journal on its online platforms on an Open Access basis.

The CC-BY-NC license allows users to copy and distribute the Article, provided this is not done for commercial purposes and further does not permit distribution of the Article if it is changed or edited in any way, and provided the user gives appropriate credit (with a link to the formal publication through the relevant DOI), provides a link to the license, and that the licensor is not represented as endorsing the use made of the work. The full details of the license are available at http://creativecommons.org/licenses/by-nc/4.0/legalcode.

REVERSION OF RIGHTS

Articles may sometimes be accepted for publication but later rejected in the publication process, even in some cases after public posting in "Articles in Press" form, in which case all rights will revert to the author.

☑ I have read and agree to the terms of the Journal Publishing Agreement.

Corresponding author:

name signature

※ E-mail this with your signature to ksoehj@ksoe.or.kr (Papers will not be published unless this form is signed and returned)

Research and Publication Ethics

Journal of Ocean Engineering and Technology (JOET) adheres to the guidelines published by professional organizations, including Committee on Publication Ethics (COPE; https://publicationethics.org/)

1. Authorship

JOET considers individuals who meet all of the following criteria to be authors:

1) Made a significant intellectual contribution to the theoretical development, system or experimental design, prototype development, and/or the analysis and interpretation of data associated with the work contained in the article.
2) Contributed to drafting the article or reviewing and/or revising it for intellectual content.
3) Approved the final version of the article as accepted for publication, including references.

Contributors who do not meet all of the above criteria may be included in the Acknowledgment section of the article. Omitting an author who contributed to your article or including a person who did not fulfill all of the above requirements is considered a breach of publishing ethics.

Correction of authorship after publication: JOET does not correct authorship after publication unless a mistake has been made by the editorial staff.

2. Originality and Duplicate Publication

All submitted manuscripts should be original and should not be in consideration by other scientific journals for publication. Any part of the accepted manuscript should not be duplicated in any other scientific journal without permission of the Editorial Board, although the figures and tables can be used freely if the original source is verified according to the Creative Commons Attribution License (CC BY-NC). It is mandatory for all authors to resolve any copyright issues when citing a figure or table from other journal that is not open access.

3. Conflict-of-Interest Statement

Conflict of interest exists when an author or the author's institution, reviewer, or editor has financial or personal relationships that inappropriately influence or bias his or her actions. Such relationships are also known as dual commitments, competing interests, or competing loyalties. These relationships vary from being negligible to having a great potential for influencing judgment. Not all relationships represent true conflict of interest. On the other hand, the potential for conflict of interest can exist regardless of whether an individual believes that the relationship affects his or her scientific judgment. Financial relationships such as employment, consultancies, stock ownership, honoraria, and paid expert testimony are the most easily identifiable conflicts of interest and the most likely to undermine the credibility of the journal, the authors, or of the science itself. Conflicts can occur for other reasons as well, such as personal relationships, academic competition, and intellectual passion. If there are any conflicts of interest, authors should disclose them in the manuscript. The conflicts of interest may occur during the research process as well; however, it is important to provide disclosure. If there is a disclosure, editors, reviewers, and reader can approach the manuscript after understanding the situation and the background of the completed research.

4. Management Procedures for the Research and Publication Misconduct

When JOET faces suspected cases of research and publication misconduct such as a redundant (duplicate) publication, plagiarism, fabricated data, changes in authorship, undisclosed conflicts of interest, an ethical problem discovered with the submitted manuscript, a reviewer who has appropriated an author's idea or data, complaints against editors, and other issues, the resolving process will follow the flowchart provided by the Committee on Publication Ethics (http://publicationethics.org/resources/flowcharts). The Editorial Board of JOET will discuss the suspected cases and reach a decision. JOET will not hesitate to publish errata, corrigenda, clarifications, retractions, and apologies when needed.

5. Editorial Responsibilities

The Editorial Board will continuously work to monitor and safeguard publication ethics: guidelines for retracting articles; maintenance of the integrity of the academic record; preclusion of business needs from compromising intellectual and ethical standards; publishing corrections, clarifications, retractions, and apologies when needed; and excluding plagiarism and fraudulent data. The editors maintain the following responsibilities: responsibility and authority to reject and accept articles; avoiding any conflict of interest with respect to articles they reject or accept; promoting publication of corrections or retractions when errors are found; and preservation of the anonymity of reviewers.

6. Hazards and human or animal subjects

If the work involves chemicals, procedures or equipment that have any unusual hazards inherent in their use, the author must clearly identify these in the manuscript. If the work involves the use of animal or human subjects, the author should ensure that the manuscript contains a statement that all procedures were performed in compliance with relevant laws and institutional guidelines and that the appropriate institutional committee(s) has approved them. Authors should include a statement in the manuscript that informed consent was obtained for experimentation with human subjects. The privacy rights of human subjects must always be observed.

Ensure correct use of the terms sex (when reporting biological factors) and gender (identity, psychosocial or cultural factors), and, unless inappropriate, report the sex and/or gender of study participants, the sex of animals or cells, and describe the methods used to determine sex and gender. If the study was done involving an exclusive population, for example in only one sex, authors should justify why, except in obvious cases. Authors should define how they determined race or ethnicity and justify their relevance.

7. Secondary publication

It is possible to republish manuscripts if the manuscripts satisfy the conditions of secondary publication. These are:

- The authors have received approval from the Editorial Board of both journals (the editor concerned with the secondary publication must have access to the primary version).
- The priority for the primary publication is respected by a publication interval negotiated by editors of both journals and the authors.
- The paper for secondary publication is intended for a different group of readers
- The secondary version faithfully reflects the data and interpretations of the primary version.
- The secondary version informs readers, peers, and documenting agencies that the paper has been published in whole or in part elsewhere, for example, with a note that might read, "This article is based on a study first reported in the [journal title, with full reference]"
- The title of the secondary publication should indicate that it is a secondary publication (complete or abridged republication or translation) of a primary publication.

8. Complaints and Appeals

The process of handling complaints and appeals follows the guidelines of the COPE available from: https://publicationethics. org/appeals

9. Post-publication discussions and corrections

The post-publication discussion is available through letter to editor. If any readers have a concern on any articles published, they can submit letter to editor on the articles. If there found any errors or mistakes in the article, it can be corrected through errata, corrigenda, or retraction.

The Korean Society of Ocean Engineers